

New Views of IC 10 in the Radio

by

Harrisen Tyler Corbould

A thesis submitted in partial fulfillment of the requirements for the degree of

Master of Science

Faculty of Science Department of Physics
University of Alberta

© Harrisen Tyler Corbould, 2024

Abstract

In this thesis, we showcase new high-resolution VLA L-band data of IC 10, a dwarf irregular galaxy in the Local Group. IC 10 is a target of the Local Group L-band survey (LGLBS) due to its distance, location in the sky, and the fact that it is the only starbursting galaxy in the Local Group. Due to its low metallicity and proximity to the Milky Way, it is a unique candidate for studying star formation and galaxy formation in an environment similar to those in the early universe. This survey has both the highest spatial (4.5'') and spectral (0.4 km/s) resolution HI 21-cm data of IC 10 to date and the highest spatial resolution (1.5'') L-band 1.0 - 2.0 GHz continuum data. We create a catalog of compact continuum sources and classify them by their spectral index and position. We find 62 total sources, of these zero are identified as HII regions with $\alpha > -0.2$, 19 are supernova remnants with a steep spectral index $-0.8 < \alpha < -0.2$, and 43 are background galaxies with steep spectral indices $\alpha < -0.8$. Using a spectral stacking technique, we compare CO (1-0) molecular gas emission with the HI 21-cm emission and recover $\sim 23\%$ more emission than previously visible in the bright CO alone. Performing Gaussian decomposition on the HI and CO data we find the HI is composed of two components in many regions within the disk and we find that the CO emission is often but not necessarily associated with the brightest HI component. Lastly, we analyze an off-disk molecular cloud and find that it is surprisingly normal in its line widths, central velocities, and integrated intensity but displays a very high molecular gas fraction for its low dynamical equilibrium pressure due to the lack of a bright stellar population in the region.

Preface

The research conducted for this thesis forms part of an international research collaboration, the Local Group L-band Survey (LGLBS). This collaboration is led by Dr. Adam Leroy at Ohio State University, Dr. Laura Chomiuk at Michigan State University, Dr. Julianne Dalcanton from the University of Washington, Dr. Snezana Stanimirovic from the University of Wisconsin, Dr. Fabian Walter from the Max Planck Institute for Astronomy and Dr. Erik Rosowlosky from the University of Alberta.

This thesis is an original work by Harrison Corbould. No part of this thesis has been previously published. Some of the data showcased in Chapter 4 was imaged, collected, or created by other members of the collaboration. The HI atomic hydrogen spectral line data was imaged by Dr. Nickolas Pingel, the CO (1-0) emission line data and the WISE infrared data were collected and shared with us by Dr. Adam Leroy, and the WISE infrared data were processed by Dr. Erik Rosolowsky. The continuum emission data showcased in Chapter 4 and the subsequent data analysis are my original work, as well as the literature review in Chapter 3 and the background information in Chapter 2.

Acknowledgements

I would like to thank Dr. Erik Rosolowsky for supervising and funding my graduate studies. More specifically, I would like to acknowledge the invaluable expertise, guidance, and knowledge he has provided throughout my research. I'd also like to thank my supervisory committee members, Dr. Sharon Morsink, Dr. Greg Sivakoff, and Dr. Dmitri Pogolian for providing their time and their feedback on my research progress. Finally, I'd like to thank the LGLBS team for the opportunity to work with them and for their excellent knowledge, feedback, and suggestions.

Table of Contents

| | | |
|----------|--|-----------|
| 1 | Introduction | 1 |
| 1.1 | Motivation | 1 |
| 1.2 | Thesis Objectives | 2 |
| 1.3 | Thesis Outline | 2 |
| 2 | Background | 4 |
| 2.1 | The Interstellar Medium in and Around Galaxies | 4 |
| 2.1.1 | Galaxy evolution | 4 |
| 2.1.2 | Phases of the ISM | 6 |
| 2.1.3 | The Dynamic Interstellar Medium | 10 |
| 2.2 | Radio Astronomy | 15 |
| 2.2.1 | General Radio Astronomy | 15 |
| 2.2.2 | Radio Imaging | 20 |
| 3 | IC 10 Literature Review | 26 |
| 3.1 | The 21-cm Atomic Hydrogen gas in IC 10 | 27 |
| 3.1.1 | The Neutral Disk of IC 10 | 29 |
| 3.1.2 | HI Extensions in and around IC 10 | 31 |
| 3.2 | Molecular Gas in IC 10 | 36 |
| 3.3 | IC 10 in the Radio Continuum | 40 |
| 3.4 | Stellar Populations in IC 10 | 43 |
| 3.5 | Literature Conclusions | 45 |
| 4 | Data Presentation and Analysis | 47 |
| 4.1 | L-band Observations | 47 |
| 4.2 | Radio Continuum | 48 |
| 4.2.1 | Radio Continuum Data and Calibration | 48 |
| 4.2.2 | Continuum Imaging | 49 |
| 4.2.3 | Spectral Index Tests | 50 |

| | | |
|----------|--------------------------------------|------------|
| 4.2.4 | Continuum Source Catalog | 60 |
| 4.3 | Spectral Lines | 62 |
| 4.3.1 | Neutral Hydrogen | 63 |
| 4.3.2 | CO Lines | 65 |
| 4.4 | Multi-wavelength Data | 68 |
| 4.5 | Spectral Line Stacking | 68 |
| 4.5.1 | Stacking Methodology | 70 |
| 4.5.2 | Results | 73 |
| 4.6 | Gaussian Decomposition | 77 |
| 4.6.1 | Method | 77 |
| 4.6.2 | Results | 79 |
| 4.7 | Off-disk Cloud | 85 |
| 4.7.1 | Methods | 85 |
| 4.7.2 | Results | 89 |
| 5 | Conclusions & Future Work | 98 |
| 5.1 | Conclusions | 98 |
| 5.2 | Future Work | 99 |
| | Appendix A: Appendix | 108 |

List of Tables

| | | |
|-----|---|----|
| 4.1 | IC 10 continuum source catalog. This table shows the first 10 rows of the continuum source catalog with the full catalog available in the appendix A.1. Offset is the source offset from the field center in arcseconds, L-band α is the L-band In-band spectral index value calculated from the CASA <code>.alpha</code> image, L-to-C α is the 2 point spectral index calculated between the L-band 1.5 GHz data and the C-band 6.0 GHz data. | 62 |
| 4.2 | IC 10 spectral stacking results over the central disk. Spectral stacking was performed by binning the data into 11 equal-sized bins based on HI integrated intensity, shifting the spectra to a common velocity before averaging over all the spectra in a given bin. The 95-100% bin contains the brightest 5% of HI pixels. The integrated intensity values were found by integrating the spectra seen in figure 4.12 and the full-width half-maximum values were taken from the Moffat fits using <code>lmfit</code> (Newville et al., 2015). Bins below 45% brightest were not included as no CO emission was able to be recovered. | 74 |
| 4.3 | IC 10 spectral stacking results over the off-disk molecular cloud. Spectral stacking was performed by binning the data into 11 equal-sized bins based on HI integrated intensity, shifting the spectra to a common velocity before averaging over all the spectra in a given bin. The 95-100% bin contains the brightest 5% of HI pixels. The integrated intensity values were found by integrating the spectra seen in figure 4.20 and the full-width half-maximum values were taken from the Moffat fits using <code>lmfit</code> (Newville et al., 2015). Bins below 45% brightest were not included as no CO emission was able to be recovered. | 91 |

| | | |
|-----|---|-----|
| A.1 | IC 10 full continuum source catalog including all 62 compact continuum sources, L-band and C-band flux densities and both the L-band in-band spectral index as well as the L-band to C-band spectral index. Offset is the source offset from the field center in arcseconds, L-band α is the L-band in-band spectral index value calculated from the CASA <code>.alpha</code> image, L-to-C α is the 2 point spectral index calculated between the L-band 1.5 GHz data and the C-band 6.0 GHz data. | 112 |
|-----|---|-----|

List of Figures

| | | |
|-----|---|----|
| 2.1 | The (u, v, w) baseline coordinate system and (l, m, n) are the sky coordinates, which are a function of the baseline coordinates. The system is constructed so that w points towards the source, v points north, and u points east. | 18 |
| 3.1 | LGLBS VLA HI 21-cm Integrated Intensity maps. The top panel shows the 4 configuration A+B+C+D high spatial resolution $\sim 4.5''$ map which displays many holes and shells visible in the disk. The bottom panel shows the lower resolution $\sim 19''$ C+D configuration map which displays the diffuse low column density gas and the large HI extensions, labeled as the three “spurs” and one “plume.” This figure is intended as a visual aid when discussing previous research on the HI emission in IC 10, more details on the data are available in chapter 4. | 28 |
| 3.2 | LGLBS CO (1-0) IC 10 integrated intensity map [K km/s] with HI integrated intensity contours overlaid. The HI contours are at levels 800, 1500, and 2500 [K km/s]. Within this figure, we can see giant molecular clouds coincident with the high column density HI. The brightest CO emission is concentrated within the large HI cloud at the bottom of the figure and along HI shells. This figure is intended as a visual aid when discussing previous research on the molecular gas in IC 10, more details on the data are available in chapter 4. | 36 |
| 3.3 | LGLBS IC 10 1.5 GHz L-band continuum image with a spatial resolution of $\sim 1.5''$. At the center of the figure, we can see a large non-thermal superbubble and throughout the region many compact continuum sources. This figure is intended as a visual aid when discussing previous research on the continuum emission in IC 10, more details on the data are available in chapter 4. | 39 |

4.1 L-band 1.0 - 2.0 GHz Continuum data. The top panel shows a large field of view covering $\sim 0.5^\circ$. The bottom panel shows the same data over a smaller region containing the majority of the continuum emission in IC 10 over $\sim 0.125^\circ$ or $7.5'$. Overlaid are contours from the HI moment 0 integrated intensity map at 250 [K km/s] and 1000 [K km/s] for the top and bottom panels respectively. 51

4.2 L-band 1.0 - 2.0 GHz continuum image with final catalog source locations overplotted. These are compact continuum ($< 3''$) sources that are likely HII regions, supernova remnants, and background galaxies. Labels are Source ID numbers from the source detection algorithm pyBDSF. 53

4.3 L-band slope Spectral Index vs. CASA Spectral Index. The figure shows the spectral index of sources over the 1.6 - 2.0 GHz frequency range calculated through two methods. On the horizontal axis is the spectral index found via the CASA `.alpha` output spectral index map. The vertical axis shows the spectral index calculated through the slope of the $\log(\text{Flux})$ vs. $\log(\text{Frequency})$ plot for each source across four 0.1 GHz wide sub-band images at 1.6 - 1.7 GHz, 1.7 - 1.8 GHz, 1.8 - 1.9 GHz, and at 1.9 - 2.0 GHz. The dashed line indicates the locus of equality. 54

4.4 CASA Spectral Index vs. Offset from the center of the image [arcsec]. The vertical axis is the spectral index calculated from the CASA output `.alpha` image from a 1.6 - 2.0 GHz image. The horizontal axis is the offset of each source from the center of the field in arcseconds. The blue points are labeled with their source IDs from the detection algorithm in pyBDSF. The dashed red lines represent the typical range for radio spectral indices between +1 and -2. 55

4.5 W-project Spectral Index vs. AW-project Spectral Index. The vertical axis shows the spectral index using the W-project gridding algorithm which only takes the sky curvature effect into account. The horizontal axis shows the spectral index from the AW-project gridding algorithm which also takes into account the antenna beam size changing with frequency. The red line represents the line of equality and each point is labeled with its source ID from pyBDSF. 57

4.6 W-project & AW-project spectral index vs. Offset from image center [arcsec]. The left panel shows the W-project gridding algorithm spectral index vs. the offset from the center of the image in arcseconds. The right panel shows the AW-project gridding spectral index vs. the offset from the center in arcseconds. The red lines show the typical range for radio spectral indices between +1 and -2. Note: The vertical axis in each panel does not share a common scale. 58

4.7 L-band 1.0 - 2.0 GHz and C-band 4.0 - 8.0 GHz data. The upper panel shows the LGLBS L-band continuum data with a $\sim 1.5''$ spatial resolution. This is the same data as shown in figure 4.1 now only over a smaller central region where we also have C-band data. The C-band data is from VLA project 15A-062 (PI: David Cseh) and can be seen in the lower panel with a spatial resolution of $\sim 1''$ 59

4.8 L-band Spectral Index vs. L-band to C-band Spectral Index. The horizontal axis shows the in-band L-band spectral index values over the 1.0 - 2.0 GHz frequency range. These were calculated from the CASA output .alpha image. The vertical axis shows the L-band to C-band two-point spectral index calculated from equation 4.3 over the 1.5 - 6.0 GHz frequency range. The red line indicates the line of equality. 61

4.9 IC 10 HI Moment Maps. The upper left panel shows the Moment 0 Integrated Intensity plot [K km/s], and the upper right panel shows the Moment 1 Intensity weighted velocity map [km/s]. In the bottom left panel, we have the line width FWHM map [km/s] and in the bottom right panel the peak temperature [K] map can be seen. 66

4.10 IC 10 CO (1-0) molecular gas moment 0 integrated intensity map [K km/s] with HI atomic hydrogen moment 0 integrated intensity contours overlaid in white. The HI contours are at levels 800, 1500, and 2500 K km/s. 67

4.11 WISE 3.4 μm map from the z0MGS atlas (Leroy et al., 2019) showcasing the stellar emission in IC 10. Overlaid in white are HI integrated intensity contours at 800 K km/s, in green CO (1-0) integrated intensity contours can be seen at a level of 1.5 K km/s. The stellar emission in the galaxy is concentrated towards the center-right of the disk with the brightest stellar emission coincident with the large HI cloud at the bottom center of the disk. 69

| | | |
|------|--|----|
| 4.12 | CO (1-0) & HI 21-cm line spectral stacking results. The left column in the figure corresponds to the CO (1-0) stacks and the right column is the HI-on-HI spectral stack results. The blue points represent the data and the green line is the Moffat profile fit with <code>lmfit</code> (Newville et al., 2015). The top row of each column shows all the stacks in one figure. Starting with the second row and going down we have the brightest bins at 95% - 100% decreasing in 5% bins until the dimmest bin at the bottom which corresponds to the 45% - 50% brightest HI pixels. . . . | 75 |
| 4.13 | Column density of hydrogen nuclei/cm ² from atomic and molecular hydrogen. The vertical axis is the log-scale column density from molecular hydrogen calculated with equation 4.10. The horizontal axis shows the log-scale column density from atomic hydrogen calculated with equation 4.9. The dashed grey line represents the line of equality and the dotted black line is a column density scaling relation derived from Eibensteiner et al. (2024) and seen in equation 4.15. | 76 |
| 4.14 | HI Gaussian Decomposition Results of IC 10's disk from ROHSA (Marchal et al., 2019). The top row shows the one component decomposition parameters. The second and third rows show the HI two component decomposition parameters, the second row is the first of the two components and the third row is the second of the two components. The left column shows the Amplitude of the Gaussian [K], the center column shows the central velocity of the Gaussian [km/s] and the right column shows the velocity dispersion of the Gaussian [km/s]. | 82 |
| 4.15 | CO 1-0 Gaussian decomposition results of IC 10's disk from ROHSA (Marchal et al., 2019). The Left panel shows the Amplitude of the Gaussian [K], the center panel shows the central velocity of the Gaussian [km/s] and the right panel shows the velocity dispersion of the Gaussian [km/s]. | 82 |
| 4.16 | Gaussian decomposition spectra example. These spectra show a two component decomposition with both a wide and a narrow component. The narrow component peaks at a brightness temperature of ~ 63 K and the wide component has a peak value of ~ 35 K. These spectra are from a region within the large HI cloud at a RA $\sim 0^{\text{h}}20^{\text{m}}30^{\text{s}}$ and DEC $\sim 59^{\circ}17'$ | 83 |

| | | |
|------|--|----|
| 4.17 | Gaussian decomposition spectra example. This figure shows a two component decomposition with two separate distinct components. One component has a peak amplitude of ~ 18 K and the other ~ 18 K. The components have central velocities of ~ -438 km/s and ~ -336 km/s, separated by ~ 100 km/s. These spectra are from a region surrounded by HI holes and shells at a RA $\sim 0^{\text{h}}20^{\text{m}}10^{\text{s}}$ and DEC $\sim 59^{\circ}18.5'$ | 83 |
| 4.18 | Gaussian decomposition spectra example. These spectra show a one component decomposition that peaks at a brightness temperature of ~ 100 K and a central velocity of ~ -345 km/s. These spectra are from a region within the large HI cloud at a RA $\sim 0^{\text{h}}20^{\text{m}}22^{\text{s}}$ and DEC $\sim 59^{\circ}17'$ | 84 |
| 4.19 | The CO (1-0) Moment 0 integrated intensity map [K km/s] with HI moment 0 contours overlaid. The HI contours are at levels 800, 1500, and 2500 K km/s. The off-disk cloud is highlighted and circled on the left side of the image. | 86 |
| 4.20 | CO 1-0 & HI 21-cm line spectral stacking results for the off-disk cloud. The left column in the figure corresponds to the CO (1-0) stacks and the right column is the HI on HI spectral stack results. The top row shows all the stacks in one figure. Starting with the second row and going down we have the brightest bins at 95% - 100% decreasing in 5% bins until the dimmest bin at the bottom which corresponds to the 45% - 50% brightest HI pixels. | 90 |
| 4.21 | Column densities from off-disk cloud stacking results. The atomic hydrogen column density N_{HI} can be seen on the horizontal axis and the molecular hydrogen column density N_{H_2} can be seen on the vertical axis. The disk column densities from 4.13 can be seen in blue points and the off-disk cloud column densities can be seen by green x's. Compared with the disk region, the off-disk cloud has significantly higher column densities. The grey dashed line represents the line of equality and the black dotted line represents the scaling relation from Eibensteiner et al. (2024) seen in 4.15. | 92 |

| | | |
|------|---|----|
| 4.22 | Molecular gas fraction vs. Dynamical equilibrium pressure for the spectral stacking bins for both the disk and off-disk molecular cloud. In blue points we can see the points associated with the full disk stacking bins and represented by green x's we can see the off-disk molecular cloud stacks. The dynamical equilibrium pressure P_{DE} was calculated using equation 4.18 and the molecular gas fraction R_{mol} was calculated using equation 4.22. The black dotted line represents the scaling relation from Eibensteiner et al. (2024) as seen in equation 4.26. . . . | 94 |
| 4.23 | Molecular gas fraction vs. Stellar mass surface density. This figure shows the molecular gas fraction R_{mol} vs. stellar mass surface density Σ_* on a pixel-by-pixel basis. The molecular gas fraction was calculated using equation 4.22 and the stellar mass surface density was calculated using equation 4.25. The values for the disk pixels can be seen represented by blue points and the off-disk cloud pixels can be seen as green x's. This shows the off-disk cloud is dominated by gas. | 95 |
| 4.24 | Gaussian Decomposition Amplitudes, Central velocities, and Line-widths for the CO Gaussian decomposition vs. the HI Gaussian decomposition. Prior to our analysis we convolved the HI to the CO spatial resolution and reprojected the data to the CO pixel grid. We then spatially smoothed it prior to the Gaussian decomposition of the spectra to ensure an accurate comparison. We masked the data to include only regions that have both bright CO and HI emission and compared the CO one-component decomposition to the HI component closest to the CO in velocity space. In blue we can see the pixels with bright emission in the disk and in red we have highlighted the off-disk molecular cloud. | 96 |
| 4.25 | Position-Velocity diagram over the off-disk cloud along a slice following the HI emission. The left panel shows the HI atomic hydrogen position velocity diagram using the HI data with convolved and spectrally smoothed to the CO resolution of $8.5''$ and 2.5km/s . The right panel shows the CO (1-0) data over the same slice. Of note is that the off-disk cloud does not have a substantial change in velocity across the slice indicating there may not be multiple HI kinematic components in the region. | 97 |

List of Symbols

Constants

| | | |
|-------|-------------------------|---|
| G | Gravitational Constant. | $4.30 \times 10^{-3} \text{ pc } M_{\odot} \text{ km s}^{-1}$ |
| k_B | Boltzmann Constant. | $1.38 \times 10^{-23} \text{ J/K}$ |

Latin

| | |
|----------------------|---|
| h_* | Disk scale height |
| $I_{3.4\mu\text{m}}$ | $3.4\mu\text{m}$ Intensity |
| I_ν | Specific intensity |
| M_0 | Moment 0 |
| M_1 | Moment 1 |
| M_2 | Moment 2 |
| N_{H_2} | Molecular hydrogen column density |
| N_{HI} | Atomic hydrogen column density |
| P_{DE} | Dynamical equilibrium pressure |
| R_{mol} | Molecular gas fraction |
| $s(l, m)$ | Point spread function or dirty beam |
| $S(u, v)$ | Sampling function in baseline coordinates |
| S_ν | Flux density |
| S_C | C-band flux density |
| S_L | L-band flux density |
| $T(l, m)$ | Sky brightness distribution in sky coordinates or image |
| $T^D(l, m)$ | Sky brightness distribution in sky coordinates or dirty image |
| T_B | Brightness Temperature |
| $V(u, v)$ | Complex visibility function in baseline coordinates |

X_{CO} Column density CO-to- H_2 conversion factor

H_2 Molecular hydrogen

HI Atomic hydrogen

HII Ionized hydrogen

Greek

α Spectral index

α_{CO} Mass density CO-to- H_2 conversion factor

χ^2 Deviance

ν Frequency

ρ_* Stellar mass volume density

Σ_* Stellar gas mass density

σ_{atom} Atomic gas velocity dispersion

$\sigma_{\text{gas},z}$ Mass-weighted average velocity dispersion

Σ_{gas} Total gas mass density

Σ_{H_2} Molecular gas mass density

Σ_{HI} Atomic gas mass density

σ_{mol} Molecular gas velocity dispersion

σ_{TB} Brightness temperature noise

θ_{PB} Primary beam full width at half power

$\Upsilon_{3.4\mu\text{m}}$ $3.4\mu\text{m}$ mass-to-light ratio

Abbreviations

AGN Active galactic nuclei.

ALMA Atacama Large Millimeter Array.

BCD Blue compact dwarf.

BIC Bayesian information criterion.

CARTA Cube analysis and rendering tool for Astronomy.

CASA The common astronomy software applications.

CMB Cosmic microwave background emission.

CNM Cold neutral medium.

DRAO Dominion Radio Astrophysical Observatory.

EM Electromagnetic.

FFT Fast Fourier transform.

FWHM Full width at half maximum.

GBT Greenbank Telescope.

GMC Giant molecular cloud.

HIM Hot ionized medium.

HST Hubble Space Telescope.

IGM Intergalactic medium.

ISM Interstellar medium.

ISRF Interstellar radiation field.

LGLBS The Local Group L-band Survey.

LMC Large Magellanic Cloud.

LOFAR Low Frequency Array.

MTMFS Multi-term multi-frequency synthesis.

NTSB Non-thermal superbubble.

PAH Polycyclic aromatic hydrocarbon.

PDR Photo-dissociation region.

PV-Diagram Position-velocity diagram.

QA Quality assurance.

RFI Radio frequency interference.

RGB Red giant branch.

RMS Root Mean Square.

ROHSA Regularized optimization for hyper-spectral analysis.

SMC Small Magellanic Cloud.

VLA Very Large Array.

VLBA Very long baseline array.

WIM Warm ionized medium.

WISE Wide-field Infrared Survey Explorer.

WNM Warm neutral medium.

WR Wolf-Rayet.

Glossary of Terms

Active galactic nuclei A compact region at the center of a galaxy made up of supermassive black holes that emit bright jets.

Baseline The vector connecting two radio telescope antennas within an interferometer.

Beam The area on the sky that a radio telescope is receiving signal from.

Blue compact dwarf Dwarf galaxies showing with low-luminosity, low-metallicity and a high star formation rate.

Brightness temperature In radio Astronomy, a scaled version of the specific intensity that is the temperature at which a black body would have to have to be to emit at the intensity of the source.

C-band VLA frequency band between 4.0 - 8.0 GHz.

Column density The number of atoms per square centimeter along the line of sight.

Continuum emission Electromagnetic radiation producing a range of wavelengths.

Convolution A mathematical operation on two functions that produces a third.

Deconvolution Inverse of convolution, used to recover the original signal prior to convolution.

Dwarf galaxy Smaller galaxies roughly a tenth the size of a typical spiral galaxy.

Dynamical equilibrium pressure The expected average ISM pressure needed to balance the weight of the ISM in the gravitational potential of the galaxy.

Elliptical galaxy Generally older galaxies with no distinct structures and an ellipsoidal shape.

Flux density The radiation received per unit time per unit area per unit frequency.

Fourier transform Based on the concept that any signal can be represented as a sum of sinusoids, a Fourier transform is a mathematical tool that decomposes a signal into its sinusoidal components.

Free-Free emission Thermal emission emitted from the interaction of two free electrons.

Gas kinematics The measurement of gas velocities and motions.

Gaussian decomposition In Astronomy, a technique used to decompose spectra into individual velocity components.

Interferometry In radio Astronomy, the technique used to combine signals from multiple antennas to synthesize a larger telescope.

Intergalactic medium Material found between galaxies, mostly consisting of diffuse neutral hydrogen gas.

Interstellar medium The region between stars made up of gas, dust and radiation responsible for forming stars in galaxies.

Irregular galaxy A galaxy that does not have a distinct regular shape.

L-band VLA frequency band between 1.0 - 2.0 GHz.

Metallicity In Astronomy, the abundance of elements heavier than hydrogen and helium.

Photo-dissociation The process in which molecules are broken apart by the absorption of a photon.

Photo-ionization The process in which an ion is formed from the interaction of an atom or molecule with a photon.

Specific intensity The power per unit area per unit solid angle per unit frequency or as the brightness per unit frequency.

Spectral index A measure of the dependence of the radiative flux density on frequency for a source.

Spectral cube A 3D cube of data containing two spatial dimensions and one spectral dimension.

Spectral emission lines Electromagnetic radiation emitted at discrete wavelengths.

Spiral galaxy A galaxy consisting of a rotating disk with spiral arms, central bars and cores.

Starburst A period of very high star formation within a galaxy.

Superbubble A large cavity in the interstellar medium composed of hot gas carved out by stellar winds and supernova explosions.

Supernova remnant A rapidly rotating neutron star that emits beams of electromagnetic radiation from its poles.

Synchrotron emission Non-thermal emission when relativistic particles spiral around magnetic field lines.

Chapter 1

Introduction

1.1 Motivation

As part of the Local Group L-band Survey (LGLBS), we have new high-resolution Very Large Array (VLA) radio 21-cm atomic hydrogen data and 1.0 - 2.0 GHz radio continuum data on six of the Local Group galaxies. Two of these galaxies are the Local Group spiral galaxies Andromeda (M31) and Triangulum (M33), and the remaining four galaxies are the dwarf galaxies NGC 6822, WLM, IC 1613 and IC 10.

Our target, IC 10 is a nearby irregular dwarf galaxy with a distance of 0.7 Mpc (Hunter et al., 2012). Its optical galaxy is quite small covering somewhere between $6'$ - $7'$ (Massey and Armandroff, 1995) and $20'$ - $46'$ (Sanna et al., 2010). The HI neutral galaxy takes up a much larger region, with a bright disk covering $\sim 0.5^\circ$ and an extended low column density envelope that covers $\sim 1^\circ$ on the sky. IC 10 has a systemic velocity of ~ -350 km/s and complex kinematics within and around the HI disk, showing HI holes, shells, and counter-rotating extensions. IC 10 is a blue compact dwarf galaxy demonstrating a very high star formation rate per unit area $\sim 0.049 M_\odot \text{yr}^{-1} \text{kpc}^{-2}$ indicating an ongoing starburst phase (Tehrani et al., 2017). Due to its low metallicity ($\frac{1}{4} Z_\odot$, Lee et al. (2003)) and proximity to us, IC 10 is a unique target enabling us to study low metallicity star and galaxy formation in the early universe. Studying the HI 21-cm emission with high-resolution data allows us to study the star-forming regions within the disk and to understand the complex history

of the Local Group dwarf galaxy.

1.2 Thesis Objectives

The objectives of this thesis are to showcase the new high-resolution data on IC 10 and to demonstrate analysis techniques and results that are possible with LGLBS data. First, we will inform the reader about IC 10 through a literature review on the neutral 21-cm gas, the molecular and ionized regions, the radio continuum emission, and finally the stellar populations. We will then showcase our data and three science demonstrators:

1. Spectral line stacking in which we use the HI 21-cm emission to study the molecular gas CO emission in dim regions.
2. Gaussian Decomposition where we decompose the HI emission spectra into multiple velocity components and compare them with the molecular gas components of the interstellar medium (ISM).
3. Radio continuum imaging and source catalog, presenting the positions, flux, and spectral indices of compact radio continuum sources.

1.3 Thesis Outline

The following chapters will first introduce the reader to the background information relevant to this research before introducing our data and science demonstrators. Chapter 2 will cover all relevant background information critical to the understanding of the research methodology, results, and analysis. Section 2.1 will introduce the theory behind the interstellar medium that we are observing, and Section 2.2 will cover an introduction to radio astronomy theory, techniques, and the imaging process. We will describe the different types of data collection, single dish and interferometer radio

observatories, emission mechanisms in our wavelength bands, and the practical radio imaging process.

Chapter 3 will contain a literature review of our target, IC 10, emphasizing why it is a target of interest in the radio continuum emission, the spectral line emission, and through its stellar populations. Section 3.1 will cover the 21-cm atomic hydrogen gas in IC 10 starting with the neutral disk and finishing with the HI extensions and their possible origins. Section 3.2 will describe the molecular gas in the galaxy, section 3.3 will describe the radio continuum and section 3.4 will cover the stellar populations.

Chapter 4 will introduce and showcase our data our results and our analysis. Section 4.1 will cover our L-band observational parameters and sensitivity requirements, 4.2 - 4.4 will cover our continuum imaging, data, and source catalog, our spectral line data including the atomic hydrogen 21-cm emission line data, the CO molecular gas data and our multi-wavelength data. Section 4.5 will describe the spectral line stacking technique and results, and Section 4.6 covers spectral line Gaussian decomposition. In Section 4.7 we apply our methods to analyze an off-disk molecular cloud. Finally, in Chapter 5 we will conclude our findings and discuss future work.

Chapter 2

Background

2.1 The Interstellar Medium in and Around Galaxies

2.1.1 Galaxy evolution

There are two main theories of galaxy evolution, the first is the top-down theory where large gas clouds collapse to form a disk which then breaks into small clouds as the disk cools which then form stars. Recent theories of galaxy evolution focus on the bottom-up model where it is proposed that instead of matter starting in large galactic scale clumps, it began in the smaller clouds, which then collided and merged to form galaxies. These galaxies were then drawn together by gravity to form galaxy clusters. The following section is based on *Galaxies in the Universe* by Sparke and Gallagher (2007).

The bottom-up theory has its roots in the Lambda-Cold Dark Matter (Λ -CDM) cosmological model where, following the Big Bang, the universe was essentially homogeneous, and dark matter was evenly spread out and mixed with baryons in the form of hot gas. However, regions of slightly higher density pulled together by their gravity existed and as the universe cooled clumps of matter and dark matter were pulled together under gravity. The larger clumps then absorbed the smaller ones creating large halos. As the clumps combined the gas within them was compressed, and if it was dense enough to cool, energy was lost and baryons fell inward. Dark matter

particles cannot lose energy, so galaxies consist of a central part that is mainly cool gas and luminous stars with a leftover dark matter halo. Then later halos merged to form larger and larger galaxies. These dark matter halos therefore may contain one or more clumps of dark matter bound together by gravity containing galaxies within them. (Sparke and Gallagher, 2007).

This model predicts a large number of mergers which leads to an underestimation of the number of thin disk galaxies as the disk structure is often destroyed in a merger (Steinmetz and Navarro, 2002). Signatures of mergers and interactions in galaxy formation can take different forms. If the two galaxies are a similar size to one another they may form an elliptical galaxy where the heated gas was too diffuse to cool and its pressure prevented it from collapsing inward (Barnes, 1989). Other mergers between different-sized galaxies may create a spiral galaxy with tidal tails or a bridge between the large galaxy and a companion (Ashley et al., 2014; Toomre and Toomre, 1972).

Blue compact dwarf galaxies like IC 10 are irregular dwarf galaxies undergoing a burst of star formation. It is not yet clear as to the origins of these starbursts however, it is often thought that they are the result of mergers, interactions with a companion, or accretion of the intergalactic medium (IGM). However, many BCDs are thought to be isolated meaning an interaction origin is not likely (Wilcots and Miller, 1998; Nidever et al., 2013; Namumba et al., 2019; Ashley et al., 2014). Understanding how starbursts are triggered in BCD galaxies is crucial to understanding how they form and how they are related to other dwarf galaxies. Stellar population studies have shown that stars in massive galaxies tend to have formed earlier and on a shorter time span and dwarfs are the systems currently undergoing the most active star formation. Neistein et al. (2006) show that this has its roots in the bottom-up clustering process of halos.

Since IC 10 is the only starburst BCD in the Local Group it is the best candidate to study and determine what triggers star formation in a BCD. Understanding how

IC 10 triggered its starburst, therefore, has implications on our knowledge of BCD formation and its low metallicity combined with the bottom-up theory for galaxy formation suggests it has implications on how galaxies in the early universe formed. Its proximity makes it an excellent subject to study; however, it lies behind the Galactic plane with a galactic latitude of only -3.3° , which makes it difficult to observe because of high extinction.

2.1.2 Phases of the ISM

The ISM is made up of the gas and dust between stars and is responsible for forming stars in galaxies. The interstellar gas contains many components, including hot ionized gas, neutral atomic gas, and molecular clouds (Draine, 2011). The interstellar dust is made up of small solid particles mixed within this gas. These components of the ISM can take many forms including that of HII regions, star-forming molecular clouds, and supernova remnants. The regions between stars include not only the ISM and its gas and dust but also cosmic rays, electromagnetic radiation, magnetic fields, and gravitational fields which all have some effect on the gas and light we observe.

In a spiral galaxy like the Milky Way or the Andromeda galaxy (M31), most of the dust and gas is found within a thin gaseous disk. In dwarf galaxies like IC 10, we see different more complex morphologies, which often include a less uniform disk with many features of turbulent gas such as shells and holes. In IC 10, the majority of the molecular and hot ionized gas is contained within this central neutral disk (Leroy et al., 2006; Wilcots and Miller, 1998). However, the dwarf also contains many large-scale neutral extensions separate from the disk (Wilcots and Miller, 1998; Ashley et al., 2014; Nidever et al., 2013; Namumba et al., 2019).

These different gases can be classified into three phases: ionized gas, neutral gas, and molecular gas, which can then be split into a further six phases of interstellar gas (Draine, 2011). These six phases are the Hot Ionized Medium (HIM), the Warm Ionized Medium (WIM), the Warm Neutral Medium (WNM), the Cool Neutral Medium

(CNM), Diffuse and dense H₂ molecular gas and finally cool stellar outflows.

The following sections on the phases of the interstellar medium are based on *Physics of the Interstellar and Intergalactic Medium* by Draine (2011).

Neutral Hydrogen in the ISM

As stated above, the neutral medium of the ISM can be split into two separate phases; The warm neutral medium and the cool neutral medium. The WNM is the dominant gas in galaxies and fills a significant fraction of a galaxy disk's volume. The WNM typically has temperatures of $T \approx 10^{3.7}$ K. The CNM on the other hand is atomic gas at temperatures ~ 100 K. The CNM has a much higher density than the WNM and occupies a much smaller fraction of the ISM volume. This atomic hydrogen gas can be studied with the 21-cm line which originates from the hyperfine splitting of the hydrogen ground state and is often called the hydrogen spin-flip transition.

Studying this line allows us to map the neutral ISM to study the morphology of galaxies and their star-forming regions. It also allows us to determine the galactic rotation curves, and measure the gas temperature, the gas column density, the total HI mass, and the kinematics of the galaxy.

Ionized gas in the ISM

The ionized ISM in galaxies is split into the hot ionized medium and the warm ionized medium. Coronal gas that has been shock-heated to $T \geq 10^{5.5}$ K by supernova explosions and collisionally ionized makes up the HIM. This gas is low density ($n_{\text{H}} \approx 0.002 - 0.004 \text{ cm}^{-3}$), on ~ 20 pc scales and cools on Myr time scales (Draine, 2011). The warm ionized medium is ionized hydrogen gas that has been photo-ionized by ultraviolet photons from hot stars. It can take the form of dense material from a nearby cloud in which case it is called an HII region or low-density intercloud gas called diffuse HII. Bright HII regions have dimensions of a few pc. Photoionized gas is also found in planetary nebulae which are created in the late stages of the evolution

of an intermediate mass star. When rapid mass loss during these stages the hot stellar core is exposed and the radiation from this core photoionizes the outflowing gas.

A thermal plasma is a partially ionized gas with temperatures ranging from 10^3 K to 10^8 K. Within these plasmas, there are three important transitions as discussed in Draine (2011) chapter 10. 1) Free–free transitions, where a free electron is scattered from one free state to another, with emission or absorption of a continuum photon. This emission is also called Bremsstrahlung emission or “braking radiation” as when the electron is scattered it is either accelerated or decelerated causing the emission of a photon. This emission is the dominant emission from HII regions in the radio frequencies. 2) Free–bound transitions, where an electron is initially free, but is captured into a bound state, with emission of a continuum photon. This is often called radiative recombination. 3) Bound-bound transitions, where an electron makes a transition from one bound state to another, with the difference in energy carried away photons. In a hydrogen plasma, many atoms will be found in high-quantum states called Rydberg states. These Rydberg levels can undergo spontaneous decay to lower levels. Transitions in very high energy levels yield radio lines, called radio recombination lines.

Molecular gas in the ISM

The molecular ISM is made up of diffuse and dense molecular gas. The diffuse molecular gas is similar to the CNM; however, it has a larger density allowing for H_2 self-shielding to occur, leading to an abundance of H_2 molecules at the cloud center. Self-shielding is a phenomenon where the photodissociation transitions of a molecule become optically thick so that the molecule in question is “shielded” from starlight by other molecules. In H_2 , the photodissociation channels are dominated by UV spectral line absorption rather than direct photodissociation allowing for this effect (Draine, 2011). Dense molecular gas is made up of gravitationally bound clouds, dark with substantial visual extinction. Within these regions, there are dust grains coated with

molecular ice. It is within these regions that star formation takes place. The dominant process for H₂ formation in molecular clouds is through grain catalyst (Draine (2011), (Wakelam et al., 2017)).

The most common way to study molecular gas is through molecular line emission, and the primary line used is the $J = 1 \rightarrow 0$ transition of CO. The reason we use this transition instead of H₂ is that the bulk of molecular hydrogen in a galaxy is cold ($\sim 10 - 20$ K) and therefore invisible. The first rotational level is more than $\Delta E/k_B = 500$ K above the fundamental level and as a result, we infer the presence of H₂ from the CO tracer (Draine, 2011). CO is the most abundant molecule after H₂ and its dipole moment is small resulting in CO being excited easily. While the CO 1-0 line is the best tracer of molecular gas it is also limited by radiative trapping effects and therefore to estimate the total molecular mass in a region from the CO luminosity we need a CO-to-H₂ conversion factor X_{CO} . While CO (1-0) is most often used to study molecular gas in galaxies it is challenging to detect in low metallicity environments and instead the [CII] 158 μm can be used instead (Madden et al., 2020).

Most of the gas and dust in a GMC are relatively cold. However, most GMCs have already had some star formation prior to the time when we observe them. Sites of recent star formation can be easily seen where one or more massive O or B-type stars have formed, photons emitted from these stars will cause photoionization and photodissociation of the surrounding gas. The photo-ionization will create an H II region visible in the radio as free-free emission or in the mid and far infrared. The photoionized gas will be overpressured and will drive a compressive wave or a shock wave into the molecular cloud. The interface between the H II region and the dense molecular cloud is called a photodissociation region (PDR). The PDR is illuminated by the CMB, galactic synchrotron radiation, $h\nu < 13.6$ eV radiation from the nearby O star, free-free radiation from the H II region, line emission from the H II region, and emission from the warm dust in the PDR (Draine (2011), Hollenbach and Tielens (1999)).

Dust in the ISM

Dust is now understood to play many critical roles in galactic evolution. By shielding molecules and by catalyzing the formation of the H_2 , dust grains are central to the chemistry of interstellar gas. Photoelectrons from dust grains can dominate the heating of gas in regions where ultraviolet starlight is present, and in dense regions, the infrared emission from dust can be an important cooling mechanism. Dust grains can be important in interstellar gas dynamics, communicating radiation pressure from starlight to the gas, and coupling the magnetic field to the gas in regions of low fractional ionization.

Dust in the ISM can also lead to extinction and reddening. Extinction is the absorption and scattering of radiation by dust and gas between an emitting source and the observer. This leads to both a decrease in the brightness of the emitting source and a “reddening” of its spectra. This reddening is due to the fact that extinction is higher for shorter wavelengths, causing more blue light to be scattered (Draine, 2011).

2.1.3 The Dynamic Interstellar Medium

The ISM is dynamic and undergoes changes of phase for many reasons; ionization can convert cold molecular gas to hot HII regions while radiative cooling can allow hot gas to cool to low temperatures leading to ions and electrons recombining to form atoms and molecules. The interstellar gas is primarily hydrogen with a small amount of heavy elements as a result of the return to the ISM of gas that has been processed through star formation and stellar explosions. Further effects on the ISM can be the result of the metallicity of the ISM, the interstellar radiation field (ISRF), stellar feedback, supernova feedback in the form of shocks and radiation, and dust abundance. Dust plays a role in setting the abundance of molecular gas by shielding heavier molecules such as CO from dissociating radiation as well as serving as the site of molecular hydrogen formation.

In star-forming galaxies, an appreciable fraction of the total luminosity of the galaxy is reprocessed through dense PDRs at the interface between molecular clouds and H II regions. Here, energy originally radiated by hot stars is absorbed by molecules and dust grains in the PDR, and reradiated at longer wavelengths as IR emission from dust and PAHs, and line emission from atoms and molecules in the gas. Part of the starlight energy goes into changing the physical state of the gas from cold and molecular to hot, photodissociated, and possibly photoionized if an ionization front is present. The entirety of the following sections on the dynamic interstellar medium including the interstellar radiation field, the effects of supernovae on the ISM, and shockwaves in the ISM is based on Draine (2011).

Shock waves in the ISM

A shock wave is a pressure-driven disturbance propagating faster than the sound speed of the medium it is propagating within. Shocks are common in the ISM, occurring due to stellar explosions - novae and supernovae drive shocks into the ISM. The gas in fast stellar winds and expanding HII regions can drive shock waves into surrounding neutral gas. The ISM in a star-forming galaxy is turbulent showing a complex morphology due to the injection of energy from stars. Stellar winds inject mass, momentum, and energy into the ISM, the ionizing radiation from the stars will create H II regions into which the wind will blow. This wind will drive a shock into the H II region.

The Interstellar Radiation Field

The physical state of interstellar gas is determined in large part by the interaction of the gas and dust with the radiation field. The ISRF is dominated by six components; synchrotron radiation from relativistic electrons which dominates the sky brightness at frequencies smaller than 1 GHz, the cosmic microwave background radiation which is very close to blackbody radiation with a temperature $T_{\text{CMB}} = 2.7255 \pm 0.0006$ K,

far-infrared and infrared emission from dust grains heated by starlight, free-free, free-bound and bound-bound transition emissions from plasma, starlight and finally X-ray emission from hot plasma.

Far-ultraviolet radiation from stars is of considerable importance in the neutral ISM, because it can (1) photoexcite and photodissociate H_2 and other molecules, (2) photoionize many heavy elements, and (3) eject photoelectrons from dust grains. The chemical and ionization state of the gas depends on the rates for photoionization and photodissociation. The thermal state is strongly affected by the heating effects of photoelectrons ejected from both atoms and dust grains. Dust grains are heated by the radiation field and reradiate the energy at longer wavelengths; the dust grain emission spectrum is determined by the spectrum and intensity of the radiation field to which the dust is exposed.

The effect of Supernovae on the ISM

The dynamic state of the ISM in the Milky Way and other galaxies is strongly affected by supernova explosions, their light, and their ejecta. The high-velocity ejecta has a dominant effect on the ISM, due to its velocity being much higher than the sound speed in the surrounding medium. As a result, supersonic shocks are driven into the circumstellar medium.

Supernova ejecta will pass through three phases before fading away. The first is called the free expansion phase and takes place in the first days after the explosion. Here the density of the ejecta is much higher than the density of the surrounding medium which allows it to expand at nearly constant velocity. There is one shock in this phase, a shock wave propagating outward into the medium. As the density of the ejecta begins to drop as it spreads out over a large area, the pressure of the shocked medium soon becomes larger than the pressure of the ejecta, and a reverse shock is driven back into the ejecta propagating inwards, slowing and heating the ejecta. The remnant now contains both an outward and an inward propagating shock front.

At some time later, the reverse shock has reached the center of the remnant, all of the ejecta is now very hot, and the free-expansion phase is over. The pressure in the supernova remnant is far higher than the pressure in the surrounding medium and the hot gas is emitting radiation. This is known as the Sedov-Taylor phase in the evolution of the blastwave. Initially, the radiative losses from the emitting hot gas are small, however, when they reach a level at which they are important, the blastwave will enter a “radiative” phase, where the gas in the shell just interior to the shock front is now able to cool due to radiative cooling to temperatures much lower than the temperature at the shock front.

This cooling causes the thermal pressure just behind the shock to drop suddenly, and the shock wave briefly stalls. However, the very hot gas in the interior of the SNR has not yet cooled, and its outward pressure forces the SNR to continue its expansion. This continued expansion is called the snowplow phase. During this phase, the mass of the dense shell propagating outward increases as it “sweeps up” the ambient gas. Throughout this phase, the shock front gradually slows, and the shock compression declines until the shock speed approaches the sound speed in the gas through which the blastwave is propagating. At this point, the shock wave turns into a soundwave and fades away as its speed reaches the sound speed in the medium.

Star Formation in Galaxies

Star formation occurs in molecular clouds with specific conditions, and this act of star formation as well as the effects from the newly formed stars can have a large impact on the ISM. For molecular clouds to begin forming stars a few conditions must be met: gravity must overcome the resistance of both the gas pressure and magnetic pressure, then nearly all of the angular momentum in the collapsing gas must be transferred to nearby material and finally, the observed magnetic fields of young stars require that most of the magnetic field lines initially present in the gas not be swept into the forming protostar (Draine, 2011).

In the case of giant molecular clouds (GMCs), the term *clump* is used to refer to self-gravitating regions that may or may not be forming stars. Star-forming clumps will generally contain several cores with each core likely to form a single star or a binary star. When a core becomes gravitationally unstable, it will begin to collapse, During the initial stages, radiative cooling in molecular lines can keep the gas cool and the gas pressure remains unimportant during this phase, and the matter moves inward nearly in free-fall. The infalling gas will generally have nonzero angular momentum, and the material will collapse to form a rotationally supported disk, with the material at the center with the lowest angular momentum collected in a “protostar”. The protostar will have a significant luminosity, allowing it and the surrounding core to be observed as a luminous infrared source (Draine, 2011).

Due to their effects on the ISM and galaxy formation, it is critical to know the rate at which stars are being formed within a region or galaxy, because massive stars are highly luminous and create bright HII regions we can use the observed number of HII regions photoionized by high mass stars, together with theoretical estimates of stellar lifetimes, to estimate the rate of star formation within a galaxy.

The metallicity of the ISM changes through star formation and stellar feedback. Through the life cycle of different mass stars hydrogen and helium are processed into heavier elements which can have an effect on the dust and gas in the ISM. Cormier et al. (2010) found that low metallicity dwarf galaxies have a lower dust abundance, and higher [C II]/CO ratios which promote large-scale photodissociation into the molecular reservoir. Madden (2001) and a later study by Madden et al. (2006) show the PAHs bands are faint when compared to larger dustier starburst galaxies and in these regions of faint PAH emission we find stronger radiation fields which contribute to the destruction of the PAHs.

2.2 Radio Astronomy

In this section, we will introduce techniques and terms used in radio astronomy, before discussing radio interferometry and practical radio imaging. First, we will introduce the common units and terms used in the field. Next, we will introduce the basic concepts of radio interferometry such as the coordinate systems and the equations to set up the imaging problem. Finally, we will discuss practical considerations when imaging in the radio regime. The following sections on radio astronomy and interferometry are based on *Essential Radio Astronomy* by Condon and Ransom (2016) and *Interferometry and Synthesis in Radio Astronomy* by Thompson et al. (2017). The subsequent sections on radio imaging are based on the CASA documentation (CASA Team et al., 2022).

2.2.1 General Radio Astronomy

Radio Units

In radio astronomy, a common unit used in describing both the flux density and specific intensity of a source is the Jansky. This is defined as $1 \text{ Jy} = 10^{-26} \text{ W m}^{-2} \text{ Hz}^{-1}$ and is used as the emission observed in radio wavelengths is often very dim. Specific intensity is defined as the power per unit area per unit solid angle per unit frequency or as the brightness per unit frequency and has units of $[\text{Jy sr}^{-1}]$ or $[\text{Jy beam}^{-1}]$. The beam is the solid angle on the sky that the telescope beams most of its power and is defined by the telescope and antenna properties. The flux density, however, is the integral of the specific intensity I_ν over the solid angle,

$$\text{Flux Density} = S_\nu = \int I_\nu d\Omega = \int I_\nu \sin \theta d\theta d\phi. \quad (2.1)$$

Therefore, it is defined as the power per unit area per unit frequency emitted by the source and has units of $[\text{Jy}]$ (Condon and Ransom, 2016).

Often, instead of specific intensity in units of $[\text{Jy beam}^{-1}]$, we use brightness tem-

perature in units of Kelvin [K]. Where the brightness temperature is not the temperature of the source but simply a scaled version of the specific intensity defined by

$$I_\nu = 2\frac{\nu^2}{c^2}k_B T_B. \quad (2.2)$$

This brightness temperature is the blackbody temperature that a source would have to have such that its brightness at frequency ν matches that of a blackbody (Condon and Ransom, 2016).

Emission mechanisms in the radio

Emission at radio wavelengths can be split into spectral lines and continuum emission. Continuum emission is comprised of two main components; thermal and non-thermal where the thermal sources are dependent on the temperature of the emitting source. The primary type of thermal emission we see in radio wavelengths is Bremsstrahlung or free-free emission from ionized H II regions.

The predominant non-thermal emission mechanism seen at these frequencies is synchrotron emission which is due to relativistic electrons spiraling around magnetic field lines and are often emitted from active galactic nuclei (AGN), pulsars, and supernova remnants (SNR).

There are many significant spectral lines visible in the radio wavelengths. Specifically in the L-band, we can see the famous hydrogen spin-flip 21-cm transition line which traces atomic gas. At 2.6 mm we can see the CO 1-0 line which is often used to trace molecular gas H₂. Finally, we can also see radio recombination lines which are transitions in very high energy levels and trace ionized gas.

Radio Interferometry

In radio astronomy, there are two types of telescopes, single-dish and interferometers. Single-dish telescopes are made up of one antenna while interferometers are collections

of many smaller dishes which work together to construct a larger diameter telescope. Both telescopes have their strengths: Single-dish telescopes can better recover large-scale diffuse emission while interferometers have a higher resolution and can resolve smaller sources.

The goal of radio astronomy is to map and measure the sky-brightness distribution which means resolving the emission on the sky. To resolve smaller sources we need a larger diameter telescope and due to the long wavelengths seen in radio astronomy, to obtain resolutions on the $1''$ scale we need telescopes with diameters that are kilometers long. This is practically and economically impossible and as a result, radio astronomers developed interferometry. This is a technique that takes many small telescopes and combines the signal received from each one to synthesize a large diameter. Of course, while we may synthesize a large diameter we don't get the same collecting area as one large telescope.

The basic concept in interferometry is that while a parabolic dish coherently sums all the light waves at the focus, the same result can be obtained by adding the signal received from individual elements (Condon and Ransom, 2016). To do this our antennas or sensors need to be able to convert Electromagnetic (EM) waves into a voltage that maintains all the information of the phase and amplitude of the incident wave.

In radio astronomy, what we measure is something called the complex visibility function $V(u, v)$ which is a function of baseline coordinates (u, v) . This coordinate system can be seen in figure 2.1 based on Figure 3.45 in Condon and Ransom (2016) where (u, v, w) are Cartesian coordinates oriented in such a way that the baselines lie on the $w = 0$ plane. Specifically, (u, v) represent East-West and North-South directions measured in wavelengths respectively. In this coordinate system w points towards the source, v points north, and u points east. The unit direction vector \hat{S} is defined by its projections (l, m, n) on the (u, v, w) axes these components are called the direction cosines and are defined by

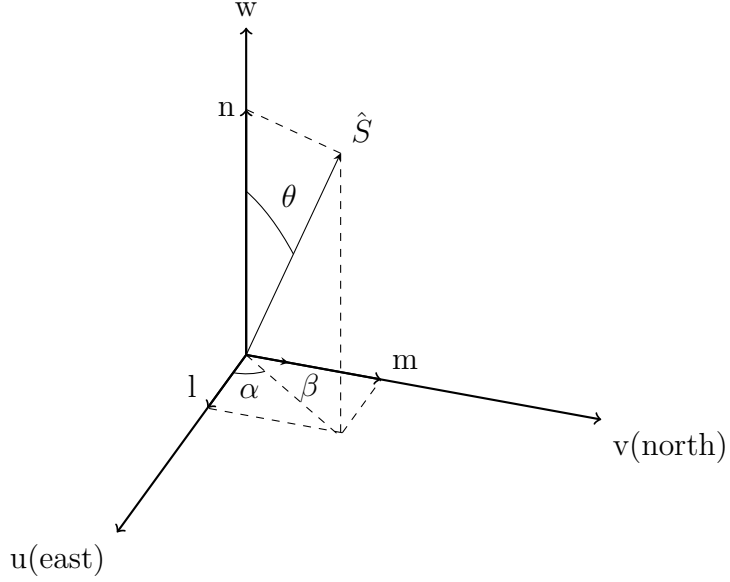


Figure 2.1: The (u, v, w) baseline coordinate system and (l, m, n) are the sky coordinates, which are a function of the baseline coordinates. The system is constructed so that w points towards the source, v points north, and u points east.

$$\begin{aligned}
 l &= \cos(\alpha) \\
 m &= \cos(\beta) \\
 n &= \cos(\theta) = \sqrt{1 - l^2 - m^2}.
 \end{aligned}
 \tag{2.3}$$

The visibility function is the Fourier transform (\mathcal{F}) of the sky brightness distribution $T(l, m)$ as a function of sky coordinates (l, m) ,

$$V(u, v) \xrightarrow{\mathcal{F}} T(l, m),
 \tag{2.4}$$

where l is E-W and m are N-S angles in the tangent plane in radians. Note that this is a spatial plane but does not describe the locations of the antennas.

Mathematically, the visibility is defined by,

$$V(u, v) = \int \int T(l, m) e^{-i2\pi(ul+vm)} dl dm,
 \tag{2.5}$$

and the sky brightness by,

$$T(l, m) = \int \int V(u, v) e^{i2\pi(ul+vm)} du dv.
 \tag{2.6}$$

$V(u, v)$ is a complex quantity with a real and imaginary part or with an amplitude and phase ($e^{ix} = \cos(x) + i \sin(x)$; Condon and Ransom, 2016; Thompson et al., 2017). The true sky brightness $T(l, m)$ is the inverse Fourier transform of the measured visibility function and is what we are trying to observe.

Therefore, (l, m) are coordinates in the sky plane and (u, v) are coordinates in the baseline plane or the “ u - v plane” and we can convert from one plane to the other with Fourier transforms. We measure $V(u, v)$ and we want to end up with $T(l, m)$ from the Fourier transform of $V(u, v)$. Since $T(l, m)$ is real $V(-u, -v) = V^*(u, v)$ and is thus Hermitian and we can get two visibilities from one measurement. Unfortunately, while we have the diameter of a kilometer-sized telescope we don’t have the collecting area so to mitigate this issue we move the antenna around into different configurations to cover or ”sample” the u - v plane.

Obtaining a good image of a source requires adequate sampling or coverage of the u - v plane. Gathering data in a snapshot of time with one baseline or one pair of antennas results in two (u, v) samples at a time. If we then increase the number of antennas we have to N antennas then we get $N(N - 1)$ samples at one time. Next, we can take advantage of the Earth’s rotation to fill the in u - v plane. Over 24 hours each baseline will trace an ellipse on the u - v plane gathering many more samples (Condon and Ransom (2016), Thompson et al. (2017)).

There are three caveats to sampling the u - v plane. The first is that there is an outer boundary and a resolution limit in which we have no information on smaller scales. This is dependent on the maximum baseline length of the interferometer. Second, even with many configurations and longer observing times, we cannot fully fill in this plane which leads to irregular coverage. We therefore call this the “sampling function” or in sky coordinates, the dirty beam. Finally, there is an inner boundary due to the fact that two antennae can only get so close together so there is a minimum separation in any configuration. This minimum separation leads to a gap in the center of the u - v plane and our sampling function which means we have no information on

larger scales. As a result, large diffuse low-column density gas is often resolved out and invisible to interferometers, because of this when working with interferometric data we often still require single-dish observations which can be combined with the high-resolution data.

As a result of the sampling function, by doing the inverse Fourier transform of the visibility function that we measure, it does not return the true sky brightness $T(l, m)$ and instead returns a “dirty image” $T^D(l, m)$ which is the true sky brightness $T(l, m)$ convolved (\star) with the “point spread function” $s(l, m)$,

$$T(l, m) \star s(l, m) = T^D(l, m). \quad (2.7)$$

The reason for this is that our data is not solely the visibility function $V(u, v)$ and instead, we have $V(u, v)S(u, v)$ where $S(u, v)$ is the sampling function and is a discrete function of where we measure or sample the u - v plane. The Fourier transform of $V(u, v)S(u, v)$,

$$V(u, v)S(u, v) \xrightarrow{\mathcal{F}} T^D(l, m) \quad (2.8)$$

returns the dirty image $T^D(l, m)$. The inverse Fourier transform of the sampling function,

$$s(l, m) \xrightarrow{\mathcal{F}^{-1}} S(u, v) \quad (2.9)$$

gives us $s(l, m)$ which is called the dirty beam or the point spread function.

2.2.2 Radio Imaging

Description of Imaging

As described in the previous section, in radio astronomy we measure the interferometers’ response to the sky brightness distribution (source brightness) called the complex visibility function. This visibility function is the Fourier transform of the sky brightness distribution which allows us to recover the source brightness from our measured response. However as previously discussed, The Fourier transform of the sampled visibilities yields the true sky brightness convolved with the point spread

function. Therefore, in order to get the true sky brightness we need to deconvolve the point spread function. This deconvolution process is the main goal of imaging. The following sections on radio imaging are based on the CASA documentation (CASA Team et al., 2022).

The imaging process and algorithms can be split into two steps, a major and a minor cycle. The role of the major cycle is to implement Fourier transforms between the data and the image spaces. While we can do the direct computation of Fourier integral by summation, this is very slow and not practical. Instead, we use FFT or the Fast Fourier Transform, which is much faster than the traditional Fourier transform but requires the data to be on a regularly spaced grid. The role of the minor cycle is to deconvolve the dirty beam from the sky brightness distribution in an iterative approach using one of many deconvolution algorithms. When deconvolving $s(l, m)$ from $T^D(l, m)$, we determine a model of $T(l, m)$ and recreate the sky brightness.

The deconvolution process uses non-linear techniques to interpolate/extrapolate $V(u, v)$ samples into unsampled regions of the u - v plane to find a plausible model for $T(l, m)$ and requires a priori assumption about $T(l, m)$. The dominant deconvolution algorithm used in radio astronomy is called clean and uses the assumption that $T(l, m)$ can be represented by point sources. Many variants of clean have been developed for computational efficiency and different use cases such as extended structure, wide-field, and wide-band imaging.

Practical Imaging Considerations

When imaging in radio astronomy with the Very Large Array (VLA) or the Atacama Large Millimeter/submillimeter Array (ALMA) the primary data processing tool used for imaging is the Common Astronomy Software Applications package (CASA, CASA Team et al., 2022). Within CASA there are many parameters one needs to consider, from calibrating data to choosing a deconvolution algorithm or taking wide field and wide band considerations into account. Here, we will summarize a few of the

considerations needed for making a high-quality radio image.

Before starting the imaging process we first need to calibrate and remove interference from our data. One unfortunate fact about working in the radio regime is the presence of Radio Frequency Interference (RFI). This is interference visible in radio astronomy observations due to terrestrial sources such as short-wave radio and telecommunications. Due to the weak signals observed in radio astronomy often these terrestrial sources are far brighter than the intended astronomical source and as a result radio astronomers have to flag and remove much of their data. This flagging process is often done as part of a Quality Assurance (QA) process or manually by the astronomer.

During the calibration step, we take instrumental and environmental properties into account. Many components contribute to the measured visibilities which can corrupt them. These effects can include ionospheric effects due to the charged particles and magnetic fields, tropospheric effects, linear polarization position angle, antenna voltage pattern, polarisation leakage, electronic gain, bandpass response, and geometry. Each component is generally separable and typically we do not need to solve for each of these in each observation. These components can be split into three categories, 1) Atmospheric effects 2) Hardware effects, and 3) Systematic effects.

To solve for calibration we first observe a known calibrator or a source for which we have a model. Calibrator sources have known properties and are good for identifying problems. A flux calibrator is used to set the flux scale of observations and is a source that has a well-known flux density. A bandpass calibrator is used to calibrate the frequency response of the system, in this case, the brighter the source the better and it is often the same source as the flux calibrator. Finally the gain calibrator, also known as the phase or secondary calibrator is used to derive complex gains (amplitude and phase) vs. time. This source must be located within a few degrees of the target and point sources are strongly preferred.

A priori calibration using external calibrators is not perfect because it is inter-

polated from a different time and a different sky direction from the source. The basic idea of self-calibration is to correct for antenna-based phase and amplitude errors together with imaging to create a source model. In practice this is an iterative, non-linear relaxation process where we first assume the source model, then solve for time-dependent gains and form a new source model from the corrected data using clean before finally solving for new gains. This method of calibration requires a sufficient signal-to-noise at each solution interval.

When we start imaging the first step is to choose a deconvolution algorithm. The standard Högbom clean algorithm is an adapted algorithm from Högbom (1974) and is the dominant deconvolution algorithm in radio astronomy. It takes the priori assumption that $T(l, m)$ is a collection of point sources. The first step in this algorithm is to identify the highest peak in the image as a point source, then subtract a fraction of this peak from the residual map and add this point source location and amplitude to a clean component list image. The algorithm then repeats this process iteratively until a stopping criterion is reached, such as an iteration count or the residual map maximum hits some threshold multiple of the RMS (Root Mean Square) noise in the image. Another deconvolution algorithm option is the Multi-Term Multi-Frequency Synthesis (MTMFS) algorithm. MTMFS is an improvement in the deconvolution algorithm that accounts for changes in the spectral index as a function of sky position and is often used in wide-field and wide-band imaging (CASA Team et al., 2022).

In the gridding process in preparation for the deconvolution minor cycle, other steps may occur beyond just gridding such as weighting, W-projection, or A-projection. Introducing a weighting function $W(u, v)$ in the gridding step modifies the sampling function $S(u, v) \rightarrow S(u, v)W(u, v)$ and changes the dirty beam shape $s(l, m)$. There are many weighting schemes but a few common ones are:

1. Natural weighting defined by

$$W(u, v) = 1/\sigma^2(u, v) , \tag{2.10}$$

where σ^2 is noise variance. This is best for point source sensitivity but results in lower resolution.

2. Uniform weighting defined by

$$W(u, v) = 1/\delta(u, v) , \quad (2.11)$$

where δ is the density of (u, v) points. This results in higher noise, higher resolution, and less dirty beam structure.

3. Robust (Briggs) weighting defined by

$$W(u, v) = \frac{1}{\sqrt{1 + S_N^2/S_{\text{thresh}}^2}} , \quad (2.12)$$

where S_N is the natural weight of a cell and S_{thresh} is a threshold value set by the astronomer. This weighting scheme combines noise and density of points and has an adjustable parameter “robust” (S_{thresh}) between -2 and $+2$ where -2 is natural weighting and $+2$ is uniform weighting. This allows us to obtain most of the natural weight sensitivity at the same time as most of the uniform weight resolution.

The W -term is a part of the real measured visibilities which have many terms based on effects such as direction-independent gains, the u - v sampling function, direction-dependent effects, and effects of how the sky brightness varies with frequency in time. Within these time-varying effects is the W -term. This W -term is an effect of the sky curvature and is a known geometric effect due to the non-coplanar baselines and sky coordinates. Standard 2D imaging applied to such data will produce artifacts around sources away from the phase center. The primary way of dealing with the W -term is to apply W -projection which is a wide-field imaging technique that takes into account the non-coplanarity of the baselines as a function of distance from the phase center, this is applied at a specified number of W -project planes (Cornwell et al., 2008).

The A-term is the Antenna term and is due to the sky brightness being multiplied by the primary beam before being sampled by each baseline. The goal of A-projection is to remove the frequency dependence of the primary beam during the gridding step so that the minor cycle sees the spectral structure of only the sky. In AW-projection, we take both the W-term and A-term into account and need to correct for the A-term at each W-project plane. The result of this computationally expensive process is more accurate spectral index values far from the image center (Bhatnagar et al., 2013).

To obtain or recover short-spacing information in an interferometer there are a couple of options. The first option is to include single-dish data. Using a large single-dish telescope we can sample all Fourier components from 0 to D , where D is the dish diameter. We can then combine our single-dish data with the interferometer data. The second option is to use a separate array of smaller antennas. Small antennas can observe shorter baselines inaccessible to larger dishes as they can physically get closer to each other.

In radio astronomy, we get to decide the pixel and image size and in practice, we generally use a pixel size such that we have 3 - 5 pixels across the main lobe of the dirty beam. For the image size, the default choice is the full extent of the primary beam. However, if there are bright sources outside the image in the side lobes then the FFT algorithm will alias them into the image creating artifacts. Instead, we can either make the image larger so the bright sources are included in the cleaning process or we can create outlier fields around the bright sources so that the image doesn't get any larger but the bright sources are dealt with properly.

Finally, during the imaging process, it is worth considering how each parameter affects the image quality. This can be done by measuring the dynamic range. The dynamic range is the ratio of peak brightness in an image to the RMS noise in a region devoid of emission and is an easy way to calculate a lower limit to the error in brightness in a non-empty region. A higher dynamic range is better.

Chapter 3

IC 10 Literature Review

IC 10 was first discovered in 1887 by Lewis Swift and was first believed to be part of the Milky Way. Later, astronomers thought it may be extragalactic and Hubble thought it was part of the Local Group, which was confirmed decades later in 1996 (Roberts, 1962; de Vaucouleurs and Ables, 1965). Its radial velocity was originally measured in 1941 and has since been narrowed down to ~ -350 km/s (Hunter et al., 2012). The neutral hydrogen 21-cm emission in IC 10 was studied as far back as 1960 but was more extensively studied through the 1990s most notably by Wilcots and Miller (1998). Its position is close to the Galactic plane (-3.3 degrees galactic latitude), which makes it difficult to measure the distance however recent estimates find IC 10 is ~ 0.7 Mpc away (Hunter et al., 2012). It is located in the constellation Cassiopeia with an approximate apparent size in the optical to be $\sim 7' \times 6'$. In the 21-cm emission, IC 10 can be seen to have an extended HI envelope spanning almost a degree in the sky (Ashley et al., 2014; Namumba et al., 2019).

IC 10 is the nearest starbursting galaxy as evidenced by its high H α luminosity (Wilcots and Miller, 1998) and its extremely high surface density of Wolf-Rayet (WR) stars. The galaxy has a star formation rate of $\sim 0.045 - 0.07 M_{\odot} \text{ yr}^{-1}$ (Tehrani et al., 2017), which is comparable to the SMC. However, IC 10 displays a much higher star formation intensity $\sim 0.049 M_{\odot} \text{ yr}^{-1} \text{ kpc}^{-2}$ than the SMC due to IC 10's lower mass. The number of WR stars in IC 10 is over twice as high as any other Local Group

galaxy and 5 times higher than the SMC, The disk contains 15 WR while 1 WR star is typical for a star-forming dwarf galaxy (Ashley et al., 2014).

The current starburst in IC 10 likely started 10^7 years ago which is evidenced by optical studies revealing numerous HII regions (Hodge and Lee, 1990). With lower abundances of carbon and oxygen, harder radiation fields due to the lower metallicity, and lower abundances of dust to shield the molecular gas and increase extinction, dwarf galaxies may be expected to display a different relationship between atomic neutral gas, molecular gas, and star formation than other galaxies (Leroy et al., 2006).

In the following sections Figures 3.1, 3.2 and 3.3 showcase LGLBS data for the purpose of a visual aid when discussing previous research. This data is not necessarily the same data as discussed in the literature and may not show the same emission and features. Further information on the LGLBS data can be found in Chapter 4.

3.1 The 21-cm Atomic Hydrogen gas in IC 10

From many studies of IC 10 including Wilcots and Miller (1998); Shostak and Skillman (1989) and newer studies such as the LITTLE THINGS survey by Ashley et al. (2014), we know that IC 10 has an unusual neutral hydrogen distribution, turbulent kinematics, and complex morphology. We see a large hydrogen envelope $\sim 70'$ in size containing a much smaller and higher column density neutral disk and intermediate-sized ($\leq 10'$) extensions. These extensions have a unique velocity distribution as they appear to be rotating counter to the direction of the central disk. Within this central disk, we see a complex morphology full of large holes and shells in the HI structure along with a large primary cloud containing most of the galaxy's multi-wavelength emission.

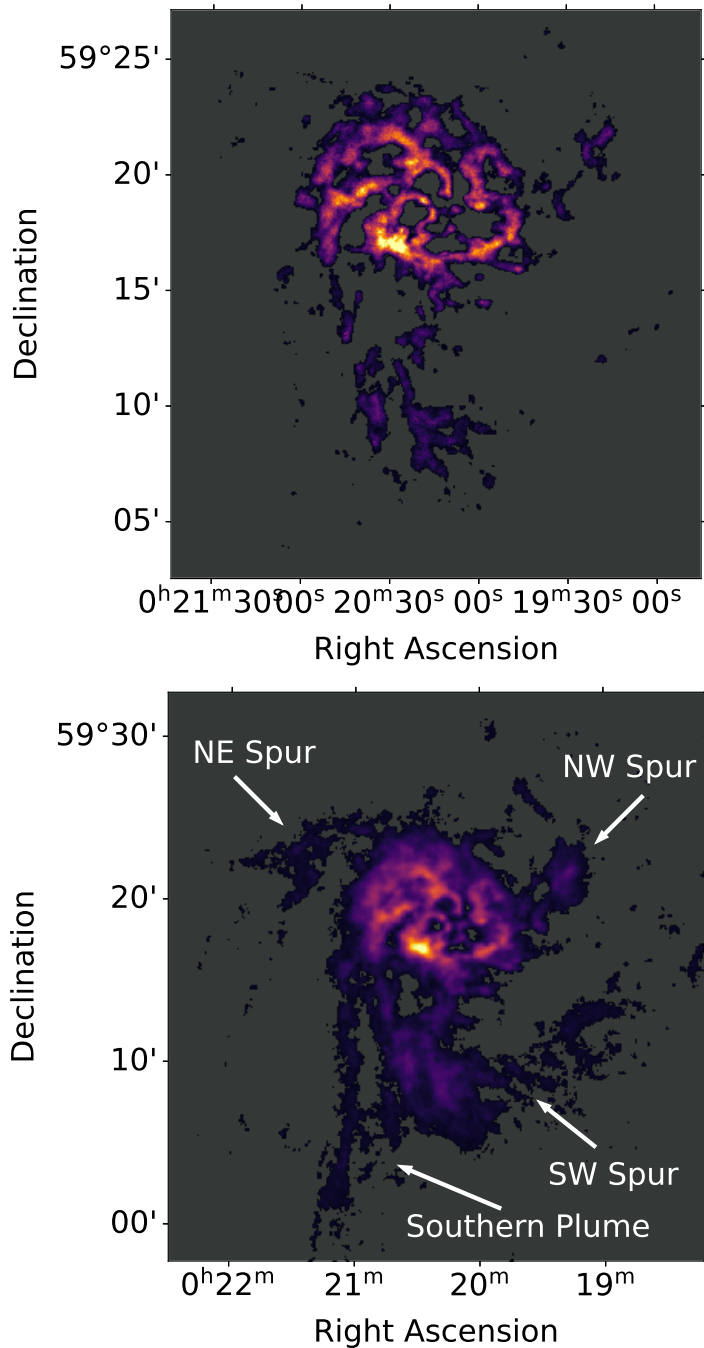


Figure 3.1: LGLBS VLA HI 21-cm Integrated Intensity maps. The top panel shows the 4 configuration A+B+C+D high spatial resolution $\sim 4.5''$ map which displays many holes and shells visible in the disk. The bottom panel shows the lower resolution $\sim 19''$ C+D configuration map which displays the diffuse low column density gas and the large HI extensions, labeled as the three “spurs” and one “plume.” This figure is intended as a visual aid when discussing previous research on the HI emission in IC 10, more details on the data are available in chapter 4.

3.1.1 The Neutral Disk of IC 10

IC 10’s main atomic disk can be seen in figure 3.1 where the upper panel displays the high resolution $\sim 4.5''$ VLA data which shows a clearly chaotic and storied past. Wilcots and Miller (1998) attempted to describe this disk by labeling and characterizing the holes in the disk. To do this they used both intermediate and low-resolution data as the higher resolution data tends to resolve out the large-scale features they were interested in as well as over-estimating the number of holes in the HI due to a poorer sensitivity. While analyzing the data they described the distribution as dominated by clumps, ridges, and filaments of high column density gas. They also described the gas outside the disk and identified a “streamer”, a “plume” and two “spurs” which will be further discussed in section 3.1.2. For now, it is worth noting that these extensions contribute to a complex velocity distribution in the disk where the extensions are counter-rotating with the central gas.

The holes in IC 10’s main disk are of interest due to their likely origins in stellar feedback and the effects of massive star formation on the interstellar medium. This is an active area of research in dwarf galaxies and IC 10’s high star formation rate makes it an excellent target to study. The combination of stellar winds from massive stars and their supernovae explosions will deposit energy into the ISM, ultimately creating bubbles of hot gas surrounded by neutral gas. Wilcots and Miller (1998) find seven holes in the disk of IC 10 with diameters ranging between 100 - 300 pc in size and with ages of $\sim 1 \times 10^7$ yr. Based on these sizes, ages, and velocities they suggest the holes are created by 1 - 3 supernovae. Wilcots & Miller quantify these holes by regions of low HI column density but more specifically as regions with double-peaked velocity profiles corresponding to the approaching and receding sides of the shell.

Ashley et al. (2014) further investigated the holes in IC 10’s disk with higher spatial ($\sim 6''$) and velocity resolution ($\leq 2.6 \text{ kms}^{-1}$) data. They verified the existence of the holes by detecting them in at least three consecutive channel maps. In their study,

they found 20 “high quality” HI holes with diameters 46 - 250 pc. They confirm the existence of the previously found seven holes from Wilcots and Miller (1998) and found that the previously found large holes contain two or more smaller holes and some of them overlap. They also classified each hole into one of three types:

1. Empty cavities that have no detected HI along the line of sight
2. Holes with HI on either the near or far side of the cavity
3. Holes that have HI detected on both the near and far side but have an empty cavity in the center similar to Wilcots and Miller (1998) double-peaked velocity profile method of hole identification.

Ashley et al. (2014) then found the age range for IC 10’s holes with at least one side on the line of sight intact to be between 1 Myr to 7.6 Myr. This indicates that the second and third types of holes are quite young and the stellar components that made them should still be visible in the $H\alpha$ emission. Unfortunately, due to a limited $H\alpha$ map, it is not possible to compare all of the holes to the $H\alpha$ emission.

As previously mentioned, along with the holes and shells in the HI structure, the disk also contains a large cloud of higher column density HI which when compared to the multi-wavelength data contains the most luminous HII regions (Magrini and Gonçalves, 2009), nearly half of the Wolf-Rayet stars (Ashley et al., 2014), the brightest molecular clouds (Leroy et al., 2006) and large scale $H\alpha$ (Wilcots and Miller, 1998). The cloud also contains a large non-thermal superbubble and its possible progenitor an X-ray binary IC 10 X-1 (Yang and Skillman, 1993; Silverman and Filippenko, 2008). This cloud contains the majority of the star-forming regions in the dwarf. When compared to the rest of the disk, the eastern and western sides don’t show much star formation and it is concentrated towards the center (Wilcots and Miller, 1998). This cloud can be seen in our data towards the bottom of the disk in figure 3.1 above the SW spur with the brightest emission.

3.1.2 HI Extensions in and around IC 10

When looking at the neutral 21-cm HI emission morphology, we can see two regions of interest: The inner atomic disk of the galaxy containing the majority of the dwarf star formation regions, and multiple extensions extending off of (or into) the inner disk.

These extensions can be seen in the bottom panel of figure 3.1. This figure shows both the high and low-resolution VLA maps of the 21-cm emission in IC 10. The upper panel shows the high-resolution map which displays the holes and shells within the disk while the lower panel shows the low-resolution map which displays the diffuse HI emission and large extensions. The atomic disk is about $12'$ across compared to the $\sim 6' - 7'$ of the visible galaxy and in the bottom panel, we can see extensions extending about $36' \times 30'$. These are the “intermediate” sized extensions made up of the southern plume extending $\sim 3''$ to the south and three spurs. The spurs are the smaller extensions closer to the disk and are made up of the SW spur, NW spur, and NE spur. Figures 2,3 and 4 of Ashley et al. (2014), show the inner disk of the galaxy with visible band contours, the same intermediate extensions, and a large HI envelope which takes up about 1° on the sky.

The inner disk is represented well by a nearly solid body circular rotation at ~ 30 km/s and looking at the central velocity Moment 1 map in figure 2 from the LITTLE THINGS survey (Ashley et al., 2014) as well as in our data in figure 4.9, we can see that the spurs and southern plume are counter-rotating when compared with the disk of the galaxy. The SW spur for example, on the western edge we see a velocity of ~ -320 kms^{-1} and as we move east towards the disk it changes to ~ -400 kms^{-1} nearer to the disk. Similar patterns can be seen for each of the spurs and the larger southern plume with a velocity gradient increasing towards the disk with higher velocities.

The last extension to mention was found at a later date with a Green Bank tele-

scope observation by Nidever et al. (2013). The single-dish observations have a lower resolution but are able to resolve the larger extended structure. Visible in these new diffuse gas observations is a very large HI extension to the NW coming out of the large HI envelope. This diffuse extension was then confirmed by another study by Namumba et al. (2019) with the Dominion Radio Astrophysical Observatory Synthesis Telescope (DRAO).

These extensions have been well studied by many authors, with many theories of their origins, their velocities, and their relation to the ongoing starburst in IC 10. Here, we will briefly describe the potential origins of these extensions.

The first potential cause for these velocity profiles is a ring model for a warped structure in a normal rotating disk. This was first proposed by Cohen (1979) where he suggested that the large envelope represents a warped gas layer oriented nearly edge-on which makes it seem like there is counter-rotating gas when in reality it is non-existent. This model can be seen in Figure 3 of Cohen (1979) drawn schematically. Visible in the figure is a three-ring structure where the inner ring is angled such that the eastern edge is closer to the observer while the outer ring is the opposite with the eastern edge closer and an intermediate ring somewhere in between. This shows how a warp can give the illusion of counter-rotating gas. However, it was later found from the HI distribution that the disk is oriented at roughly 45° and not face-on (Shostak and Skillman, 1989). We would also expect to see at least one “ring” near the systemic velocity which we do not observe. The complex velocity dispersion seen in and around the disk showing randomly oriented velocity fields also argues against any stable tilted ring configuration.

The next few theories involved interactions with other galaxies, including a possible interaction with M31, an interaction with another dwarf galaxy or IC 10 itself is an advanced merger between two dwarf galaxies. It is possible that IC 10 may have interacted with an outside source such as a galaxy in the M31/M33 group with M31 being the closest and most likely candidate with a relative distance of about 250 kpc

and relative velocity of 48 km s^{-1} .

Brunthaler et al. (2007) measured the proper motions of IC 10 from VLBA masers which allowed Nidever et al. (2013) to produce an accurate model for its orbit using GBT measured radial velocity. This can be seen in Figure 2 of Nidever et al. (2013), where the HI extension is leading IC 10 in its orbit, therefore this extension cannot be caused by ram pressure stripping from an interaction with the M31 halo or the intergalactic medium because ram pressure stripping causes trailing tails. This “interaction with M31 theory” has also been discussed by Ashley et al. (2014). They found that IC 10’s spurs do not originate from IC 10’s main disk due to their increase in velocity dispersion as they join the disk and due to the inverse velocity to the disk. Therefore, this situation would involve IC 10 gaining the northern extension from M31 and it is now accreting onto IC 10 and the southern plume is a tidal tail coming from IC 10’s main disk.

However, the timescale for these two galaxies interacting was found to be $\sim 5 \text{ Gyr}$ and the accretion time for the southern plume is $\sim 0.4 \text{ Gyr}$ and $\sim 0.6 \text{ Gyr}$ for the northern extension. They concluded that it does not seem likely that IC 10’s northern extension and southern plume could retain their extended structure for 5 Gyr after an interaction with M31.

Finally, simulations for an IC 10 - M31 interaction done by Namumba et al. (2019) found that most of the simulations do not show any clear tidal features in the final state of the IC 10 gas disk in nine simulations. Only one simulation did and the stream-like feature that is visible is much larger than the one visible in the HI disk of IC 10 and when shown at the larger scale of the DRAO observations shows no tidal features at all.

The higher column density region at the end of the HI extension visible in the Ashley et al. (2014) VLA observations and the Namumba et al. (2019) DRAO observations is a potential candidate for an interacting dwarf galaxy. This theory is nice as it would naturally explain the starburst and possibly the counter-rotating gas in

the outer regions of IC 10 as they could either be disturbed by the interaction or accreting from the companion. It would also answer how an isolated galaxy such as IC 10 could have triggered its starburst to become a BCD.

Evidence for this theory would be a stellar component associated with the HI extension however, this has yet to be observed due to most of the optical and near-infrared surveys of IC 10 focusing on the stellar populations in the central disk and much smaller visible region of IC 10. There is also the added difficulty of IC 10's proximity to the Galactic plane with lots of dust to obscure the stellar light. Stellar population studies will be discussed further in section 3.4. Along with a lack of a stellar component, we also observe no obvious tidal arm on the other side of the companion which would be expected if the higher-density region at the end of the extension was another dwarf galaxy.

Another interaction scenario is that IC 10 may be an advanced merger itself with two tidal tails, the northern extension and the southern plume. This is suggested in the Ashley et al. (2014) study. They describe two peaks in the center of the GBT data one corresponding to IC 10's main disk and the other potentially a remnant from a past companion. They argue that, depending on the properties of the interaction and the two galaxies interacting, a tidal feature can appear to be spiraling as a merger occurs; and it is possible for a lower mass galaxy to quickly merge with the larger mass galaxy before the tidal tails dissipate. Following the radial line of sight velocities in the GBT data, they argue they transition from the NE extension into the main body of IC 10 before spiraling counterclockwise in towards the center of the galaxy, indicating that much of the velocity field could be tracing a tidal feature. In this case, the spurs would be from the tidal feature and not from IC 10 with a morphological counterclockwise rotation of the spurs around IC 10's main disk. In this scenario, they suggest the southern plume could also be a second tidal tail seen from an extreme projection angle originating from IC 10's main disk.

Another potential origin is that stellar feedback from the starburst formed the

HI extensions. However, the high number of Wolf-Rayet stars and lack of young red supergiants indicates the starburst is quite young at roughly 10 Myr. The NW extension is about 18 kpc long and the Southern plume is about 7 kpc long therefore, for stellar feedback to form these extensions in 10 Myr it would require an outflow velocity of ~ 1800 km/s for the NW extension and ~ 700 km/s for the plume, which is unreasonably high and unlikely. In a more recent stellar cluster paper, Lim and Lee (2015) it was suggested that IC 10 had two starbursts, a recent one starting ~ 10 Myr and an earlier one ~ 100 Myr. Taking this time into consideration it reduces the outflow velocity needed to roughly 180 km/s which is much more reasonable.

The final possible mechanism for the formation of these HI extensions is that IC 10 is still forming and accreting primordial gas. In Ashley et al. (2014), they explain that cold accretion is the dominant form of intergalactic medium accretion in low-mass galaxies and the filaments accrete essentially in free fall. The infalling gas accretion rate in the north is ~ 0.6 Gyr to finish accreting and ~ 0.2 Gyr in the south. This rate in the south is close to being able to account for the high star formation rate ($\sim 0.045 - 0.07 M_{\odot} \text{ yr}^{-1}$) seen in IC 10 and could be fueling the starburst. Finally, they suggest the southern plume could also be an accretion filament. The plume is redshifted so therefore the gas would have to be accreting onto the main body from the near side of the disk.

Namumba et al. (2019) indicate that the HI extensions with different kinematics seen in the south, east, and west of the main core may be the result of accretion due to counter rotation of the disk and by the increase in velocity dispersion observed at the point of contact of those regions with the inner regular disk. The combined mass of the counter-rotating HI and HI extension is $\sim 3 \times 10^7 M_{\odot}$. However, there is no observational evidence of a population of $\geq 10^7 M_{\odot}$ HI clouds in intergalactic space fueling star formation. Although smaller clouds could exist in the IGM and be accreted. If the counter-rotating gas and extension are from cold accretion alone, then we would expect the gas filament to be fairly massive.

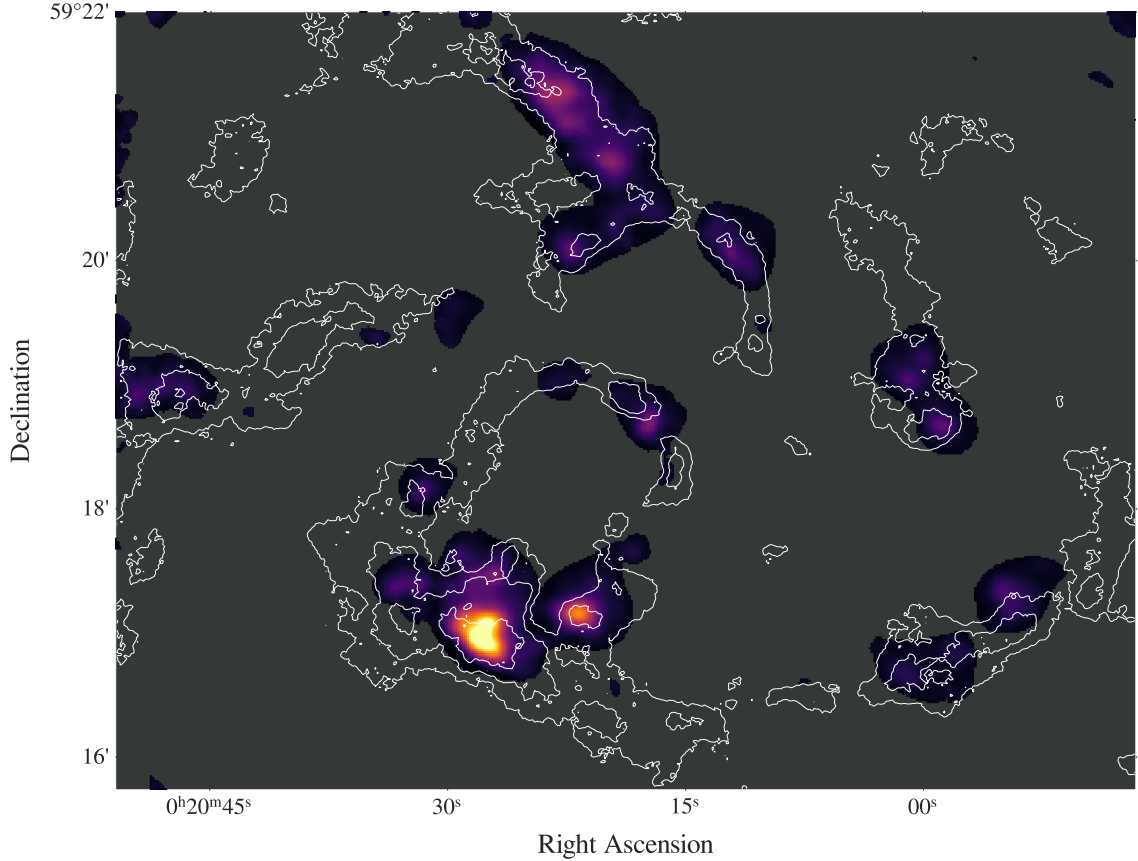


Figure 3.2: LGLBS CO (1-0) IC 10 integrated intensity map [K km/s] with HI integrated intensity contours overlaid. The HI contours are at levels 800, 1500, and 2500 [K km/s]. Within this figure, we can see giant molecular clouds coincident with the high column density HI. The brightest CO emission is concentrated within the large HI cloud at the bottom of the figure and along HI shells. This figure is intended as a visual aid when discussing previous research on the molecular gas in IC 10, more details on the data are available in chapter 4.

3.2 Molecular Gas in IC 10

The molecular gas in IC 10 has not been studied as extensively as the 21-cm emission. The LGLBS CO (1 - 0) data with HI contours can be seen in figure 3.2 for the purpose of this discussion. In Ohta et al. (1988), CO clouds were detected in star-forming regions corresponding to HI peaks. They also found these clouds to be located at the edge of the optical galaxy. Later, Wilson and Reid (1991) found three molecular clouds in IC 10 with velocity, line widths, diameters, temperatures, and masses similar

to Galactic giant molecular clouds (GMCs). In a follow-up study, in Wilson (1995) found six additional GMCs with again similar properties to Galactic GMCs. However, in this initial work, they found the virial masses were substantially larger than the molecular masses of the clouds and used a distance of 1 Mpc for IC 10, this led to an over-estimation in the CO-to-H₂ conversion factor finding a result indicating the CO-to-H₂ conversion factor increases by a factor of 4.6 as the metallicity of the galaxy decreases by a factor of 10.

Leroy et al. (2006) presented a new survey of CO(1 - 0) emission with higher sensitivity and resolution than previous work allowing the detection of individual giant molecular clouds. This survey detected 16 clouds and measured their properties to find once again that they are similar to Galactic GMCs in their sizes, line widths, and luminosities. Contrary to previous work, they found similar CO-to-H₂ conversion factors to Galactic GMCs despite the galaxy's low metallicity. One would expect a low metallicity to lead to an increase in the Interstellar radiation field, as a result, molecules may be dissociated faster, and as H₂ can self-shield while CO is dissociated this may affect the CO-to-H₂ conversion factor. However, in this paper they found that virial mass is much closer to the luminosity mass or the molecular mass as found in Wilson (1995), leading to the finding that the CO-to-H₂ conversion factor does not differ significantly from the Galactic value and noting that the discrepancy is due to Wilson (1995) fluxes representing an outlier from other interferometric data. Finally, they once again found that most of the CO emission is coincident with the high surface density HI, but that the hydrostatic gas pressure was better at predicting the CO along a line of sight than the HI column density alone.

These results were further supported by Blitz and Rosolowsky (2006) and Bolatto et al. (2008) where they both found giant molecular clouds in Local Group galaxies were correlated with HI filaments and no metallicity trends in the CO-to-H₂ conversion factor and that the Galactic conversion factor is a good value to use for most galaxies. Concluding that GMCs identified by their CO emission have a uniform set

of properties from galaxy to galaxy.

The galaxy has a star formation rate of $\sim 0.045 - 0.07 M_{\odot} \text{ yr}^{-1}$ (Tehrani et al., 2017), which is comparable to the SMC. However, IC 10 displays a much higher star formation intensity $\sim 0.049 M_{\odot} \text{ yr}^{-1} \text{ kpc}^{-2}$ than the SMC due to IC 10's lower mass.

Finally, IC 10 displays more star formation per molecular or total gas surface density than large spiral galaxies and at a SFR of $\sim 0.045 - 0.07 M_{\odot} \text{ yr}^{-1}$ (Tehrani et al., 2017), the depletion time for the molecular gas associated with CO in IC 10 is $\sim 4 \times 10^7$ yr, compared to the median depletion time of $\sim 2 \times 10^9$ yr found in nearby dwarf galaxies (Leroy et al., 2006). This has been suggested by Leroy et al. (2006) to be a timing effect, and we may be observing IC 10 just after a peak in the starburst and star formation rate so that the tracers of this star formation are still present but the molecular gas has already been somewhat depleted. Another option is that IC 10 has more H_2 than we can infer from the CO emission and a higher CO-to- H_2 conversion factor. Madden et al. (1997) mapped IC 10 in the first complete [C II] map of an entire low-metallicity galaxy. [C II] emission is associated with PDRs found at interfaces between H II regions and giant molecular clouds. They found in certain regions of IC 10 that the minimum amount of hydrogen needed to produce the observed [C II] emission implies the presence of an additional column density of H_2 and they suggested that in parts of IC 10, the UV field and low metallicity create a situation where small CO cores are surrounded by larger [C II] envelopes where molecular hydrogen is self-shield and abundant. Bolatto et al. (2000) considered and rejected the possibility of a large reservoir of cold molecular gas in that region. Although later papers use the Galactic CO-to- H_2 conversion factor the possibility for a large reservoir of hidden warm molecular gas outside the central bright GMCs has not been strictly ruled out however, it would be unlikely for a reservoir of H_2 to have the physical conditions to support star formation and remain hidden.

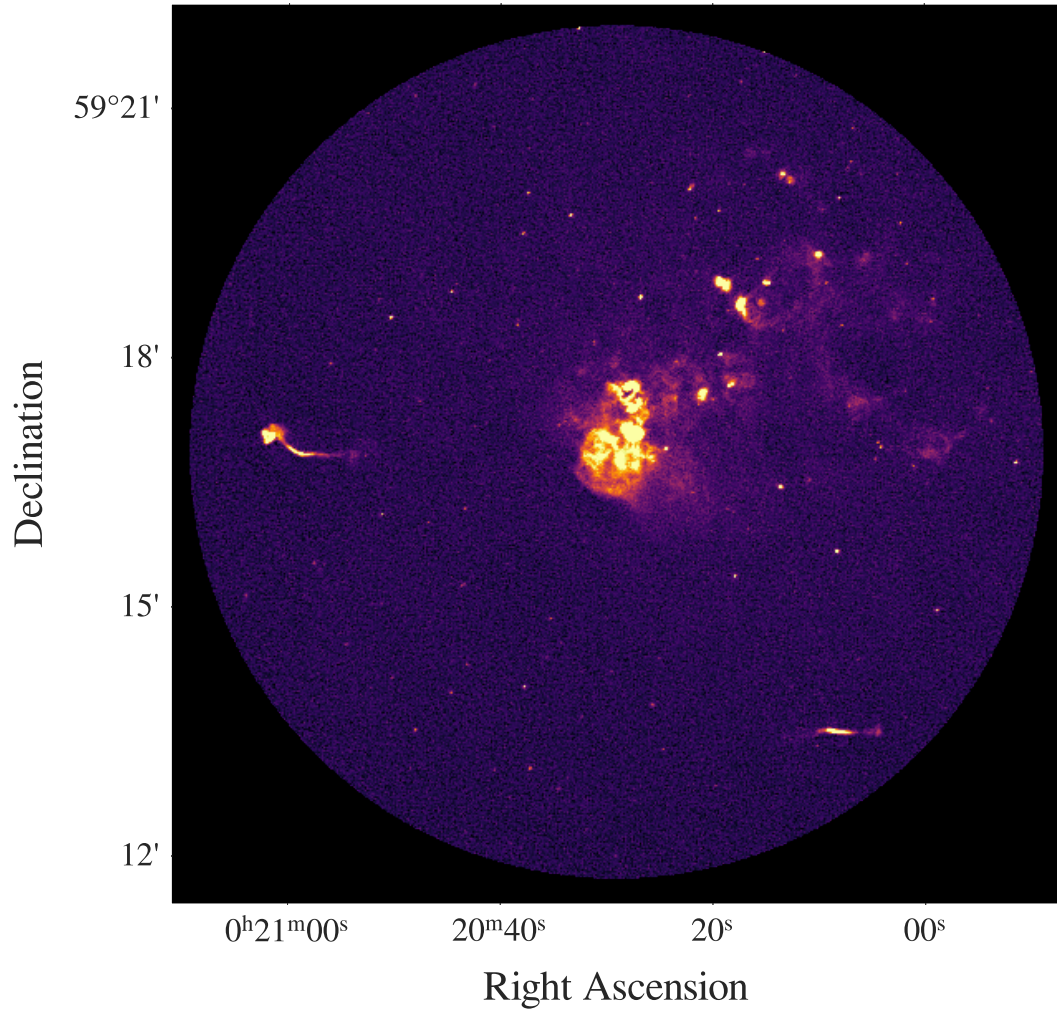


Figure 3.3: LGLBS IC 10 1.5 GHz L-band continuum image with a spatial resolution of $\sim 1.5''$. At the center of the figure, we can see a large non-thermal superbubble and throughout the region many compact continuum sources. This figure is intended as a visual aid when discussing previous research on the continuum emission in IC 10, more details on the data are available in chapter 4.

3.3 IC 10 in the Radio Continuum

Yang and Skillman (1993) presented radio continuum observations at 6 cm (~ 5 GHz), 20 cm (~ 1.5 GHz) and 49 cm (~ 0.6 GHz). They detected and measured the flux and spectral index of a number of resolved radio sources in the galaxy and found most to be thermal emission from H II regions and some non-thermal background sources. However, they found one extended, non-thermal source which appeared to be a superbubble in IC 10. They found the size of this non-thermal SuperBubble (NTSB) to be ~ 250 pc which implies it is most likely the product of several supernovae. Comparisons with H α , HI, and optical imaging show that the superbubble is associated with the most massive HI cloud in IC 10 which also contains two of the brightest HII regions seen in the galaxy and two Wolf-Rayet (WR) stars. The LGLBS radio continuum 1.5 GHz data can be seen in Figure 3.3 and also shows the large NTSB. Yang & Skillman originally ruled out a single supernova remnant (SNR) to be the source of the Superbubble because of its large size and its proximity to the biggest H II regions in IC 10. Instead, they considered up to as many as 10 SNRs created this NTSB. While comparing with HI and H α emission, they didn't find an HI hole or an H α shell indicating it is at the early stages of its formation, and considering that the size of the HI complex the bubble is located in, this superbubble could expand to a size of ~ 1 kpc.

Lozinskaya and Moiseev (2007) suggest this superbubble could be the result of a large hypernova explosion instead of multiple supernova explosions. Arguing that due to the very high kinetic energy of the shell, the presence of a bright extended and spherically symmetric source of synchrotron radiation which is difficult to explain with many supernovas, as well as the presence of a compact remnant of the explosion of a very massive star, IC 10 X-1, that it is more likely to be formed from a single large hypernova explosion rather than many supernovae.

Heesen et al. (2015) combined data from the VLA and the Effelsberg telescope and

subtracted the thermal emission using a combination of Balmer $H\alpha$ maps and VLA 32 GHz continuum maps. They found the NTSB’s non-thermal spectrum between 1.5 and 8.8 GHz displays curvature, and based on the spectral curvature, the spectral age of the bubble was found to be 1.0 ± 0.3 Myr. When comparing to the LITTLE THINGS HI data (Ashley et al., 2014) They found an expanding HI hole moving at ~ 15 km/s within 16 pc of IC 10 X-1, a massive stellar-mass black hole ($M \geq 23 M_{\odot}$). Based on these results, Heesen et al. (2015) found that a single energetic explosion of the progenitor of IC 10 X-1 released 10^{52} ergs, accelerating the non-thermal particles and the HI shell at the same time to be the most likely scenario. This slow shell velocity of ~ 15 km/s is consistent with the idea that the last SN exploded 1 Myr ago. They suggest as before that we are observing the NTSB in the early stages of its evolution and it may increase in size and eventually be visible as a large HI hole.

Silverman and Filippenko (2008), showed that IC 10 X-1 is a WR/Black-hole binary containing one of the most massive known stellar mass black holes with a mass of 23 - $32.7 M_{\odot}$. This was done by studying the optical counterpart of IC 10 X-1, a Wolf-Rayet (WR) star. Through new spectra of the WR star, they found a shift in the He II emission line from which they calculated a period, a radial-velocity semi-amplitude, and a mass function for the binary system. This combined with the previously estimated mass of the WR star of $35 M_{\odot}$ yields a primary mass of $32.7 \pm 2.6 M_{\odot}$; and even with a WR star mass of only $17 M_{\odot}$, it yields a primary mass of $23.1 \pm 2.1 M_{\odot}$.

Heesen et al. (2011) used the Very Large Array to study the radio continuum emission at 6 cm or 5 GHz in the C-band of the VLA at a linear resolution of ~ 50 pc. They confirm and clearly resolve polarized emission associated with a non-thermal superbubble and they found close agreement between the radio continuum and $H\alpha$ emission. They found the radio continuum peaks at the location of the $H\alpha$ emission that traces HII regions, this close correlation between the radio continuum and the $H\alpha$ emission suggests a large fraction of thermal radio emission is from

free-free emission. Studying, the radio spectral index of the compact sources, the thermal emission was found to have a radio spectral index of $\alpha = -0.1$ to -0.2 . These thermal emission sources were almost all found within the galaxy indicating a dominant thermal component. Further from these HII regions, the compact sources' spectral indices were steeper, between -0.7 and -1 , indicating that these are non-thermal synchrotron sources.

One important result from Heesen et al. (2011) is the linear relation between the radio and the $H\alpha$ brightness. This relationship means that we can use both as star formation tracers. Converting both of the emission types into star formation rates (SFR) they are able to compare the two measurements and they find that the radio SFR is 3 times lower than the $H\alpha$ SFR. This means that IC 10 lies beneath the radio-SFR correlation and is radio-dim. As mentioned above, Leroy et al. (2006) found that the inferred SFRs in IC 10 are too high for the molecular gas content. This may be explained through a biased in-time perspective where we are seeing IC 10 right after a peak in its starburst however, it is still not clear how much molecular gas is hidden and not traced by the CO emission in the dwarf and other dwarf galaxies. Heesen et al. (2011) therefore argue the importance of the development of an alternative SFR tracer in dwarf galaxies.

Westcott et al. (2017) presented high-resolution radio continuum maps of IC 10 at 1.5 GHz and 5 GHz using the e-MERLIN very-long baseline interferometer. They detected 26 sources in total, 11 compact sources at 1.5 GHz, 5 of which also had detections at 5 GHz. They identified 3 of the sources as HII regions, 5 as background galaxies, and 3 they could not identify. Of these 26 sources, they found 15 to be coincident with IC 10's main disk but none of these compact radio sources were found within the NTSB.

Heesen et al. (2018) studied IC 10 in the radio continuum using the Low-Frequency Array (LOFAR) at 140 MHz and with the VLA at 1580 MHz and 6200 MHz. They found that the continuum emission extends further along the minor axis of the galaxy

than expected for its inclination angle as well as a second more extended component away from the disk along the minor axis. This leads them to suggest that IC 10 has a radio halo.

3.4 Stellar Populations in IC 10

In two papers on the stellar content of IC 10, Sanna et al. (2009) and Sanna et al. (2010), investigated stellar populations with optical data from the Hubble space telescope (HST). They found a clear change in age distribution moving from the center of the field toward the external regions. They found a well-defined overdensity in their color-magnitude diagrams indicating the presence of intermediate-age red clump stars as well as old, red horizontal branch stars. In 2010, with new HST data and ground-based optical data from the Subaru Telescope and the Mega-Cam at the Canada-France-Hawaii Telescope, they confirmed the significant decrease of the young stellar populations when moving from the center toward the outer regions and found the tidal radius of IC 10 to be larger than previous estimates $r \approx 10'$. By taking the ratio of the observed star counts from the Mega-Cam data and the star counts predicted by galactic models they found a star count in excess by $\sim 3\sigma$ up to $42'$ from the center of the galaxy, supporting that the huge HI envelope surrounding IC 10 is associated with the galaxy.

Another study, Gerbrandt et al. (2015), done on the stellar populations in IC 10 revealed the spatial distribution of its resolved young, intermediate, and old stellar populations. They find that younger stellar populations in IC 10 are significantly offset from the geometric center of the older RGB population that traces an extended structure typical of blue compact dwarf galaxies (BCG) with an effective radius of $\sim 5.75'$. From this, they conclude that the young star formation takes place significantly away from the center of the galaxy and that IC 10 is much more extended in the optical than previously thought. When examining the outer regions of the older stellar population they find the outer isophotes of this galaxy are very regular in shape

and do not show any obvious signs of distortion, or any features that might suggest the presence of stellar streams or shells. They also do not find any evidence of stars located at a large radius exceeding the number that is expected from an extrapolation of the star counts toward the center of the population. Gerbrandt et al. (2015) concluded from their findings that there was no evidence of significant interaction with an unknown companion as suggested by the HI distribution. However, they do note that the current optical and near-infrared data on IC 10 does not cover the same area as the HI emission and further observations are necessary.

Somewhat contrary to the findings discovered by observing the stellar populations in IC 10, when studying the star clusters, Lim and Lee (2015) found some evidence of a past merger or tidal interaction of IC 10 with a companion galaxy. In this paper they derive photometry for 66 clusters and find star clusters in the halo are all older than 1 Gyr, while clusters found in the main body have ages from very young (several Myr) to old (≥ 1 Gyr). The young clusters are found to be mostly located in the H α emission to the southeast of the galactic center around the large HI cloud. Intermediate age clusters (~ 100 Myr) are found in two groups, One near the same large HI cloud and young stellar cluster and the other further away from the young cluster but still concentrated within the main disk and potentially associated with the HI spur in the NW. The old clusters are distributed in a wider area than the disk and show an asymmetrical structure elongated along the east and southwest directions potentially formed due to accretion. The concentration of the young and intermediate-mass cluster towards the center of the galaxy and the elongated distribution of the old metal-poor star clusters indicate that IC 10 may have an old halo embedding the disk of the main body. Two scenarios have been suggested to explain the formation of halos in dwarfs. The first is a merger between two gas-rich dwarf irregular galaxies similar and the second is early star formation activity with supernova feedback causing the large HI extensions. In section 3.1.2 we previously discussed that Ashley et al. (2014) found the velocity required for stellar feedback to

produce the southern plume is substantially larger than observed. However, this paper also suggests that there were potentially two starbursts due to the age distribution in the clusters. Suggesting that the youngest clusters show a peak at ~ 6 Myr corresponding to the most recent starburst, the intermediate aged clusters peak at ~ 100 Myr suggesting another starburst, and the oldest population at ~ 1 Gyr. This theory of a second, older starburst reduces the required velocity for stellar feedback to have created the southern plume to ~ 180 km/s which is much more reasonable than the previous findings.

A more specific stellar population worth discussing is the Wolf-Rayet (WR) stars found within IC 10. These are post-main sequence stars in their helium-burning stage that are dominated by strong winds and a high mass loss rate. Due to these winds, this stage in a star's evolution does not last very long and therefore a high concentration of WR stars in a galaxy indicates a period of a high SFR. These stars are also identifiable by their unique spectra, WN stars are observed with strong nitrogen lines in the stars spectra and WC stars are observed with strong carbon lines. The ratio of WC/WN stars in IC 10 stands at ~ 1.0 (Tehrani et al., 2017) which is an order of magnitude higher than other metal-poor dwarf galaxies in the Local Group such as the LMC and SMC. Possible origins for this high ratio are an unusual starburst has occurred or there are more hidden WN stars within the galaxy. Tehrani et al. (2017) did a new spectroscopic survey of IC 10 and found 11 WR candidates, 3 of which are new WN stars with 6 more being WC candidates, including all these stars it reduced the WC/WN ratio to ~ 0.7 . This is still more than twice that of the LMC and SMC. The author attributes this high ratio to the large star formation surface density of IC 10 relative to the LMC and SMC.

3.5 Literature Conclusions

IC 10 has been the subject of many multi-wavelength studies targeting the neutral ISM, the molecular ISM, stellar populations, the radio continuum emission, ionized

HII regions, and more. Yet questions still remain.

IC 10 has a turbulent and complex HI disk filled with holes and shells created by stellar winds and supernova explosions. The extent of the violent feedback is a result of IC 10's high star formation intensity. The inner disk of the galaxy has not been as extensively studied as the large HI extensions due to the resolutions required. The previously highest resolution survey, LITTLE THINGS (Ashley et al., 2014) with a spatial resolution of $\sim 6''$ or ~ 30 pc and a velocity resolution of ~ 2.6 km s $^{-1}$ shows twenty high-quality holes in the disk, thirteen more than previously seen by Wilcots and Miller (1998). Individual star-forming clouds appear on scales of ~ 20 pc, leaving the obvious question: what are IC 10's true morphological and kinematic features only visible with higher resolution data? We do not yet know how many holes or star-forming clouds appear in the disk of IC 10. Further, the kinematic components of the clouds have not yet been studied in depth. Within the star-forming clouds, we do not yet know how a low metallicity environment affects star formation and molecular abundances.

The same mechanism that triggered the starburst in IC 10 may also have ties to the creation of the large HI extensions visible around the disk. These extensions have been extensively studied with a single dish and compact array observations sensitive to the low column density gas. As a result, there are now only two main theories to the origins of these large-scale HI structures. Either IC 10 is the result of a merger or interaction or IC 10 is still forming and accreting primordial intergalactic gas. The true origins have yet to be discovered, however, with new stellar population studies we may be able to answer the question of how BCD galaxies trigger their starbursts.

Answering the outstanding questions left for IC 10 could have fundamental impacts on our understanding of galaxy evolution and star formation in the early universe. The galaxy remains the best-known candidate to answer questions on the characteristics of low metallicity, less massive galaxies.

Chapter 4

Data Presentation and Analysis

4.1 L-band Observations

The L-band observations for IC 10 consist of both 1 - 2 GHz continuum observations and 21-cm spectral line observations of the atomic hydrogen. These allow us to observe both atomic gas clouds as well as continuum free-free and synchrotron emission. We observe IC 10 in all 4 VLA configurations; A, B, C, and D for ~ 1820 hours in order to achieve the required sensitivity and resolution for our science goals. The C and D configuration observations consist of a 7-point hexagonally packed mosaic which covers the bright HI emission in the disk of the galaxy as well as the extended HI envelope that surrounds the galaxy. The A and B observations only consist of a single central field pointing which covers all of the brightest HI at the center of IC 10.

The two main science drivers for the survey are the 21-cm spectral line and the 1-2 GHz continuum which require the following sensitivity and time requirements. In order to resolve the line-integrated HI emission associated with individual clouds and resolve holes in the atomic gas we require ~ 20 pc resolution and 1σ column sensitivity of $1.0 \times 10^{20} \text{ cm}^{-2}$ per 7 km/s channel. To analyze detailed kinematics in the atomic gas we again require 0.4 km/s spectral resolution with a $\sim 15''$ spatial resolution or ~ 60 pc at the ~ 790 kpc distance to IC 10. To detect large scale HI structures we target a $\sim 3 \times 10^{18} \text{ cm}^{-2}$ over a 20 km/s line width. Finally, for detecting and

resolving SNRs and HII regions in the 1 - 2 GHz continuum emission we require point source sensitivity of 2 - 3 μJy and a spatial resolution of $\sim 2''$ or $\sim 5 - 10$ pc at the distance to IC 10.

The above requirements lead to ~ 22 hours split between A and B configurations or ~ 11 hour effective integration time on source each, ~ 11 hours on source per pointing in C configuration, and ~ 5.5 hours on source per pointing in D configuration. All-in this combines to ~ 137.5 hours on source for IC 10. We have new continuum data with a resolution of $1.4''$ and a $4.5 \mu\text{Jy}/\text{beam}$ continuum RMS as well as HI spectral line data with a spatial resolution of $4.5''$, a spectral resolution of 0.4 km/s and an RMS of $\sim 7.0 \times 10^{20} \text{ cm}^{-2}$.

4.2 Radio Continuum

4.2.1 Radio Continuum Data and Calibration

For our continuum imaging, we used data from three out of the four VLA configurations, the largest separation and highest angular resolution A configuration with a maximum baseline length of 36.4 km and angular resolution in the L-band of $1.3''$. The B configuration with a baseline length of 11.1 km and a resolution of $4.3''$ and finally the C configuration with a baseline length of 3.4 km and a resolution of $14''$ in the L-band. For this imaging, we don't include our D configuration data as this is lower resolution ($\sim 46''$) and we are targeting the compact HII regions and supernova remnants within IC 10. We included data from all of our A and B configuration measurement sets and only included the C configuration data over the central field of the 7-point hexagon as the continuum emission is concentrated in a small region towards IC 10's HI disk.

All of our data has gone through the VLA pipeline as well as a manual QA process that flagged RFI within the observations. During our observations, we observed two known flux density calibrator sources, 3C138 for polarization angle calibrations and

3C48 for the bandpass and amplitude calibrator. Within the QA process, we use calibrator amplitude and phase vs. frequency plots, amplitude vs. phase plots, time axis plots, and more to identify RFI within specific spectral windows, at specific times or as a result of issues in certain baselines or antennas (Koch et al., in prep.).

Following the quality assurance of our data and a final run of the VLA calibration pipeline, we run a single round of phase-only self-calibration (“selfcal”) on our data set. During this selfcal run, we use solution intervals for each configuration and we calibrate each polarization separately without combining them. After selfcal, we found an improvement in the dynamic range of images by a factor of $\sim 1.5\times$ around the bright sources in the field.

4.2.2 Continuum Imaging

For our imaging parameters, we used the MTMFS deconvolution algorithm in CASA (CASA Team et al., 2022) for its wide-band and wide-field advantages, as we are imaging over the entire 1.0 GHz wide L-band and over an area of $\sim 0.5^\circ$. We used a pixel size of $0.26''$ in order to have 5 pixels across the synthesized beam and an image size of 8000 pixels attempting to include as many bright nearby sources as possible while reducing the effects from a bright out-of-field source. We chose Briggs weighting with a robust value of 0 allowing for a balanced weighting between natural and uniform and with a default value of the small scale bias we include scales at 0, 6, 10, 30, 60, 120 and 240 pixels this sets the scales on which to clean and includes the larger scale emission by folding in 120 and 240 pixel scales. Finally, we used the *w*-project gridding algorithm to correct for the wide-field, non-coplanar baseline effect.

The final L-band image from 1.0 - 2.0 GHz can be seen in figure 4.1 with HI contours at levels of 250 and 1000 K km/s. The image has a spatial resolution of $\sim 1.5''$ and an RMS noise of $4.5 \mu\text{Jy}/\text{beam}$. Within the image visible is IC 10’s large non-thermal superbubble as well as a few bright continuum sources concentrated along the HI shells and within the large HI cloud. Also visible are two bright background radio

galaxies to the East (left) and southwest (bottom right) of the center of the galaxy. Further, we can see many more bright point sources around IC 10 which are mostly bright background galaxies.

4.2.3 Spectral Index Tests

CASA Spectral index

The goal of this research was to identify optimal imaging strategies for the LGLBS continuum data. We thus conducted several trials of imaging strategies before validating and comparing the results of each. Our primary objectives for the IC 10 continuum data in this thesis were to first verify our imaging parameters and second to create a compact continuum source catalog with source positions, fluxes, and source classifications. To accomplish both these goals we will detect sources in our different images and calculate the spectral index, a measure of how the source flux varies with frequency. The spectral index is given implicitly by

$$S_\nu = S_0 \left(\frac{\nu}{\nu_0} \right)^\alpha, \quad (4.1)$$

where rearranging gives

$$\alpha = \frac{\log(S_\nu/S_0)}{\log(\nu/\nu_0)}. \quad (4.2)$$

Typical values for the radio spectral index are between -2 and $+1$ so if we find any sources with a steeper spectral index than this we assume it is an issue in our imaging. Through literature, common spectral index lines have been used to classify sources into thermal HII regions or non-thermal supernova remnants, and in this thesis we use the following:

1. ($\alpha > -0.2$) - HII-region
2. ($-0.2 > \alpha > -0.8$) - Supernova Remnant
3. ($-0.8 > \alpha$) - Background galaxy

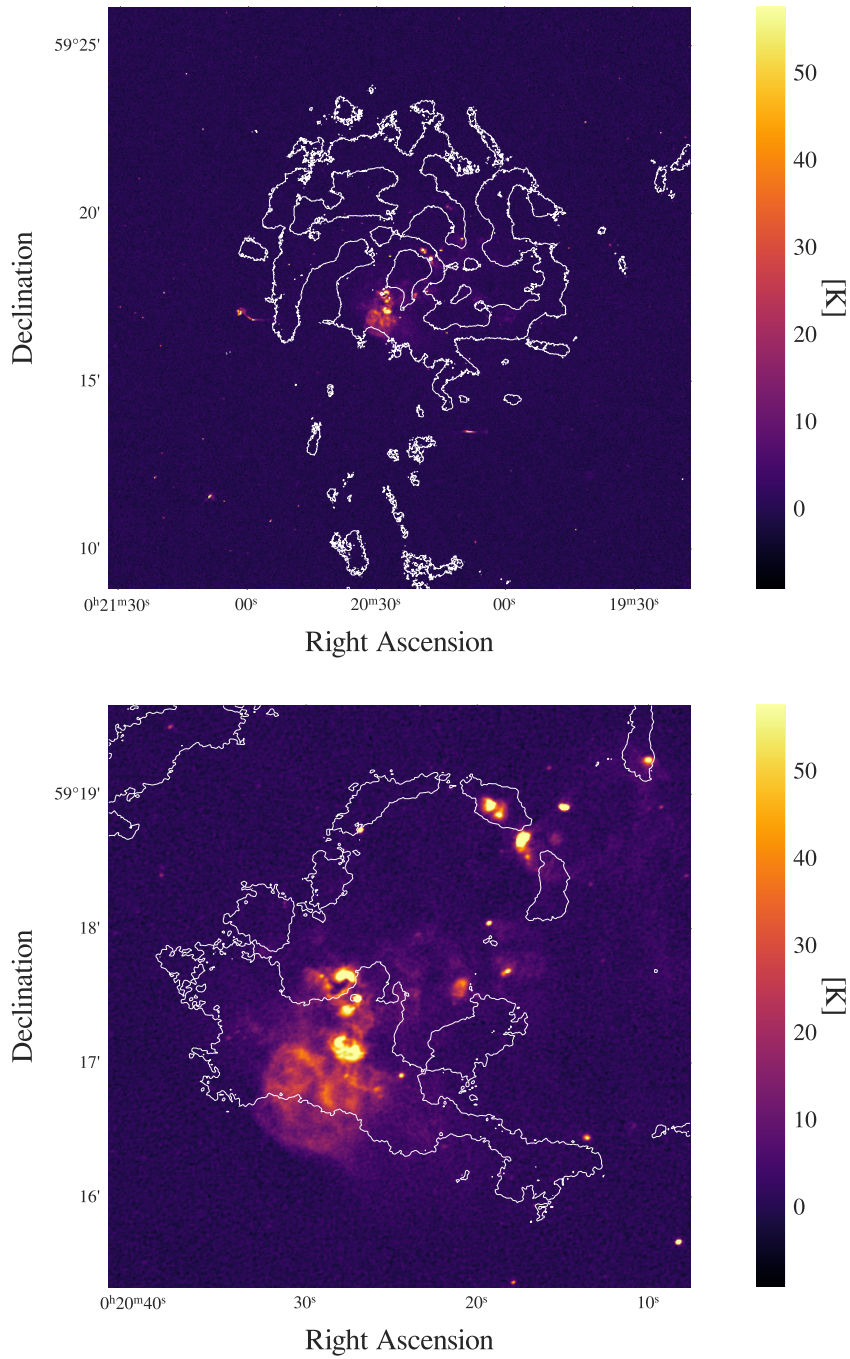


Figure 4.1: L-band 1.0 - 2.0 GHz Continuum data. The top panel shows a large field of view covering $\sim 0.5^\circ$. The bottom panel shows the same data over a smaller region containing the majority of the continuum emission in IC 10 over $\sim 0.125^\circ$ or $7.5'$. Overlaid are contours from the HI moment 0 integrated intensity map at 250 [K km/s] and 1000 [K km/s] for the top and bottom panels respectively.

We attempt two imaging strategies using both W-project and AW-project and three methods to calculate the spectral index; using the CASA output `.alpha` spectral index map, by taking the slope of a log scale flux vs. frequency plot and by finding a two-point spectral index between the L-band 1.5 GHz image and 6.0 GHz C-band data. This C-band data is from VLA project 15A-062 (PI: Dávid Cseh) and can be seen in the bottom panel of figure 4.7. It was prepared using the standard VLA reduction pipeline with no changes. This data has a resolution of $\sim 1''$ compared to the $\sim 1.5''$ resolution of the L-band data and will therefore be convolved to the resolution of the L-band 1.5 GHz image for comparison. The data and the approach to calculating the L-to-C spectral index will be discussed further in section 4.2.3.

The first test was to confirm the spectral index output from the CASA imaging software was trustworthy. To do this we imaged the L-band into five smaller sub-bands. Four 0.1 GHz wide bands; 1.6 - 1.7 GHz, 1.7 - 1.8 GHz, 1.8 - 1.9 GHz, 1.9 - 2.0 GHz, and one 0.4 GHz wide image from 1.6 GHz to 2.0 GHz to compare with. Using PyBDSF (Mohan and Rafferty, 2015) to detect sources in the images, we were able to get a catalog of all the sources in each of the 0.1 GHz images and the 1.6-2.0 GHz image. Next, we matched these catalogs by coordinates keeping only the sources that are visible in each sub-band. Finally, we found the spectral indices for each source in two ways. In the first method, we used the CASA spectral index output `.alpha` image from the 1.6 - 2.0 GHz sub-band and took the average value of the spectral index for each source. For the second method, we found the total flux from each source in each of the four 0.1 GHz images. We then created a log scale flux vs. frequency plot and took the slope of the line to find the spectral index of the source, following equation 4.2.

Finally, we plotted the spectral index found in each method against each other. This can be seen in figure 4.3. While there are a few outlier points, the spectral indices from both methods generally agree. The outlier points, specifically in the slope spectral index are due to issues in the 0.1 GHz sub-band images. The 1.9 - 2.0 GHz

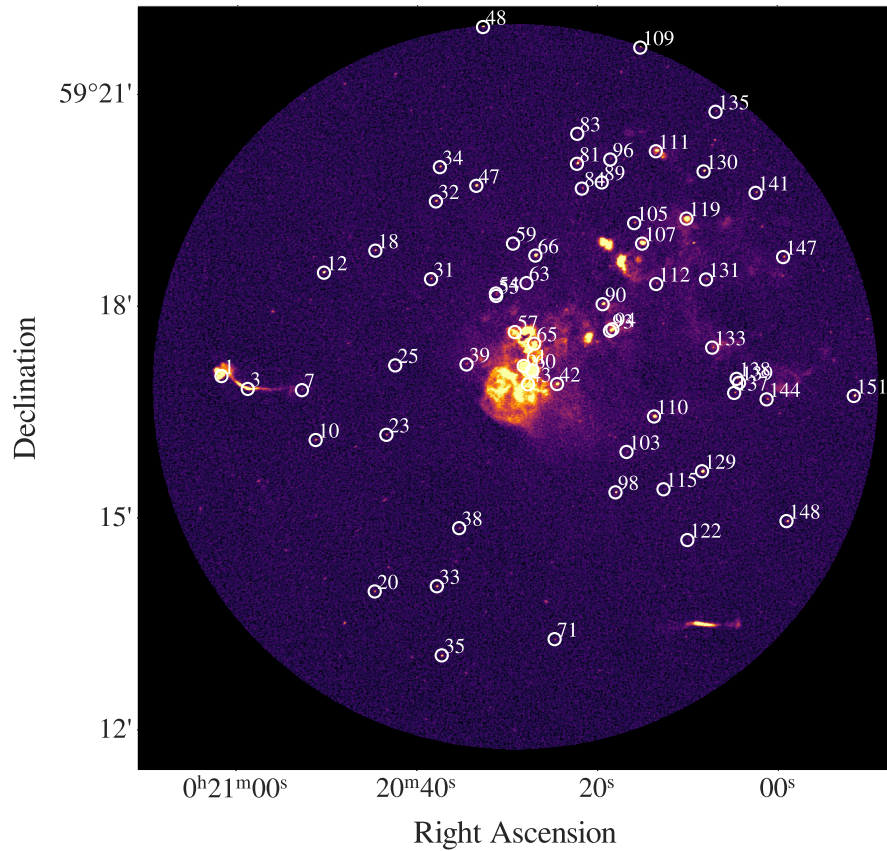


Figure 4.2: L-band 1.0 - 2.0 GHz continuum image with final catalog source locations overplotted. These are compact continuum ($< 3''$) sources that are likely HII regions, supernova remnants, and background galaxies. Labels are Source ID numbers from the source detection algorithm pyBDSF.

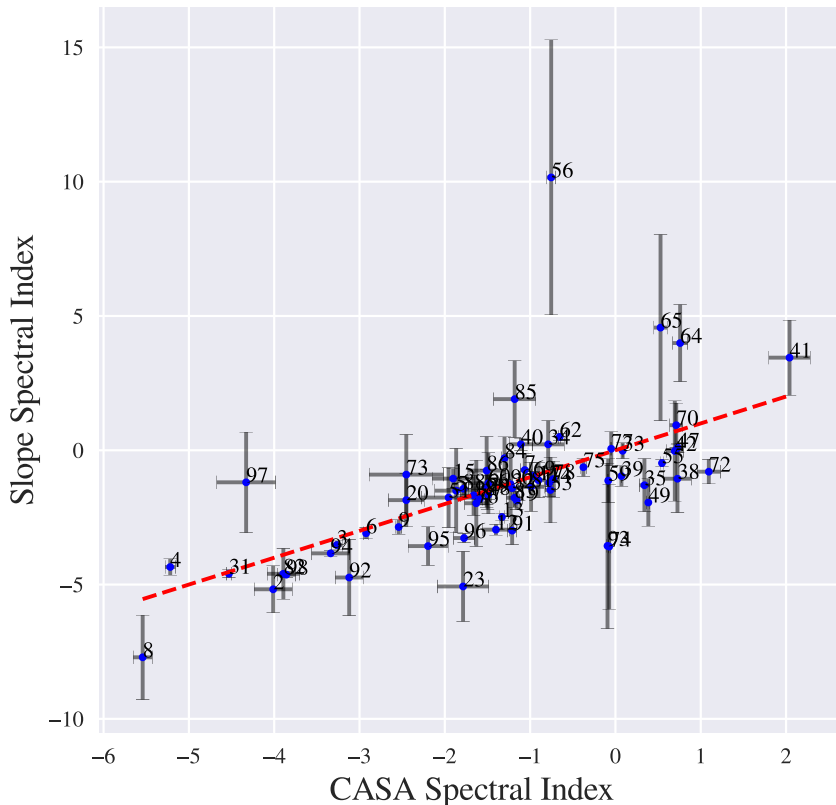


Figure 4.3: L-band slope Spectral Index vs. CASA Spectral Index. The figure shows the spectral index of sources over the 1.6 - 2.0 GHz frequency range calculated through two methods. On the horizontal axis is the spectral index found via the CASA `.alpha` output spectral index map. The vertical axis shows the spectral index calculated through the slope of the $\log(\text{Flux})$ vs. $\log(\text{Frequency})$ plot for each source across four 0.1 GHz wide sub-band images at 1.6 - 1.7 GHz, 1.7 - 1.8 GHz, 1.8 - 1.9 GHz, and at 1.9 - 2.0 GHz. The dashed line indicates the locus of equality.

image had radio frequency interference that caused issues in the flux measurements of some sources.

The sources detected in the above test were detected over the full range of the L-band image which is $\sim 0.5^\circ$ across and thus over quite a large area. Both spectral indices generally have ranges between -5 and $+2$ ignoring some outliers. This is a fairly large range and usually, we expect to find radio spectral indices between -2 and $+1$ with anything steeper than ~ -2 being due to an issue in the imaging process. To verify these spectral indices, we plotted the spectral index as a function of the

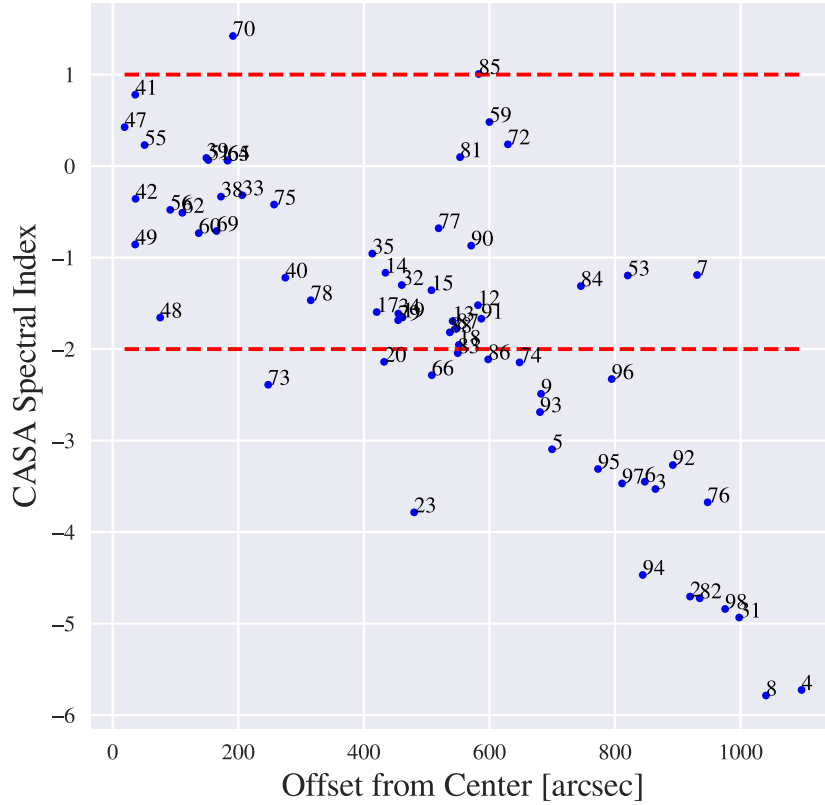


Figure 4.4: CASA Spectral Index vs. Offset from the center of the image [arcsec]. The vertical axis is the spectral index calculated from the CASA output `.alpha` image from a 1.6 - 2.0 GHz image. The horizontal axis is the offset of each source from the center of the field in arcseconds. The blue points are labeled with their source IDs from the detection algorithm in `pyBDSF`. The dashed red lines represent the typical range for radio spectral indices between +1 and -2.

offset from the center of the image. This can be seen in figure 4.4. Immediately visible is a trend that further from the center of the image we have steeper more negative spectral indices. The primary beam size at a specific frequency is defined as $\theta_{\text{PB}} = 42' / \nu_{\text{GHz}}$, therefore at a central frequency of 1.8 GHz, this image has a full width at half power θ_{PB} of $\sim 1400''$. At the lowest frequency in the sub-band images of 1.6 GHz $\theta_{\text{PB}} = 1575''$ and at the highest frequency of 2.0 GHz $\theta_{\text{PB}} = 1260''$ meaning the entire area is within the primary beam across the 0.4 GHz wide frequency band of the image.

W-project vs. AW-project

Attempting to find a solution to the steep spectral indices at high offsets, we experimented with the AW-project algorithm. This algorithm attempts to solve the Antenna A-term at each W-projection plane as a wide bandwidth implies the primary beam changes significantly in-band as a function of frequency (CASA Team et al., 2022).

Unfortunately, AW-project is a computationally expensive algorithm and therefore we could only image one B-configuration data set. For our comparison, we imaged the same data set using both W-project and AW-project with minimal cleaning and the same imaging parameters. We then once again used `pyBDSF` to detect sources in each image and matched the catalogs by their positions. Due to the different imaging parameters and different catalog matching, this W-project and AW-project catalog do not necessarily contain the same sources or the same source IDs as the previous catalog. Finally, we found the spectral index of each source from the CASA output spectral index image and compare each with each other and against the offset from the center of the image as seen in figure 4.5 and figure 4.6.

AW-project clearly produces much better results at high offset with every source having a spectral index between ~ 2 and ~ -2 . Unfortunately due to its computational cost, it is not feasible to image our full data set with the standard gridding algorithm at this time, however, CASA is developing a GPU-based gridding algorithm which should reduce the computational time required.

In-band Spectral Index vs. L-to-C band Spectral Index

For the final spectral index value to be used in the continuum source catalog, we used both L-band and VLA C-band data at 4.0 - 8.0 GHz. Both the L-band and C-band data can be seen in figure 4.7. We use only data from the center of the field so as to not have sources with steep α . This figure shows the L-band image over the same region we have C-band data. In the bottom panel of this figure, the C-band VLA

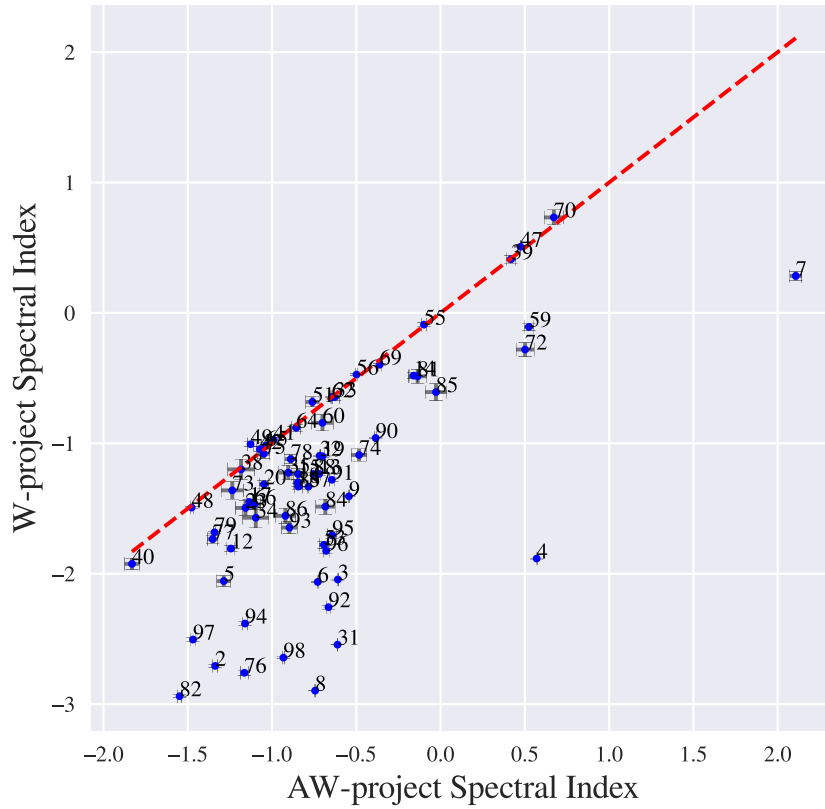


Figure 4.5: W-project Spectral Index vs. AW-project Spectral Index. The vertical axis shows the spectral index using the W-project gridding algorithm which only takes the sky curvature effect into account. The horizontal axis shows the spectral index from the AW-project gridding algorithm which also takes into account the antenna beam size changing with frequency. The red line represents the line of equality and each point is labeled with its source ID from pyBDSF.

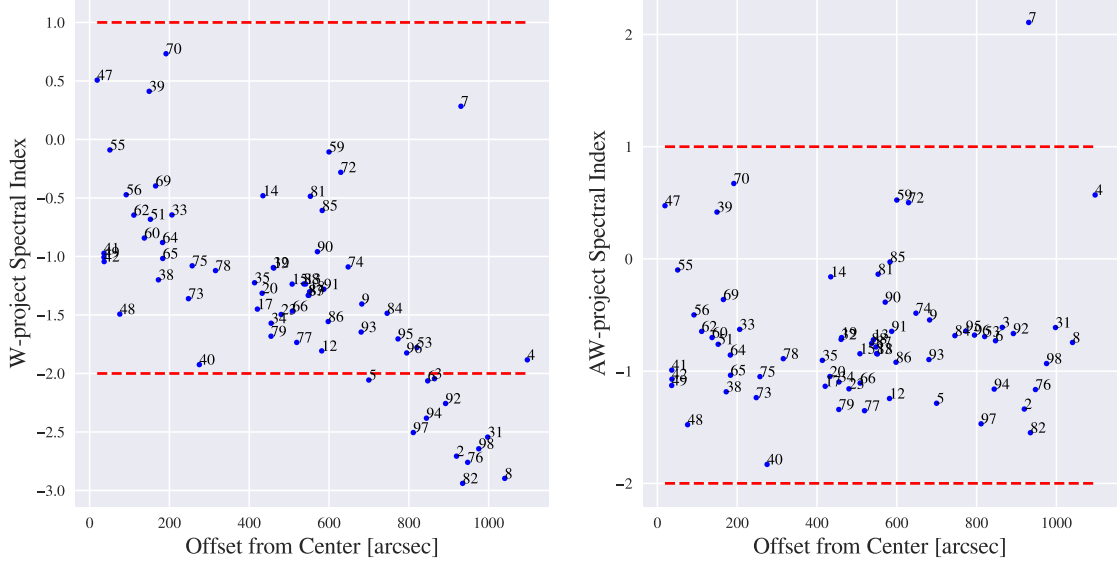


Figure 4.6: W-project & AW-project spectral index vs. Offset from image center [arcsec]. The left panel shows the W-project gridding algorithm spectral index vs. the offset from the center of the image in arcseconds. The right panel shows the AW-project gridded spectral index vs. the offset from the center in arcseconds. The red lines show the typical range for radio spectral indices between +1 and -2. Note: The vertical axis in each panel does not share a common scale.

data is visible and in the image, a few bright radio sources can be seen but limited extended emission. Also visible, are artifacts in the image left over from the imaging process and negatives around the bright sources. These artifacts are potentially due to missing short spacing information or the data requires further calibration. This approach to calculating the spectral index should give a better result as it has a much wider (4.5 GHz) spectral interval than the in-band L-band spectral index (0.4 GHz). First, we once again use `pyBDSF` to detect the sources in both the L-band and C-band images before matching the catalogs with each other. This is a distinct catalog from the previous two tests and while many sources may overlap between catalogs due to not all sources being visible in the C-band the final catalog does not include all sources visible in the L-band. This catalog is also over a smaller region than the previous two tests leading to fewer total sources detected and different source IDs.

Using equation 4.2 and applying it to our L-band and C-band flux and frequencies,

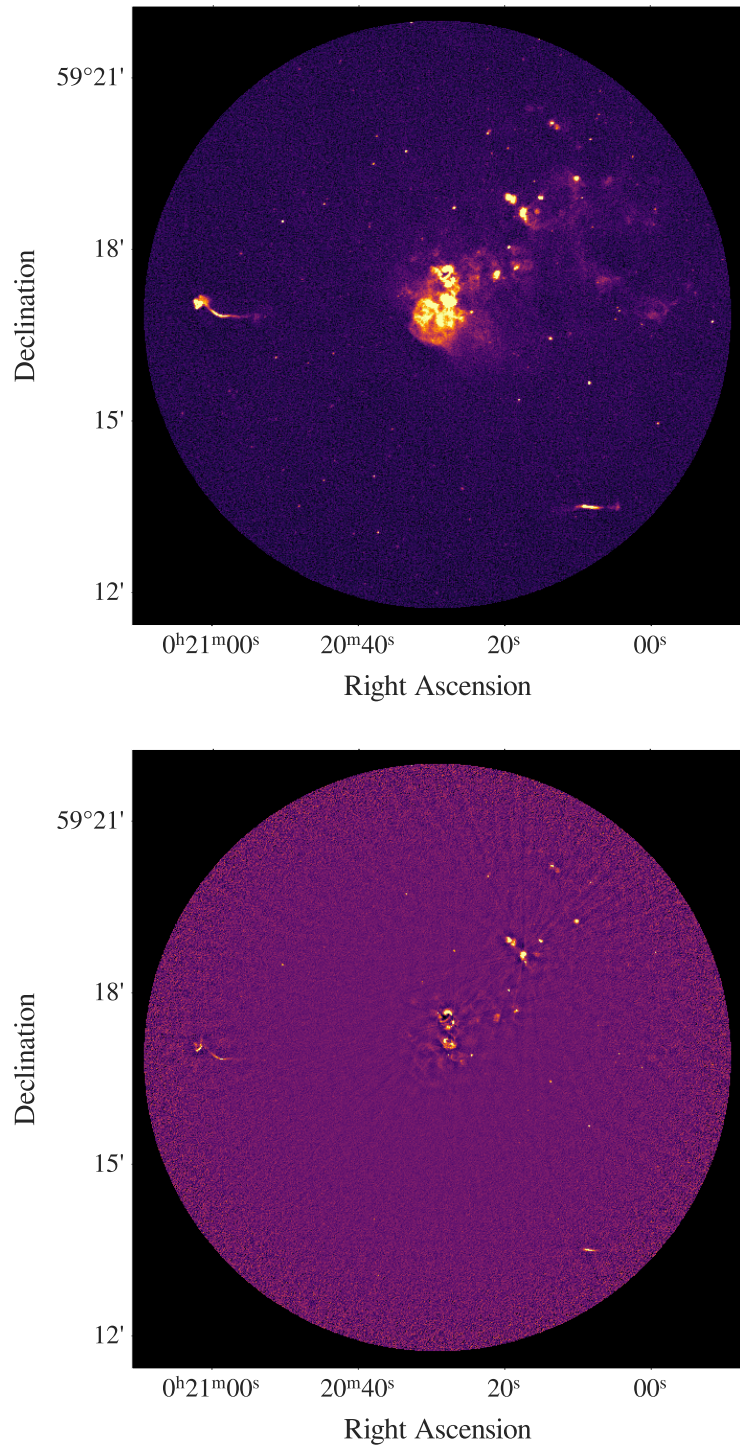


Figure 4.7: L-band 1.0 - 2.0 GHz and C-band 4.0 - 8.0 GHz data. The upper panel shows the LGLBS L-band continuum data with a $\sim 1.5''$ spatial resolution. This is the same data as shown in figure 4.1 now only over a smaller central region where we also have C-band data. The C-band data is from VLA project 15A-062 (PI: Dávid Cseh) and can be seen in the lower panel with a spatial resolution of $\sim 1''$.

the two-point spectral index is defined by

$$\alpha = \frac{\log(S_C/S_L)}{\log(\nu_C/\nu_L)}. \quad (4.3)$$

This allows us to calculate the spectral index over a larger frequency range, from the 1.5 GHz central frequency in the L-band to the 6 GHz central frequency in the C-band. We then compared this L-to-C spectral index with the In-band α from the L-band image, the results of which can be seen in the L-band to C-band Spectral Index vs. Spectral Index plot in figure 4.8. We can see that the L-to-C spectral indices have a maximum value of ~ -0.25 and a minimum value of ~ -2.5 while the L-band spectral indices have a maximum value of ~ 0.5 and a minimum value of ~ -3.0 .

4.2.4 Continuum Source Catalog

The first 10 rows of the continuum source catalog can be seen in 4.1 with the full catalog available in the appendix A.1. Figure 4.2 shows the L-band data with each source circled and labeled. The final catalog was taken from the L-to-C source detection and we used the L-to-C spectral index results. We find 62 total sources, the brightest source with a total flux of 7 mJy and the dimmest detected source having a flux of 0.047 mJy. Using the spectral index values as well as the source offset from the center we categorized each source into either an HII region ($\alpha \geq -0.2$), a supernova remnant ($-0.8 \leq \alpha \leq -0.2$) or a background galaxy ($\alpha \leq -0.8$). As both SNR and background galaxies have steep radio spectral indices and there is some overlap, we help distinguish between SNR and background galaxies by using the offset from the center of the field. Sources with a high offset ($\geq \sim 250''$) definitively outside of IC 10's continuum galaxy and HI disk are likely to be background galaxies.

Taking the L-to-C Spectral Index, we find 0 HII regions, 19 SNR, and 43 background galaxies. Comparing this with the generally flatter L-band in-band spectral index we find 7 HII regions, 16 SNR, and 39 background galaxies. While calculat-

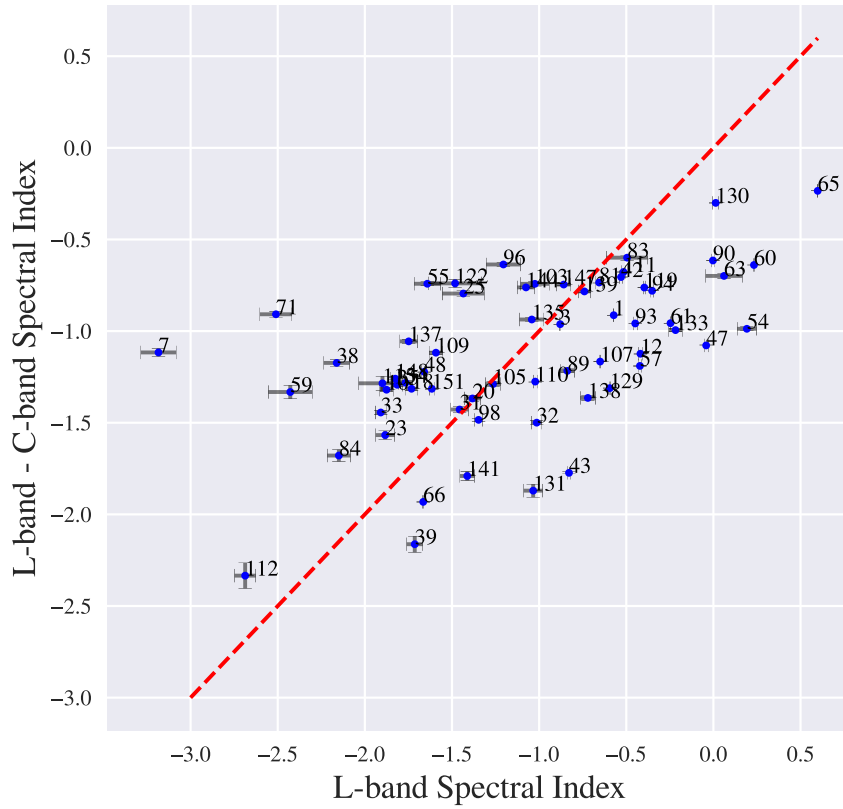


Figure 4.8: L-band Spectral Index vs. L-band to C-band Spectral Index. The horizontal axis shows the in-band L-band spectral index values over the 1.0 - 2.0 GHz frequency range. These were calculated from the CASA output `.alpha` image. The vertical axis shows the L-band to C-band two-point spectral index calculated from equation 4.3 over the 1.5 - 6.0 GHz frequency range. The red line indicates the line of equality.

| ID | Offset [arcsec] | RA [°] | DEC [°] | L-band Flux [μ Jy] | C-band Flux [μ Jy] | L-band α | L-to-C α | Class | L-band Class |
|----|--------------------|-----------|------------|----------------------------|----------------------------|--------------------|--------------------|-------|--------------|
| 1 | 286.2 | 5.26 | 59.28 | 5104.5 \pm 114.2 | 1335.5 \pm 22.1 | -0.57 \pm -0.001 | -0.91 \pm 0.0002 | SNR | BKG |
| 3 | 265.3 | 5.24 | 59.28 | 1274.8 \pm 83.9 | 458.6 \pm 22.1 | -0.88 \pm -0.004 | -0.96 \pm 0.0008 | BKG | BKG |
| 7 | 220.1 | 5.22 | 59.28 | 102.5 \pm 17.9 | 29.5 \pm 8.1 | -3.18 \pm -0.101 | -1.12 \pm 0.0209 | BKG | BKG |
| 10 | 220.9 | 5.21 | 59.27 | 227.3 \pm 19.5 | 37.7 \pm 8.1 | -1.88 \pm -0.038 | -1.32 \pm 0.0113 | BKG | BKG |
| 12 | 206.2 | 5.21 | 59.31 | 802.7 \pm 20.3 | 168.9 \pm 5.8 | -0.42 \pm -0.01 | -1.12 \pm 0.0024 | SNR | BKG |
| 20 | 262.2 | 5.19 | 59.23 | 187.3 \pm 17.9 | 34.1 \pm 10.5 | -1.38 \pm -0.046 | -1.37 \pm 0.0151 | BKG | BKG |
| 18 | 172.4 | 5.19 | 59.31 | 265.1 \pm 15.5 | 42.9 \pm 5.2 | -1.73 \pm -0.032 | -1.31 \pm 0.0095 | BKG | BKG |
| 23 | 164.6 | 5.18 | 59.27 | 179.1 \pm 21.7 | 20.7 \pm 5.5 | -1.88 \pm -0.054 | -1.57 \pm 0.0226 | BKG | BKG |
| 25 | 138.4 | 5.18 | 59.29 | 70.2 \pm 15.4 | 24.3 \pm 6.7 | -1.43 \pm -0.12 | -0.79 \pm 0.0182 | BKG | SNR |
| 31 | 119.3 | 5.16 | 59.31 | 169.5 \pm 17.6 | 14.5 \pm 4.9 | -1.46 \pm -0.05 | -1.43 \pm 0.0177 | BKG | BKG |

Table 4.1: IC 10 continuum source catalog. This table shows the first 10 rows of the continuum source catalog with the full catalog available in the appendix A.1. Offset is the source offset from the field center in arcseconds, L-band α is the L-band In-band spectral index value calculated from the CASA `.alpha` image, L-to-C α is the 2 point spectral index calculated between the L-band 1.5 GHz data and the C-band 6.0 GHz data.

ing the spectral index over a larger frequency range should recover a more accurate spectral index it is worth noting the artifacts and negatives in the C-band data are affecting our L-to-C spectral indices leading to steeper values. A future analysis with improved C-band data would likely improve these results.

4.3 Spectral Lines

Spectral line data is contained in a so-called ‘‘Spectral Cube,’’ this is a 3D cube of data with two spatial dimensions and a third velocity or spectral dimension. We can split these cubes into one 2D map for each velocity channel called ‘‘channel maps’’ to see all the emission at those velocities or we can integrate the cube along different axes.

By collapsing the cube into a 2D map we get ‘‘Moment maps.’’ There are four moment maps used in this thesis, the first is the Moment 0 integrated intensity map

created by integrating the spectra over the frequency range,

$$M_0 = \int I_\nu d\nu, \quad (4.4)$$

where ν is the frequency, however, we can also integrate over the spectral axis in velocity units. The Moment 1 map is the intensity-weighted velocity of the spectral line and is given by

$$M_1 = \frac{\int \nu I_\nu d\nu}{\int I_\nu d\nu} = \frac{\int \nu I_\nu d\nu}{M_0}, \quad (4.5)$$

and the Moment 2 map is the variance around the centroid defined by

$$M_2 = \frac{\int I_\nu (\nu - M_1)^2 d\nu}{M_0}. \quad (4.6)$$

The moment 2 map can be used as an estimator of line width in units of the spectral axis squared, from which we can get linewidth maps in units of the spectral axis [km/s] through

$$\sigma = \sqrt{M_2}, \quad (4.7)$$

and through

$$\text{FWHM} = \sigma \sqrt{8 \ln 2}. \quad (4.8)$$

Here, σ is the width of a Gaussian and the FWHM is a full-width half-maximum linewidth map along the same spectral axis. Two more 2D maps we can get are the Peak intensity and the velocity of peak intensity respectively. We can also collapse the 3D map into a 1-dimensional spectrum where we collapse both position axes within an aperture or per pixel and return the spectrum of the line in that area. This can be used to look at the composition/chemistry of an observation or to look at the kinematic components of the gas.

4.3.1 Neutral Hydrogen

To showcase our data, we create moment maps from our high-resolution HI cube. Before collapsing the cube into the 2D maps, we first mask the cube at a 3σ level

using the `signal-id cprops-mask` tool from the PHANGS Imaging Pipeline (Leroy et al., 2021). Figure 4.9 shows the HI 21-cm spectral line data. This figure shows the Moment 0 integrated intensity map in units of [K km/s], the top right panel shows the Moment 1 central velocity map in [km/s], the bottom left panel shows the line width FWHM [km/s] and the bottom right plot shows the peak brightness temperature in [K]. This spectral cube has a spatial resolution of $\sim 4.5''$ and a spectral resolution of ~ 0.4 km/s and an RMS noise of 3.7×10^2 K km/s.

The integrated intensity map shows us that, unsurprisingly, the HI is concentrated within the disk of the galaxy. The brightest HI can be seen within the large cloud towards the bottom of the disk. This large cloud contains the vast majority of the continuum and optical emission within the galaxy. The rest of the brightest HI is concentrated on the shell structures surrounding the holes in the HI. The HI holes immediately visible in the integrated intensity map typically have no HI emission throughout the entirety of the region. However, there are also some smaller holes within the disk that contain HI emission on either the near or far side but not both and are not immediately evident in the moment 0 map discussed in Ashley et al. (2014).

Central velocities range from -320 km/s to -360 km/s where the disk appears to be rotating such that the eastern edge approaches us and the western side of the disk is receding. The extensions are only slightly visible in our data due to the high resolution which resolves our large-scale diffuse gas. Regardless, it is evident the extensions and spurs around the disk are counter-rotating, starting with the northwest spur in the top right of the Moment 1 map we can see it has a typical velocity of -320 km/s while the western edge of the disk has a typical velocity of -370 km/s, ~ 50 km/s difference. The NE spur is not fully visible in our map, however, it is possible to see the region has gas approaching us compared with the disk. Within, the southern plume we can see starting at the southern tip a central velocity of ~ -330 km/s decreasing to ~ -360 km/s where the plume approaches the eastern side of the disk.

Visible in the FWHM map, we can see regions of higher line width, these regions are generally concentrated in regions with increased HI emission, such as the large HI cloud at the south of the disk. Notably, we also see regions of higher dispersion in regions with lower column density HI towards the edge of the disk. These regions seem to be where the spurs and plumes around the disk meet the gas within the disk.

4.3.2 CO Lines

Along with the HI 21-cm spectral line data we use to trace the atomic gas, we also use CO (1-0) emission line data to trace the molecular gas in IC 10. Figure 4.10 shows the CO 1-0 emission from the CARMA interferometer feathered with IRAM 30m single dish data, This data set was collected by our collaborator Dr. Adam Leroy and will be published in forthcoming work from the LGLBS collaboration. The CO (1-0) data has a spatial resolution of $\sim 8.5''$, a spectral resolution of ~ 2.5 km/s, and an RMS noise of ~ 1.3 K km/s. This figure shows the CO integrated intensity map with the HI integrated intensity contours overlaid at 800, 1500, and 2500 K km/s. Evident in the image is the CO emission concentrated in regions where we also see bright HI gas. The majority and brightest CO emission is once again found within the large HI cloud in the southern region of IC 10's disk. However, we can also see some bright CO towards the north of the disk and along the HI shells.

To both the east and west of the disk, we can see relatively large and bright CO clouds, the western side has clouds far from the center of the disk, however, the clouds at the center are concentrated along HI shells on the far side of many HI holes. On the eastern side of the galaxy far from the disk and away from the holes and shells we see one lone, large CO cloud. This off-disk cloud is isolated from other CO emission and stellar populations and will be investigated further in section 4.7.

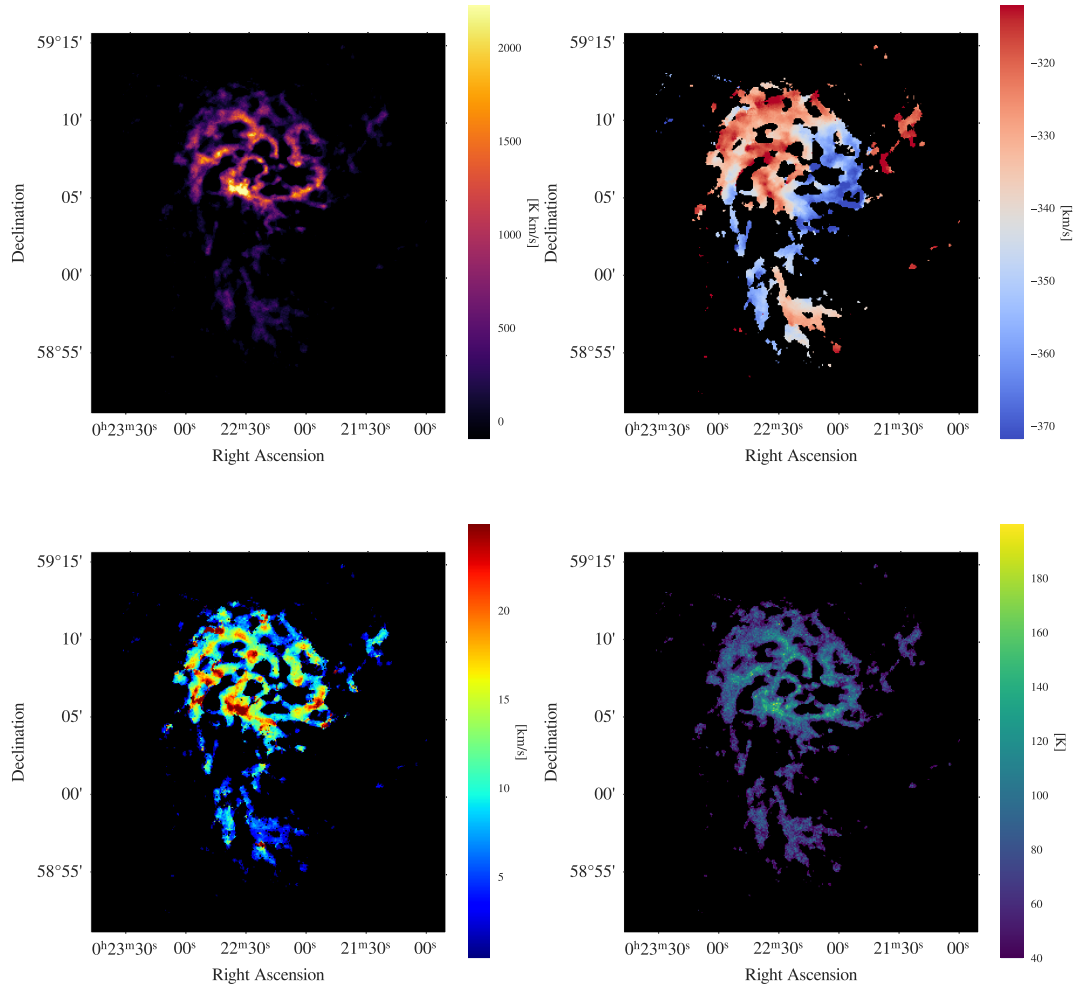


Figure 4.9: IC 10 HI Moment Maps. The upper left panel shows the Moment 0 Integrated Intensity plot [K km/s], and the upper right panel shows the Moment 1 Intensity weighted velocity map [km/s]. In the bottom left panel, we have the line width FWHM map [km/s] and in the bottom right panel the peak temperature [K] map can be seen.

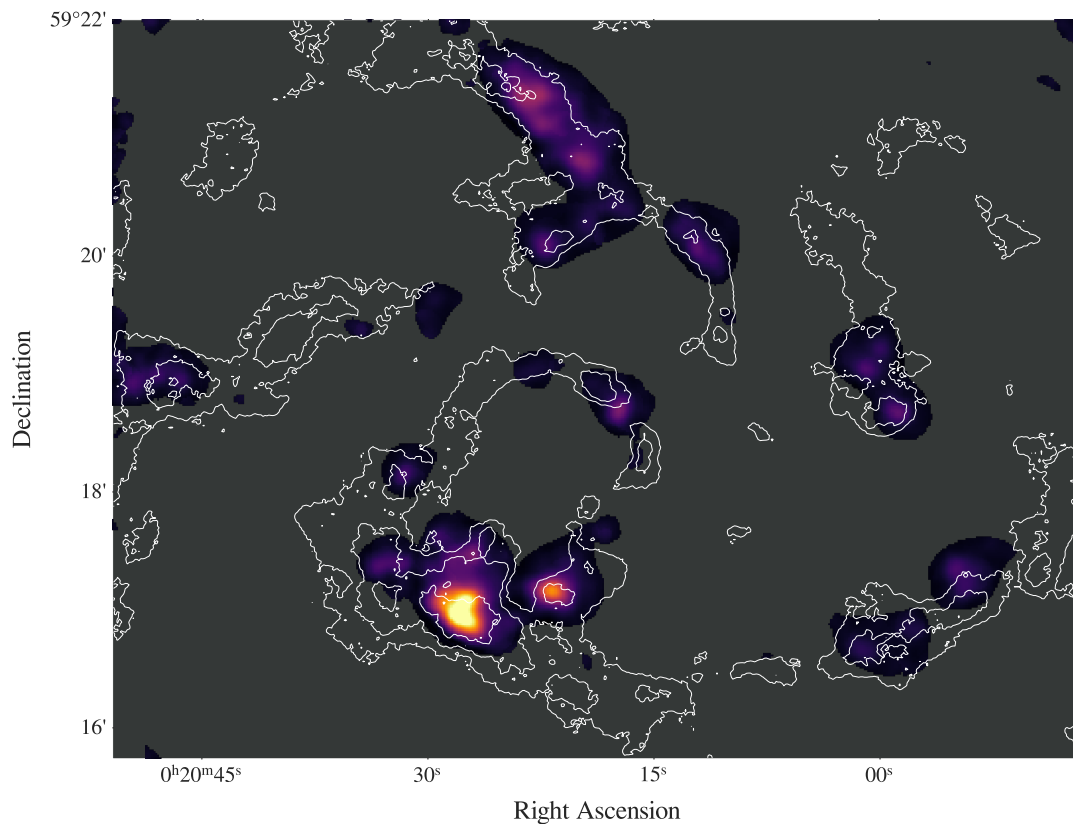


Figure 4.10: IC 10 CO (1-0) molecular gas moment 0 integrated intensity map [K km/s] with HI atomic hydrogen moment 0 integrated intensity contours overlaid in white. The HI contours are at levels 800, 1500, and 2500 K km/s.

4.4 Multi-wavelength Data

Figure 4.11, shows the Wide-Field Infrared Survey Explorer (WISE) band 1 (WISE1) Near Infrared (NIR) $3.4 \mu\text{m}$ emission map from the $z = 0$ Multiwavelength Galaxy Synthesis (z0MGS) atlas (Leroy et al., 2019). The $3.4 \mu\text{m}$ NIR emission traces stellar structure and is often used to measure the total stellar mass of a population. Overlaid are both HI 21-cm integrated intensity contours in white and CO (1-0) contours in green. The HI contours appear at a single level of 800 K km s^{-1} and the CO contours appear at a level of 1.5 K km s^{-1} . In the image, we can see that the stellar emission from the WISE1 data is coincident with the HI disk and it peaks within the large HI cloud. The CO contours serve to highlight the off-disk cloud on the east (left) side of the galaxy, this cloud is in a region separated from other molecular gas and devoid of stellar emission. This data will later be used to measure the stellar mass density in IC 10 using the $3.4 \mu\text{m}$ mass-to-light ratio $\Upsilon_*^{3.4 \mu\text{m}}$.

4.5 Spectral Line Stacking

As seen in figure 4.10 and discussed in Leroy et al. (2006), the CO emission is concentrated in regions with high HI column density. However, the CO emission is only a fraction of the brightness of the HI and as a result, is not visible to the same extent as the atomic gas. Therefore, the presence of atomic hydrogen does not guarantee the presence of CO emission and regions with strong HI emission can be associated with strong CO emission, faint CO, or none at all. The HI extends over the entire IC 10 disk and our goal is to recover faint CO emission within regions that have a strong atomic gas component but that do not have a visible molecular gas component. To recover this emission, we need to average over multiple lines of sight.

To accomplish this we will follow a methodology similar to Schrubba et al. (2011) where we will use the `spectral-stack` tool from the signal identification and noise tools for spectral line data cubes software developed as part of the PHANGS Imaging

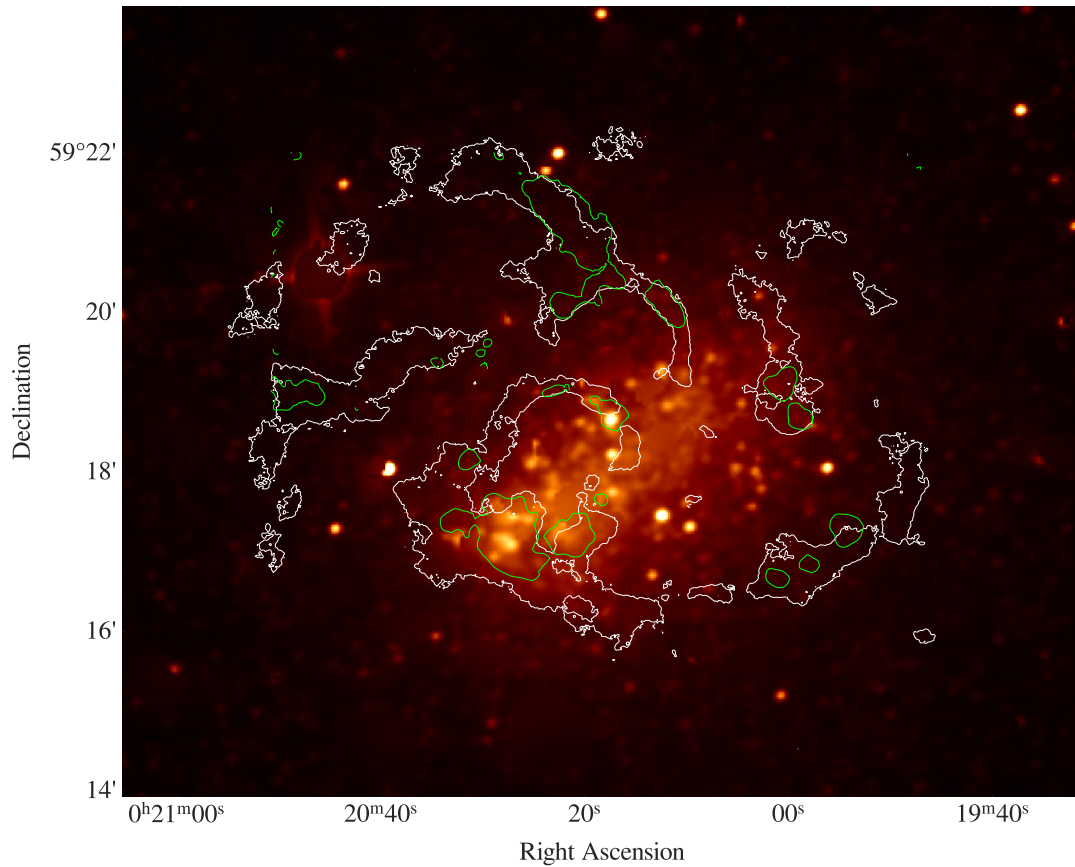


Figure 4.11: WISE 3.4 μm map from the z0MGS atlas (Leroy et al., 2019) showcasing the stellar emission in IC 10. Overlaid in white are HI integrated intensity contours at 800 K km/s, in green CO (1-0) integrated intensity contours can be seen at a level of 1.5 K km/s. The stellar emission in the galaxy is concentrated towards the center-right of the disk with the brightest stellar emission coincident with the large HI cloud at the bottom center of the disk.

Pipeline (Leroy et al., 2021), to shift the local mean velocity of the CO spectra to a common velocity of 0 km/s and then average over the spectra to maximize the signal-to-noise ratio and recover the weak emission.

4.5.1 Stacking Methodology

Due to IC 10's irregular shape instead of stacking by radius from the galactic center, we will bin the data in percentiles of HI brightness and stack the CO emission within these regions. The first step is to create a label map to bin each position in both the CO and HI images based on the atomic hydrogen brightness. We create 11 bins splitting the HI moment 0 integrated intensity data into 45-100th percentiles bins with each bin covering 5% of the brightness. The first bin includes the 95-100th percentiles, the second 90-95th percentile, and so on, continuing to the final bin containing the 45-50th percentiles. Below this bin, the data are noise dominated, and we find no evidence of CO emission in our stacking results.

Next, we need to estimate the central velocity of the CO spectra. The CO moment 1 intensity-weighted velocity map is a good indicator of the velocity of the line in regions of bright CO emission, however in regions with faint emission the SNR of the CO is too small and we do not recover the dim emission. Instead, we use the HI moment 1 central velocity map as a proxy for the velocity of the molecular gas. This works as the atomic gas has relatively constant and bright emission across the whole disk of IC 10 making it easy to measure the velocity in regions with dim molecular gas which is only bright towards the center and a few locations with higher HI column density. This assumption that the HI velocity is a good approximation for the CO velocity is shown to hold in Schruba et al. (2011) figure 1. This can also be seen to hold later in the central panel of figure 4.24 in section 4.7. This figure shows the central velocity relation between the CO emission and the HI component associated with the CO is mostly linear.

Now, using the signal identification `spectral-stack` tool we input the CO inte-

grated intensity map, the label map, and the HI central velocity map. This then uses the velocity map to shift the local mean velocity of each CO spectrum to 0 km/s. We then average these CO spectra in each bin and expect to see the CO line emerge at $v = 0$. To create the label map we use the highest resolution $\sim 4.5''$ moment 0 integrated intensity map to bin the CO data. We then use a lower spectral resolution HI cube at ~ 4 km/s to estimate the central velocity of the CO spectra. This is a lower velocity resolution however it has a higher signal-to-noise ratio which results in a better central velocity estimation and we recover more CO emission. The last step in the stacking is to create an “HI-on-HI” stack to compare with the CO. To do this we follow the same procedure as above but replace the CO cube with the HI cube convolved to the CO resolution and reprojected to the CO pixel grid.

Following the stacking, we then fit the spectra with a Moffat profile using `lmfit` (Newville et al., 2015). This distribution was selected as it is much better at reconstructing the wings of the spectra when compared to a Gaussian or a Lorentzian distribution. Most of the recovered lines were represented well with the default Moffat distribution, however, in the faintest regions (rows 7 and 8 of figure 4.12) baseline effects are more noticeable, we used a composite Moffat and linear model to perform baseline subtraction for the final models.

From our fits, we receive the CO & HI integrated intensity [K km/s], the line width [km/s], and the central velocity [km/s] which shifts slightly around 0 km/s, our chosen velocity. These results can be seen in table 4.2. Next, from the HI integrated intensity, we can calculate the column density of the atomic hydrogen in H nuclei/cm² as defined by

$$\left(\frac{N_{\text{H}}}{\text{cm}^{-2}} \right) \simeq 1.82 \times 10^{18} \int \left[\frac{T_{\text{b}}(\nu)}{\text{K}} \right] d \left(\frac{v}{\text{km s}^{-1}} \right) , \quad (4.9)$$

where the integral represents the integrated intensity in units [K km/s]. To compare with the HI column density N_{H} we calculate the molecular hydrogen column density

N_{H_2} in H nuclei/cm² similarly to the atomic hydrogen by using

$$\left(\frac{N_{\text{H}_2}}{\text{cm}^{-2}}\right) \simeq X_{\text{CO}} \int \left[\frac{T_b(\nu)}{K}\right] d\left(\frac{v}{\text{km s}^{-1}}\right), \quad (4.10)$$

where X_{CO} is the CO-to-H₂ conversion factor defined by

$$X_{\text{CO}} = (2 \pm 0.6) \times 10^{20} \text{ cm}^{-2} (\text{K km s}^{-1})^{-1}. \quad (4.11)$$

We chose to use the Galactic X_{CO} , as Leroy et al. (2006) show the molecular clouds in IC 10 are similar to Galactic GMCs. To compare our results with other galaxies, we derive a column density scaling relation from the first equation in table 7 of Eibensteiner et al. (2024):

$$\log_{10} R_{\text{mol}} = -0.9 + 0.73 \times \log_{10} \left(\frac{\Sigma_{\text{gas}}}{\text{M}_{\odot} \text{pc}^{-2}}\right), \quad (4.12)$$

where R_{mol} is the molecular gas fraction $R_{\text{mol}} = \Sigma_{\text{H}_2}/\Sigma_{\text{HI}}$, Σ_{gas} is the total gas mass surface density ($\Sigma_{\text{gas}} = \Sigma_{\text{HI}} + \Sigma_{\text{H}_2}$), Σ_{HI} is the atomic gas mass surface density and Σ_{H_2} is the molecular gas mass surface density. The gas mass surface densities are related to the integrated intensity through

$$\Sigma_{\text{HI}} [\text{M}_{\odot} \text{pc}^{-2}] = 2.0 \times 10^{-2} I_{\text{HI}} [\text{K kms}^{-1}] \cos(i), \quad (4.13)$$

and through

$$\Sigma_{\text{H}_2} [\text{M}_{\odot} \text{pc}^{-2}] = \alpha_{\text{CO}(1-0)} R_{21}^{-1} I_{\text{CO}} [\text{K kms}^{-1}] \cos(i). \quad (4.14)$$

Here, I_{HI} and I_{CO} are the atomic hydrogen HI and molecular CO integrated intensities respectively, $\alpha_{\text{CO}(1-0)}$ is the CO-to-H₂ conversion factor to convert from integrated intensity to mass surface density and R_{21} is the CO line ratio $R_{21} = 0.65$ (Eibensteiner et al., 2024), and i is the inclination of the galaxy (45°). Taking the above equations and assuming the atomic gas is dominant over the molecular gas ($\Sigma_{\text{gas}} \approx \Sigma_{\text{HI}}$) we can rearrange and find

$$N_{\text{H}_2} [\text{H nuclei/cm}^2] = (2.95 \times 10^{-16}) \frac{R_{21}}{\alpha_{\text{CO}} \cos i} [N_{\text{HI}} \cos i]^{1.75}. \quad (4.15)$$

4.5.2 Results

The result from the CO stacking process can be seen in the left column of figure 4.12 where the uppermost row shows the stacks in each bin compared with each other, the second row corresponds to the brightest region and the bottom row corresponds to the dimmest. The uppermost row in figure 4.12 shows all of the spectral stacking profiles for each of the different bins in relation to each other where a bump at 0 km/s can be seen, which corresponds to the recovered faint CO line. In the right column of the figure, we can see the HI-on-HI stacks for comparison, which are much more consistent down to the dimmest regions due to the brightness of the HI. The properties of the lines can be seen in table 4.2, including the line widths and integrated intensities.

We recovered CO emission down to the 45-50th % brightest HI regions corresponding to a recovered integrated intensity in the dimmest region of ~ 0.0111 K km/s. In total, we recovered a total integrated intensity of ~ 3.75 K km/s from our CO stacking. Compared with the average integrated intensity in the percentiles of brightness bins without stacking, we find zero CO emission and only noise dominated negative values in bins lower than the 70% - 75% brightest bins. In the 70% - 75% bin we find an integrated intensity of 0.007 K km/s as compared to the 0.0818 K km/s found when stacking. In total, we find an integrated intensity of 3.047 K km/s when we don't shift the CO velocities. Therefore, using this stacking technique we recover 23% more CO emission than before. Worth noting is the high error in the CO FWHM in the 50% - 55% and 45% - 50% bins. These errors are likely due to a poor fit of the data caused by larger baseline effects and a peak value much closer to the noise in the CO data $\sigma \approx 0.0065$ K.

From our spectral stacking results, we can report three findings. First, we can see from 4.13 that $N_{\text{H}_2} \leq N_{\text{HI}}$ in all of the disk stacking bins, consistent with what we expect to see in a dwarf galaxy. In this figure, we can also see a scaling relation represented as a black dotted line which was derived from the first scaling relation

Table 4.2: IC 10 spectral stacking results over the central disk. Spectral stacking was performed by binning the data into 11 equal-sized bins based on HI integrated intensity, shifting the spectra to a common velocity before averaging over all the spectra in a given bin. The 95-100% bin contains the brightest 5% of HI pixels. The integrated intensity values were found by integrating the spectra seen in figure 4.12 and the full-width half-maximum values were taken from the Moffat fits using `lmfit` (Newville et al., 2015). Bins below 45% brightest were not included as no CO emission was able to be recovered.

| Bin | HI Integrated Intensity [K km/s] | CO Integrated Intensity [K km/s] | HI FWHM [km/s] | CO FWHM [km/s] |
|------------|-------------------------------------|-------------------------------------|-------------------|-------------------|
| 95% - 100% | 2149.6 \pm 0.53 | 2.44 \pm 0.0022 | 20.3 \pm 0.29 | 12.9 \pm 0.25 |
| 90% - 95% | 1425.0 \pm 0.50 | 0.51 \pm 0.0012 | 17.6 \pm 0.34 | 10.1 \pm 0.36 |
| 85% - 90% | 1183.6 \pm 0.51 | 0.29 \pm 0.0008 | 16.2 \pm 0.40 | 10.2 \pm 0.46 |
| 80% - 85% | 1018.4 \pm 0.55 | 0.16 \pm 0.0007 | 14.6 \pm 0.45 | 9.8 \pm 0.61 |
| 75% - 80% | 888.1 \pm 0.50 | 0.10 \pm 0.0006 | 13.2 \pm 0.42 | 9.4 \pm 0.74 |
| 70% - 75% | 778.8 \pm 0.51 | 0.08 \pm 0.0005 | 11.6 \pm 0.40 | 8.8 \pm 0.80 |
| 65% - 70% | 682.2 \pm 0.47 | 0.05 \pm 0.0004 | 10.8 \pm 0.38 | 9.0 \pm 0.87 |
| 60% - 65% | 594.8 \pm 0.47 | 0.03 \pm 0.0003 | 9.6 \pm 0.35 | 6.9 \pm 0.72 |
| 55% - 60% | 514.4 \pm 0.45 | 0.02 \pm 0.0003 | 8.8 \pm 0.32 | 7.8 \pm 1.73 |
| 50% - 55% | 437.7 \pm 0.44 | 0.01 \pm 0.0002 | 8.0 \pm 0.29 | 9.0 \pm 37.77 |
| 45% - 50% | 364.9 \pm 0.43 | 0.01 \pm 0.0003 | 7.4 \pm 0.27 | 7.4 \pm 267.83 |

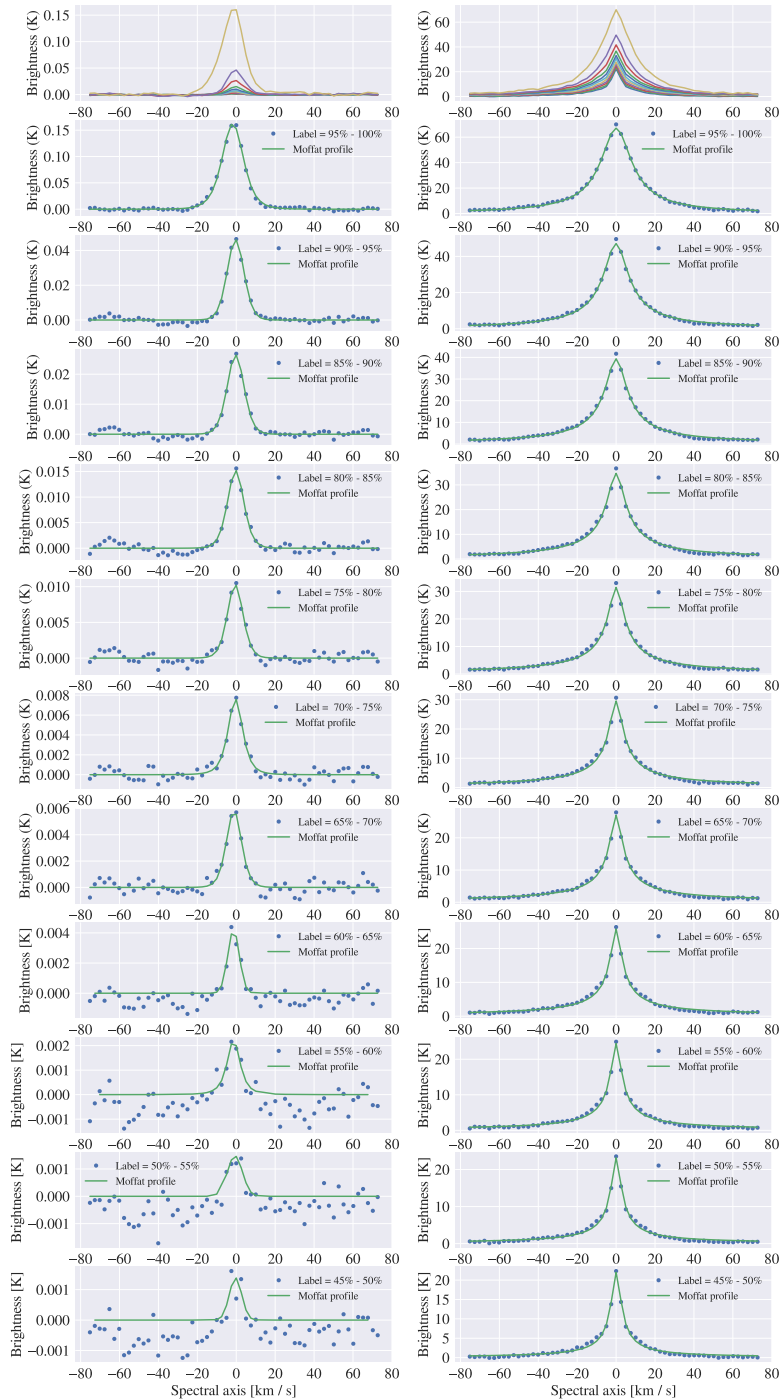


Figure 4.12: CO (1-0) & HI 21-cm line spectral stacking results. The left column in the figure corresponds to the CO (1-0) stacks and the right column is the HI-on-HI spectral stack results. The blue points represent the data and the green line is the Moffat profile fit with `lmfit` (Newville et al., 2015). The top row of each column shows all the stacks in one figure. Starting with the second row and going down we have the brightest bins at 95% - 100% decreasing in 5% bins until the dimmest bin at the bottom which corresponds to the 45% - 50% brightest HI pixels.

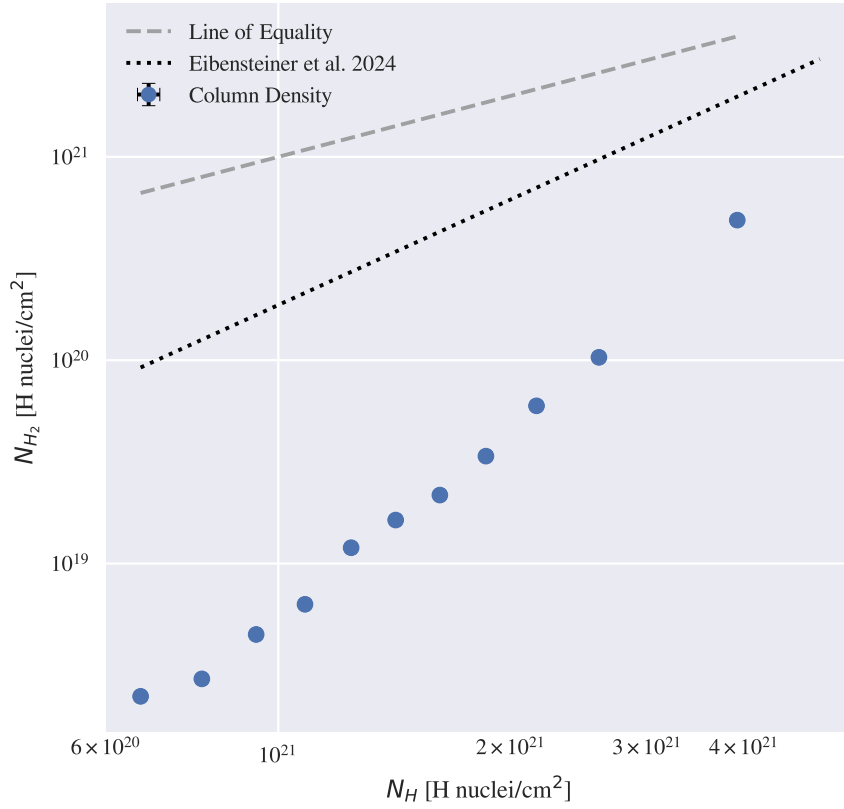


Figure 4.13: Column density of hydrogen nuclei/cm² from atomic and molecular hydrogen. The vertical axis is the log-scale column density from molecular hydrogen calculated with equation 4.10. The horizontal axis shows the log-scale column density from atomic hydrogen calculated with equation 4.9. The dashed grey line represents the line of equality and the dotted black line is a column density scaling relation derived from Eibensteiner et al. (2024) and seen in equation 4.15.

in table 7 from Eibensteiner et al. (2024) as discussed above. To calculate N_{H_2} we need the CO-to- H_2 conversion factor, X_{CO} and here we use the Galactic value for X_{CO} . However, the CO-to- H_2 conversion factor is uncertain in low metallicity dwarf galaxies such as IC 10 leading to some uncertainty in the H_2 column density (Bolatto et al., 2013). Second, we can see from table 4.2 that the CO line widths are almost always smaller or of similar widths to that of the HI. This is likely due to the multi-component ISM of the HI emission which can be seen in the following section. Finally, using this technique we find we are able to recover 23% more CO emission than before.

4.6 Gaussian Decomposition

4.6.1 Method

In this section, we attempt to decompose the HI and the CO emission into one or two component Gaussians. To do this we use The Regularized Optimization for Hyper-Spectral Analysis (ROHSA) tool (Marchal et al., 2019). This is a Gaussian decomposition algorithm designed to separate diffuse sources in hyper-spectral data. It was specifically designed to extract the multi-phase structure of the HI 21-cm line emission, providing a means to map each phase of the Neutral interstellar medium separately. In this thesis, we do not separate the phases of the ISM and strictly analyze the kinematic components in the HI emission. Normally, this approach is restricted to Galactic and Magellanic clouds as it requires high spectral resolution. LGLBS is the first observations that allow Gaussian decomposition and multi-component analysis in these systems.

The goal of our analysis is to decompose the HI into regions where it can be represented by a single Gaussian component and regions where multiple Gaussian components are needed and then split the HI components into two separate maps. Regions with multiple HI components could be regions with two distinctly separate components at different velocities or regions with a narrow and wide HI component

covering a similar velocity range. We want to investigate any regions with complex kinematics or morphology such as regions with two distinct HI components, regions with high dispersion, or regions associated with the HI holes and shells.

ROHSA has six inputs, The number of Gaussian components N , four hyper-parameters λ_i , and the maximum number of iterations of the algorithm. Following Marchal et al. (2019), we choose our parameters such that we ensure complete encoding of the signal. In our data, we found we needed only 1-2 Gaussian components for the HI emission and only one component for the CO molecular gas. We choose our hyper-parameters to receive a spatially coherent solution that describes the data well without being too spatially coherent and wiping out small-scale fluctuations or providing a bad fit to the data. We found a value of $\lambda_i = 50$ worked appropriately.

We used these parameters to decompose three HI data cubes. The first cube we tried was the full resolution $\sim 4.5''$ and ~ 0.4 km/s cube. While we were able to decompose the high-resolution data we found with the lower signal-to-noise ratio it was harder to make out the distinct components within the HI. We then used a lower spatial resolution HI cube convolved to the CO cube resolution of $8.5''$, this increased the signal-to-noise ratio of the data while keeping the same pixel scale and velocity resolution. Finally, for direct comparison with the CO data we ran ROHSA on the $8.5''$ cube spatially smoothed to the CO velocity resolution of 2.5 km/s and reprojected to the CO coordinates and pixel scale.

Once we have decomposed the data into Gaussian components, we choose which regions need one or two components using the Bayesian Information Criterion (BIC) for Gaussians. This is a model selection criterion in which models with a lower BIC are preferred. Models with a higher number of components are punished such that if a data sample can be represented equally well by both a single and multi-component Gaussian, the single-component fit will be chosen. The BIC can be written in terms of the deviance as

$$\text{BIC} = \chi^2 + k \ln(n) , \tag{4.16}$$

where k represents the number of parameters estimated by the model ($k = 3$ for a one component Gaussian), n is the number of data points and χ^2 is the deviance given by

$$\chi^2 = \left(\frac{y - y_{\text{fit}}}{\sigma_{T_b}} \right)^2. \quad (4.17)$$

Here, y is the data and y_{fit} is the Moffat profile fit, σ_{T_b} is the noise in the data cube or the error in the brightness temperature T_b and is calculated using the `signal-id` tool from the PHANGS Imaging Pipeline (Leroy et al., 2021). This tool returns a 3D data cube for the noise in each pixel and velocity channel. For our analysis we found the noise did not change significantly across the image and therefore to accelerate our computation times we used a 2D noise map with a constant value across the image.

The final step is to split the HI into two separate component maps, a primary and a secondary component. We split the HI components in two separate ways, in the first method we simply take all the single component regions the brightest of the two components in the multi-component regions as the “primary” component and the dimmer component as the “secondary”. The second method we use to split the HI components is by their proximity to the CO 1-0 component in velocity space. This is in an effort to determine which component the CO emission is associated with and how its properties (Amplitude, central velocity, and dispersion) relate to the HI emission. In this scenario, the “primary” component is the one closest to the CO velocity and the single components. The “secondary” component is therefore the remaining component with a velocity further from the CO. These HI components will be explored more in section 4.7 when comparing the full region to an off-disk CO molecular cloud.

4.6.2 Results

The results of the Gaussian decomposition can be seen in figures 4.14 and 4.15. These figures show the components of the Gaussian decompositions, the amplitude can be seen in the far left plot, the central velocity in the center plot, and the dispersion in

the far right. The first row in figure 4.14 shows the components for a one component decomposition of the HI data over the same region as the CO emission. The middle and bottom rows show the same data as the first row except for a two component decomposition. Figure 4.15 shows the CO Gaussian decomposition components. The maximum amplitude (brightness temperature) observed in the single component HI results is ~ 100 K, the central velocity on the eastern side of the disk is ~ -250 km/s while on the west side, it is ~ -400 km/s. The peak dispersion in the HI is found to be ~ 100 km/s in the large HI cloud and heading towards the shell region where we see multi-component HI.

In the two component, HI decomposition we can see ROHSA sets the first component mostly in the northern part of the disk along the shell structures, and the second component is concentrated to the south. However, it is worth noting that ROHSA does not distinguish between components by any specific parameter (i.e. ROHSA does not set the first component to be the brighter component and the second component the dimmer one.) As a result, which component is which will often switch from one region to the next. In the CO Gaussian component plots, we can see peak emission tracing the bright HI and shells. This data has been masked to only include regions with bright CO emission. The central velocity is ~ -325 km/s on the east side and ~ -350 km/s on the west.

As discussed in the last section, we split the HI components in two ways. The first by their peak brightness temperatures and the second by their proximity to the CO emission in velocity space. When splitting by their brightness, the primary component is the brighter one and the secondary component is dimmer. In these two components, we find the primary component totals an integrated intensity of $\sim 4.47 \times 10^7$ K km/s and the secondary component totals $\sim 8.95 \times 10^6$ K km/s.

In the second method, the primary component is the one closest to the CO in velocity space and the second component is further away. We find here that the primary component totals an integrated intensity of 4.46×10^7 K km/s. The secondary

component has an integrated intensity of 9.07×10^6 K km/s. This indicates that the CO component is likely associated with the brighter HI component.

Gaussian decomposition spectra examples can be seen in figures 4.16,4.17 and 4.18. These are spectra from the HI 8.5'' cube which has the highest signal-to-noise ratio while maintaining a high spectral resolution. Figure 4.16 shows a region with a narrow and wide component associated with the HI emission. This corresponds to the bright HI cloud. The narrow component has a peak brightness temperature of ~ 63 K, a central velocity of ~ -315 km/s and a ~ 16 km/s dispersion. The wide component has a peak brightness temperature of ~ 35 K, a central velocity of ~ -341 km/s and a ~ 64 km/s dispersion. In figure 4.17 we see a region with two distinct HI components. The components have similar peak brightness temperatures of ~ 18 K and ~ 24 K respectively. Notably the components have central velocities of ~ -380 km/s and ~ -335 km/s, separated by ~ 45 km/s. Each component has similar dispersion at ~ 24 km/s and ~ 30 km/s. Figure 4.18 shows a region with only one HI component. In this region, we find a peak brightness temperature of ~ 300 K and a central velocity and dispersion of ~ -345 km/s and ~ -16 km/s respectively.

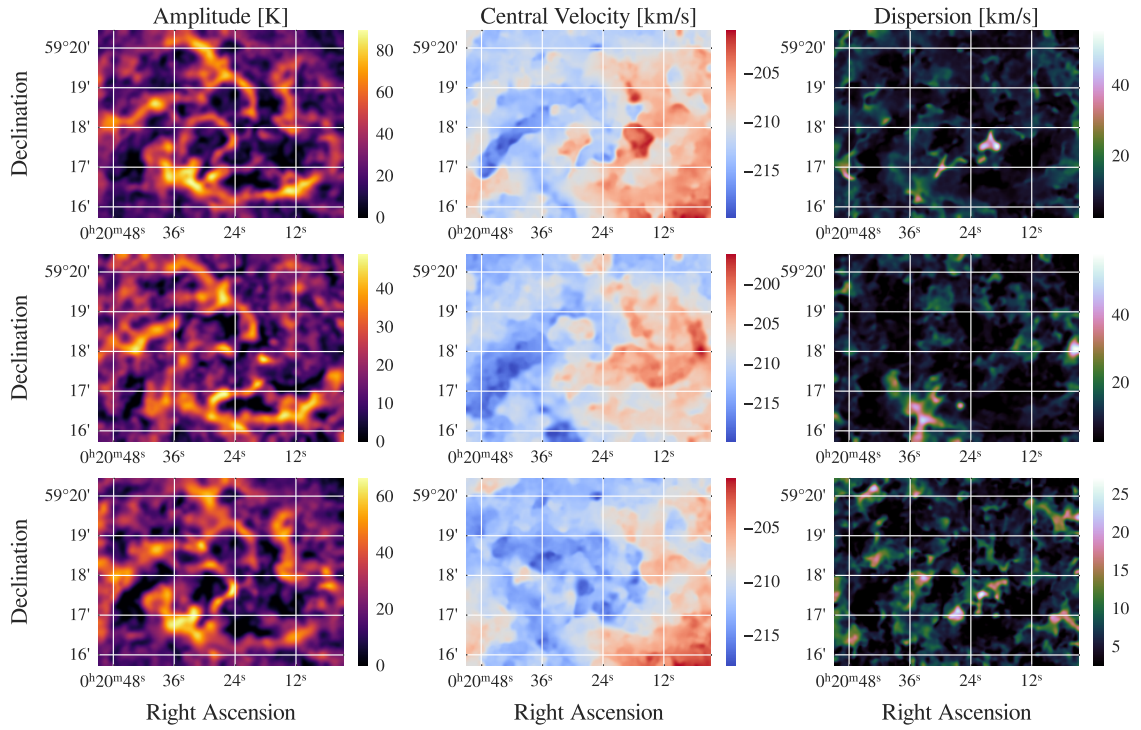


Figure 4.14: HI Gaussian Decomposition Results of IC 10's disk from ROHSA (Marchal et al., 2019). The top row shows the one component decomposition parameters. The second and third rows show the HI two component decomposition parameters, the second row is the first of the two components and the third row is the second of the two components. The left column shows the Amplitude of the Gaussian [K], the center column shows the central velocity of the Gaussian [km/s] and the right column shows the velocity dispersion of the Gaussian [km/s].

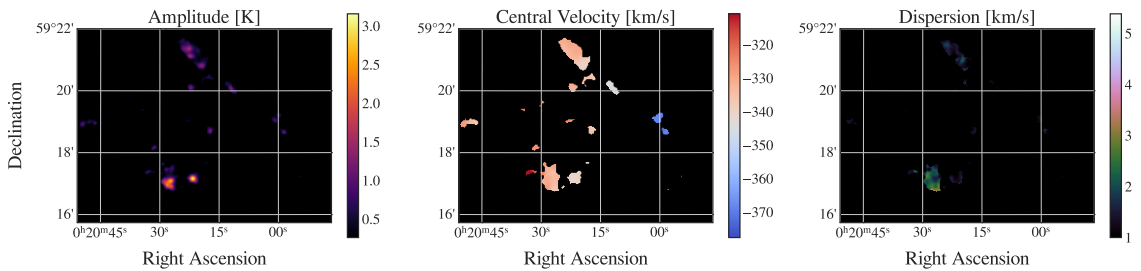


Figure 4.15: CO 1-0 Gaussian decomposition results of IC 10's disk from ROHSA (Marchal et al., 2019). The Left panel shows the Amplitude of the Gaussian [K], the center panel shows the central velocity of the Gaussian [km/s] and the right panel shows the velocity dispersion of the Gaussian [km/s].

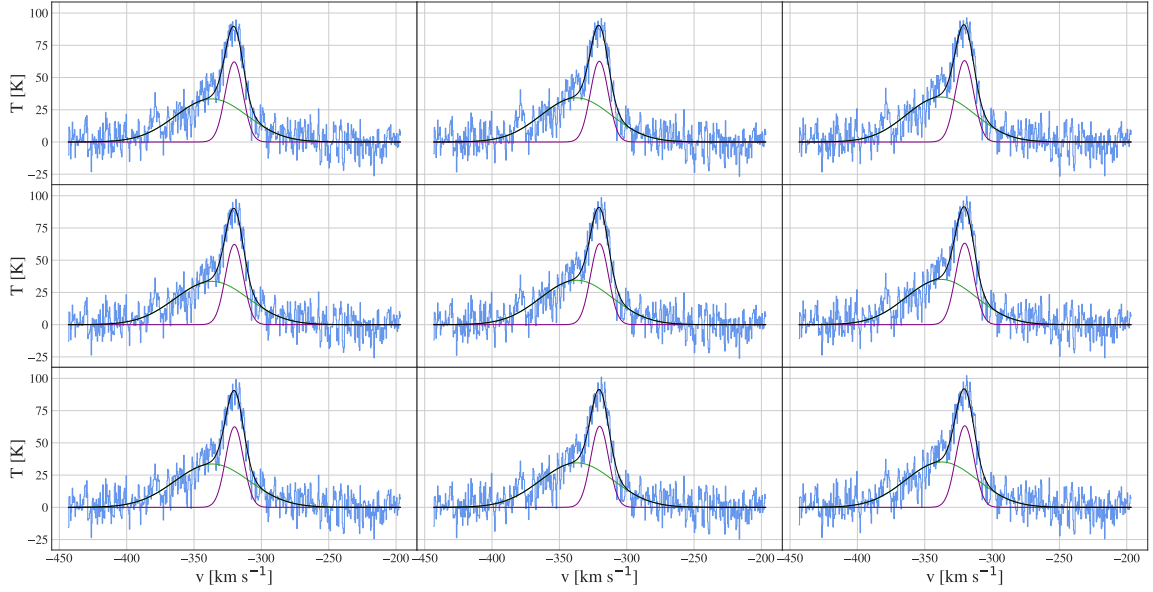


Figure 4.16: Gaussian decomposition spectra example. These spectra show a two component decomposition with both a wide and a narrow component. The narrow component peaks at a brightness temperature of ~ 63 K and the wide component has a peak value of ~ 35 K. These spectra are from a region within the large HI cloud at a RA $\sim 0^{\text{h}}20^{\text{m}}30^{\text{s}}$ and DEC $\sim 59^{\circ}17'$.

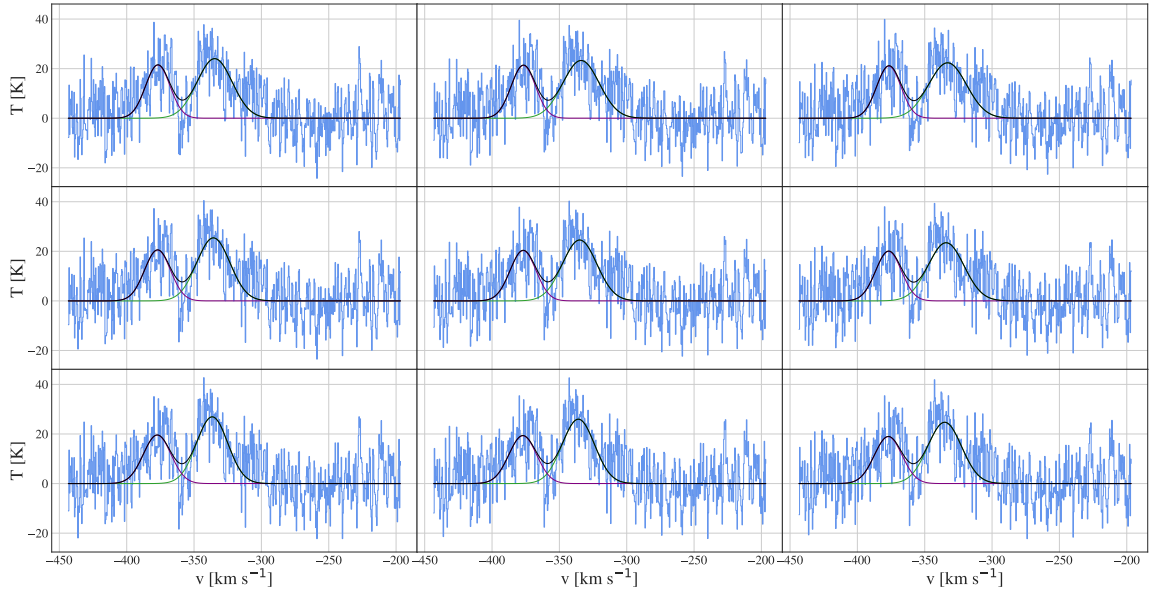


Figure 4.17: Gaussian decomposition spectra example. This figure shows a two component decomposition with two separate distinct components. One component has a peak amplitude of ~ 18 K and the other ~ 18 K. The components have central velocities of ~ -438 km/s and ~ -336 km/s, separated by ~ 100 km/s. These spectra are from a region surrounded by HI holes and shells at a RA $\sim 0^{\text{h}}20^{\text{m}}10^{\text{s}}$ and DEC $\sim 59^{\circ}18.5'$.

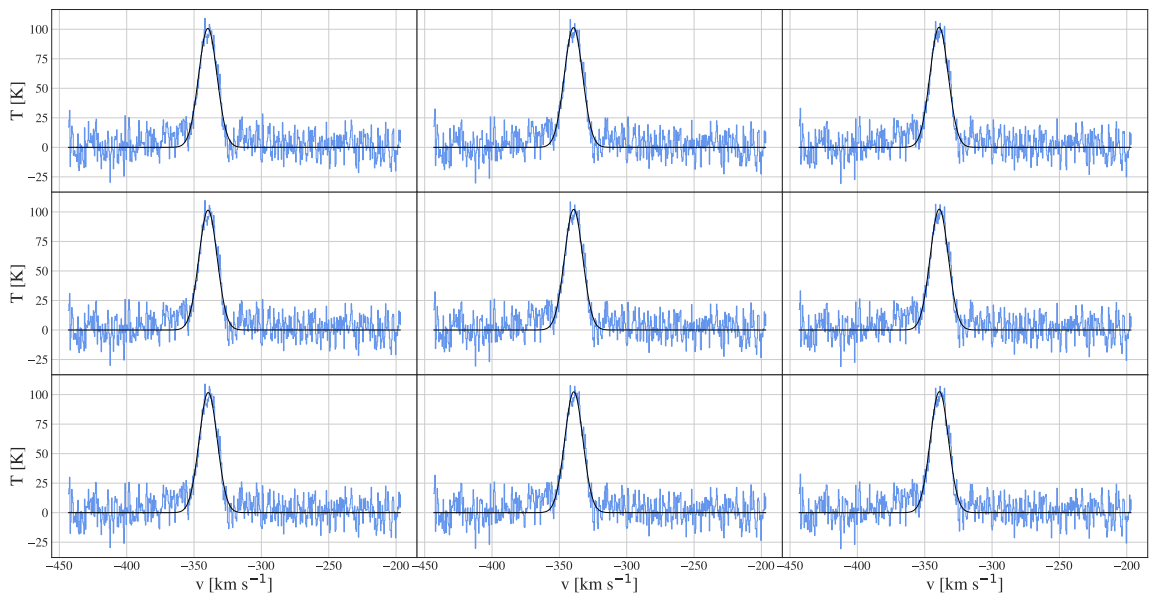


Figure 4.18: Gaussian decomposition spectra example. These spectra show a one component decomposition that peaks at a brightness temperature of ~ 100 K and a central velocity of ~ -345 km/s. These spectra are from a region within the large HI cloud at a RA $\sim 0^{\text{h}}20^{\text{m}}22^{\text{s}}$ and DEC $\sim 59^{\circ}17'$.

4.7 Off-disk Cloud

In this section, we use the previously discussed techniques and apply them to analyzing a region of interest in more detail. This is the off-disk molecular cloud which can be seen in figure 4.19. This cloud appears to have a size of $\sim 1.5' \times 0.5'$ and looks to be made up of two or three smaller clouds visible as peaks in the CO emission. The cloud is $\sim 7.5'$ away from the center of the disk, has a total CO integrated intensity of $\sim 2.2 \times 10^3$ K km/s or an equivalent molecular gas mass of $\sim 4.73 \times 10^5 M_{\odot}$ using the CO-to-H₂ conversion factor. This is a unique cloud due to it being situated in a region that is devoid of stellar emission and isolated from other molecular clouds.

4.7.1 Methods

In order to analyze the cloud we employ three techniques, two of which were discussed in detail for the disk of IC 10, that is, the spectral stacking and the Gaussian decomposition techniques. The third method we use is to create a position-velocity diagram over the off-disk cloud.

For the spectral stacking, we follow the same procedure as in section 4.5. However, we also created a small sub-cube over the region of the off-disk cloud. We then once again binned the full disk region of the data by the HI brightness and sliced the bin map to create a smaller map over the off-disk cloud. We then created a plot showing the stacks in each bin as before which can be seen in figure 4.20. Following the previous method we then found the column density of the gas in each bin which is shown in figure 4.21.

New from the previous section we now calculate the molecular gas fraction R_{mol} and the dynamical equilibrium pressure P_{DE} . The P_{DE} is the expected average ISM pressure needed to balance the weight of the ISM in the gravitational potential of the galaxy. Blitz and Rosolowsky (2006) and Leroy et al. (2006) found a relation between the P_{DE} and the molecular gas fraction that holds in IC 10. To calculate the

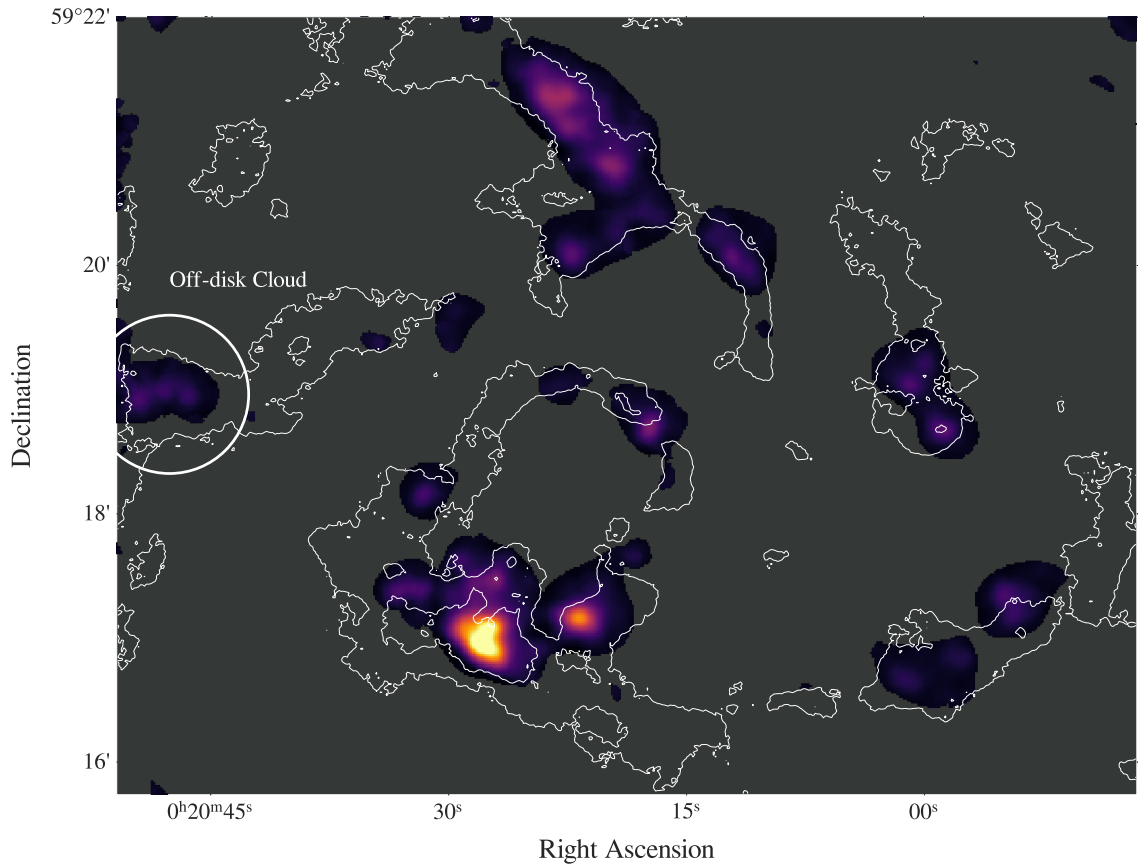


Figure 4.19: The CO (1-0) Moment 0 integrated intensity map [K km/s] with HI moment 0 contours overlaid. The HI contours are at levels 800, 1500, and 2500 K km/s. The off-disk cloud is highlighted and circled on the left side of the image.

dynamical equilibrium pressure we use

$$P_{\text{DE}}[\text{k}_B \text{ K cm}^{-3}] = \left(\frac{\pi G}{2} \Sigma_{\text{gas}}^2 + \Sigma_{\text{gas}} \sqrt{2G\rho_*} \sigma_{\text{gas},z} \right), \quad (4.18)$$

where the first term is the weight of the ISM due to the self-gravity of the ISM disk and the second term is the weight of the ISM due to stellar gravity (Sun et al., 2020). Here the gravitational constant $G = 4.30 \times 10^{-3} \text{ pc M}_\odot^{-1} (\text{km s}^{-1})^2$.

Following this equation, we need the gas mass surface density,

$$\Sigma_{\text{gas}}[\text{M}_\odot \text{ pc}^{-2}] = \Sigma_{\text{HI}} + \Sigma_{\text{H}_2}, \quad (4.19)$$

which needs both the atomic gas mass surface density,

$$\Sigma_{\text{HI}}[\text{M}_\odot \text{ pc}^{-2}] = 2.0 \times 10^{-2} I_{\text{HI}} [\text{K km s}^{-1}] \cos(i) \quad (4.20)$$

and the molecular gas mass surface density,

$$\Sigma_{\text{H}_2}[\text{M}_\odot \text{ pc}^{-2}] = \alpha_{\text{CO}(1-0)} R_{21}^{-1} I_{\text{CO}} [\text{K km s}^{-1}] \cos(i). \quad (4.21)$$

We adopt a CO line ratio ($R_{21} = 0.65$) and CO-to-H₂ conversion factor ($\alpha_{\text{CO}} = 4.3 \text{ M}_\odot (\text{K km s}^{-1} \text{ pc}^2)^{-1}$) from Eibensteiner et al. (2024) From the above values we can then calculate the molecular gas fraction R_{mol} using:

$$R_{\text{mol}} = \frac{\Sigma_{\text{H}_2}[\text{M}_\odot \text{ pc}^{-2}]}{\Sigma_{\text{HI}}[\text{M}_\odot \text{ pc}^{-2}]}, \quad (4.22)$$

Next, we can find the mass-weighted average velocity dispersion given by

$$\sigma_{\text{gas},z} = \frac{\Sigma_{\text{H}_2}}{\Sigma_{\text{gas}}} \sigma_{\text{mol}} + \left(1 - \frac{\Sigma_{\text{H}_2}}{\Sigma_{\text{gas}}} \right) \sigma_{\text{atom}}, \quad (4.23)$$

where σ_{atom} and σ_{mol} are the atomic and molecular gas velocity dispersions respectively. Following Eibensteiner et al. (2024) and Leroy et al. (2008) we adopt a fixed σ_{atom} of 10 km s^{-1} .

To calculate the stellar mass volume density defined as

$$\rho_* = \frac{\Sigma_*}{4h_*}, \quad (4.24)$$

we first need the disk scale height h_* and the stellar mass density Σ_* calculated as follows:

$$\Sigma_* [M_\odot \text{ pc}^{-2}] = 350 \left(\frac{\Upsilon_{3.4\mu\text{m}}}{0.5 M_\odot/L_\odot} \right) I_{3.4\mu\text{m}} [\text{MJy sr}^{-2}] \cos(i), \quad (4.25)$$

where $I_{3.4\mu\text{m}}$ is the WISE1 3.4 μm emission and $\Upsilon_{3.4\mu\text{m}}$ is the 3.4 μm mass-to-light ratio. For our calculations, we assume a mass-to-light ratio of $\Upsilon_{3.4\mu\text{m}} = 0.35 [M_\odot L_\odot^{-1}]$, the average value from Leroy et al. (2021). For the scale height, we use a value of 300 pc as in Leroy et al. (2006). Finally, to compare our dynamical equilibrium pressure values with the literature we take the scaling relation from the fifth equation in table 7 from Eibensteiner et al. (2024):

$$\log_{10} R_{\text{mol}} = -2.1 + 0.4 \times \log_{10} \left(\frac{P_{\text{DE}}}{k_B \text{ K cm}^{-3}} \right). \quad (4.26)$$

Next, taking the results of the Gaussian decomposition we created three plots to highlight the off-disk cloud. We used the HI data convolved to the CO resolution of 8.5'' and reprojected the data to the CO pixel grid to compare accurately. As discussed in section 4.6 we split the HI into two components and found the component associated with CO by its proximity to the CO in velocity space. We then mask the map by including only regions with CO amplitudes larger than the 3σ level. Using this map we plot the CO vs HI amplitude, central velocity, and line widths which can be seen in figure 4.24.

Finally, to create a position velocity diagram we first create a sub-cube over the off-disk cloud in both the HI and the CO data. We then smooth the HI data from 0.4 km/s to 2.5 km/s to match the CO before reprojecting the HI data to the CO coordinates and pixel grid. Next, using the Cube Analysis and Rendering Tool for Astronomy (CARTA, Comrie et al., 2021) we draw a line over the region following the SE - NW direction of the HI shell. This results in figure 4.25.

4.7.2 Results

In figure 4.20 and table 4.3 the results of the spectral stacking for the off-disk cloud region can be seen, including the integrated intensity and line widths. The CO integrated intensity peaks in the 65% - 70% brightest HI bin at 4.05 K km s^{-1} and has a value of 4.05 K km s^{-1} in the 60% - 65% bin. We find a maximum FWHM of 13.0 km s^{-1} in the brightest HI bin and 4.5 km s^{-1} in the 55% - 60% bin. Comparing to the CO stacks from figure 4.12 we can see that these stacks have smaller maximum amplitudes and line widths but larger minimum values. This is unsurprising as the entire region of the off-disk cloud appears within a region of bright HI. This is also the reason we don't find a uniform decreasing trend in the amplitude that we saw in the full disk region stacks. The errors in the FWHM for the off-disk CO stack are significant and are due to a poor fit of the Moffat profile within certain bins, visible in 4.20. Figure 4.21 shows the column density of the HI vs. CO in the disk and in the off-disk cloud labeled in green. The off-disk cloud is entirely contained in a region of bright HI with high column density but visible in the figure is that it maintains a high H2 column density in the dimmer bins as compared to the disk. The black dotted line represents the scaling relation derived from Eibensteiner et al. (2024) visible in equation 4.15.

Figure 4.22 shows the molecular gas fraction vs. the dynamical equilibrium pressure for each of the 11 stacking bins for both the disk and the off-disk cloud region. In this figure we can see in the disk that the $\log_{10}(PDE)$ values range from $\sim 5.5 - 7.0 \text{ k}_B \text{ K km s}^{-1}$ and the $\log_{10}(R_{\text{mol}})$ values range from ~ -2.0 to 0.0 . As expected, the off-disk cloud has both a higher molecular gas fraction and a lower dynamical equilibrium pressure than the disk for the same bins of HI brightness. We can also see the black dotted line showing the scaling relation from Eibensteiner et al. (2024), equation 4.26. Figure 4.23 shows R_{mol} vs. the stellar mass density $\Sigma_* [\text{M}_\odot \text{ pc}^{-2}]$ which clearly demonstrates that the cloud is dominated by gas and contains a high amount

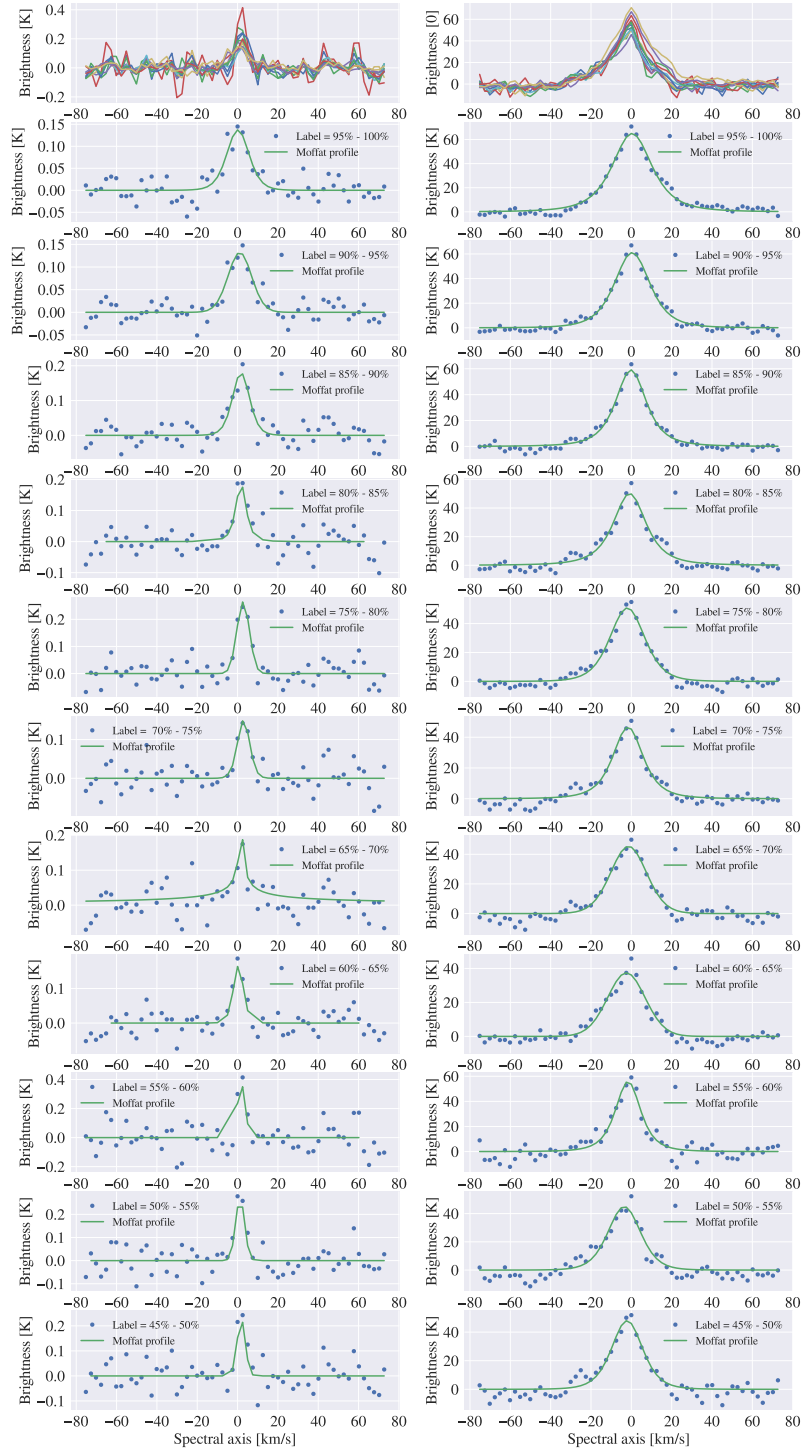


Figure 4.20: CO 1-0 & HI 21-cm line spectral stacking results for the off-disk cloud. The left column in the figure corresponds to the CO (1-0) stacks and the right column is the HI on HI spectral stack results. The top row shows all the stacks in one figure. Starting with the second row and going down we have the brightest bins at 95% - 100% decreasing in 5% bins until the dimmest bin at the bottom which corresponds to the 45% - 50% brightest HI pixels.

Table 4.3: IC 10 spectral stacking results over the off-disk molecular cloud. Spectral stacking was performed by binning the data into 11 equal-sized bins based on HI integrated intensity, shifting the spectra to a common velocity before averaging over all the spectra in a given bin. The 95-100% bin contains the brightest 5% of HI pixels. The integrated intensity values were found by integrating the spectra seen in figure 4.20 and the full-width half-maximum values were taken from the Moffat fits using `lmfit` (Newville et al., 2015). Bins below 45% brightest were not included as no CO emission was able to be recovered.

| Bin | HI Integrated Intensity [K km/s] | CO Integrated Intensity [K km/s] | HI FWHM [km/s] | CO FWHM [km/s] |
|------------|-------------------------------------|-------------------------------------|-------------------|-------------------|
| 95% - 100% | 1848.7 \pm 1.62 | 2.01 \pm 0.018 | 23.1 \pm 0.89 | 13.0 \pm 2.33 |
| 90% - 95% | 1511.0 \pm 1.58 | 1.96 \pm 0.014 | 20.6 \pm 0.81 | 13.8 \pm 2.06 |
| 85% - 90% | 1327.0 \pm 1.53 | 2.02 \pm 0.024 | 17.9 \pm 0.72 | 10.0 \pm 1.90 |
| 80% - 85% | 1212.3 \pm 2.11 | 1.36 \pm 0.027 | 19.1 \pm 1.26 | 6.0 \pm 1.34 |
| 75% - 80% | 1185.2 \pm 1.97 | 2.06 \pm 0.032 | 20.3 \pm 1.17 | 7.3 \pm 900.71 |
| 70% - 75% | 1016.7 \pm 2.12 | 1.18 \pm 0.033 | 17.7 \pm 1.24 | 7.2 \pm 2.23 |
| 65% - 70% | 1040.3 \pm 2.11 | 4.05 \pm 0.072 | 21.1 \pm 1.40 | 6.5 \pm 1492.53 |
| 60% - 65% | 887.8 \pm 1.71 | 1.06 \pm 0.018 | 22.0 \pm 1.41 | 5.9 \pm 0.90 |
| 55% - 60% | 1013.3 \pm 3.82 | 2.32 \pm 1.119 | 14.7 \pm 1.55 | 4.5 \pm 1521.97 |
| 50% - 55% | 967.6 \pm 3.02 | 1.46 \pm 0.045 | 19.0 \pm 1.88 | 5.2 \pm 527.09 |
| 45% - 50% | 1004.7 \pm 2.93 | 1.14 \pm 0.110 | 18.1 \pm 1.65 | 4.8 \pm 1034.40 |

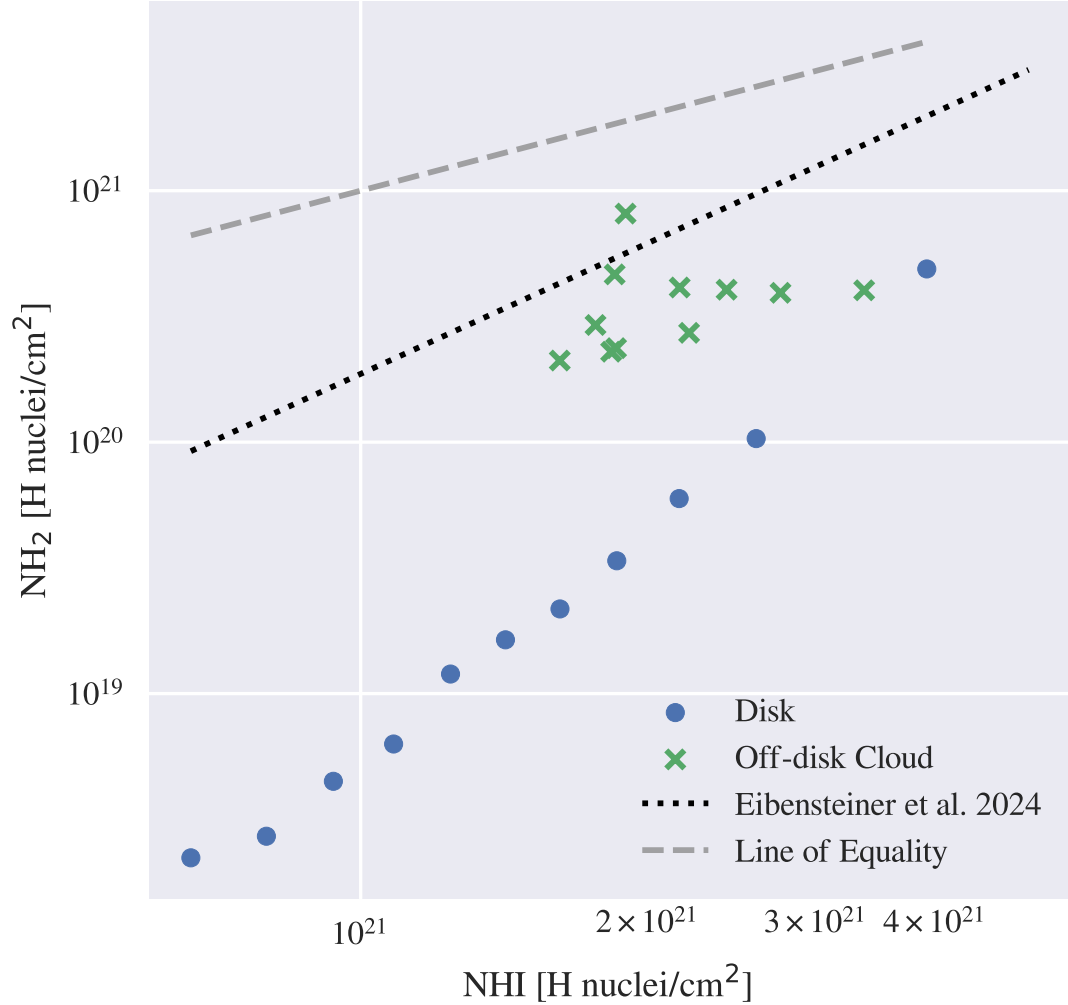


Figure 4.21: Column densities from off-disk cloud stacking results. The atomic hydrogen column density N_{HI} can be seen on the horizontal axis and the molecular hydrogen column density N_{H_2} can be seen on the vertical axis. The disk column densities from 4.13 can be seen in blue points and the off-disk cloud column densities can be seen by green x's. Compared with the disk region, the off-disk cloud has significantly higher column densities. The grey dashed line represents the line of equality and the black dotted line represents the scaling relation from Eibensteiner et al. (2024) seen in 4.15.

of molecular gas. Figure 4.24 shows the Gaussian decomposition results for the CO and the HI components associated with the molecular gas. Here we mask the data and take only points with CO amplitude $\geq 3\sigma$. Here we can see three peaks in the amplitude correlating to the bright CO clouds at the center of the disk, while the majority of the pixels have CO amplitudes between 0.24 K and 1.5 K. In the central velocity plot, we see a linear relationship between the CO and the HI. This is expected as these components are in close proximity to one another in velocity space, however, We can see two groups of points in this plot, one at low velocities at $\sim -380 \text{ km s}^{-1}$ and one at high velocities $\sim -325 \text{ km s}^{-1}$. This lower velocity group corresponds to the CO clouds on the west side of the disk the high groups correspond to most of the bright CO emission in the central disk, shells, and northern disk. In the line width plots we can see that the HI ranges between 1 km s^{-1} and 40 km s^{-1} and the CO ranges between 1 km s^{-1} and 10 km s^{-1} barring some outliers. The minimum line width of 1 km/s is a consequence of the Gaussian decomposition algorithm ROHSA. In all of our plots, we can see that the off-disk cloud is not an outlier in the CO or HI amplitude, central velocity, or line widths. We can also see outlier points that generally correspond to weak CO emission where our Gaussian decomposition is likely not as trustworthy.

In the PV-diagram seen in 4.25, we can see the HI data over a SE - NW slice through the off-disk cloud in the left panel, and in the right panel we can see the CO data over the same slice. Here we can see a relatively consistent velocity of $\sim -330 \text{ km s}^{-1}$ along the slice in both the CO and HI with a slight increase in the HI velocity to $\sim -320 \text{ km s}^{-1}$ at $\sim +5''$ along the slice.

From these results, we can conclude that the off-disk cloud does not display unusual characteristics in its central velocities, amplitudes, or line widths. This is evident from the Gaussian decomposition, the spectral stacking, and the PV-diagram results. However, it is unique in its dynamical pressure equilibrium and molecular gas fraction. Figure 4.23 shows the cloud is dominated by gas and has a small stellar mass density.

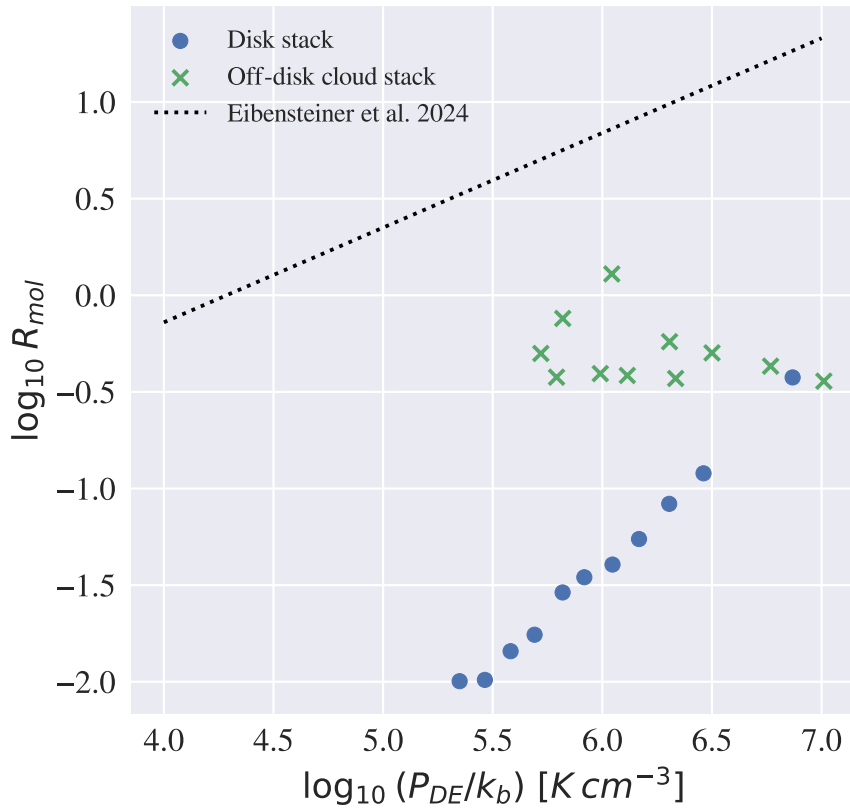


Figure 4.22: Molecular gas fraction vs. Dynamical equilibrium pressure for the spectral stacking bins for both the disk and off-disk molecular cloud. In blue points we can see the points associated with the full disk stacking bins and represented by green x's we can see the off-disk molecular cloud stacks. The dynamical equilibrium pressure P_{DE} was calculated using equation 4.18 and the molecular gas fraction R_{mol} was calculated using equation 4.22. The black dotted line represents the scaling relation from Eibensteiner et al. (2024) as seen in equation 4.26.

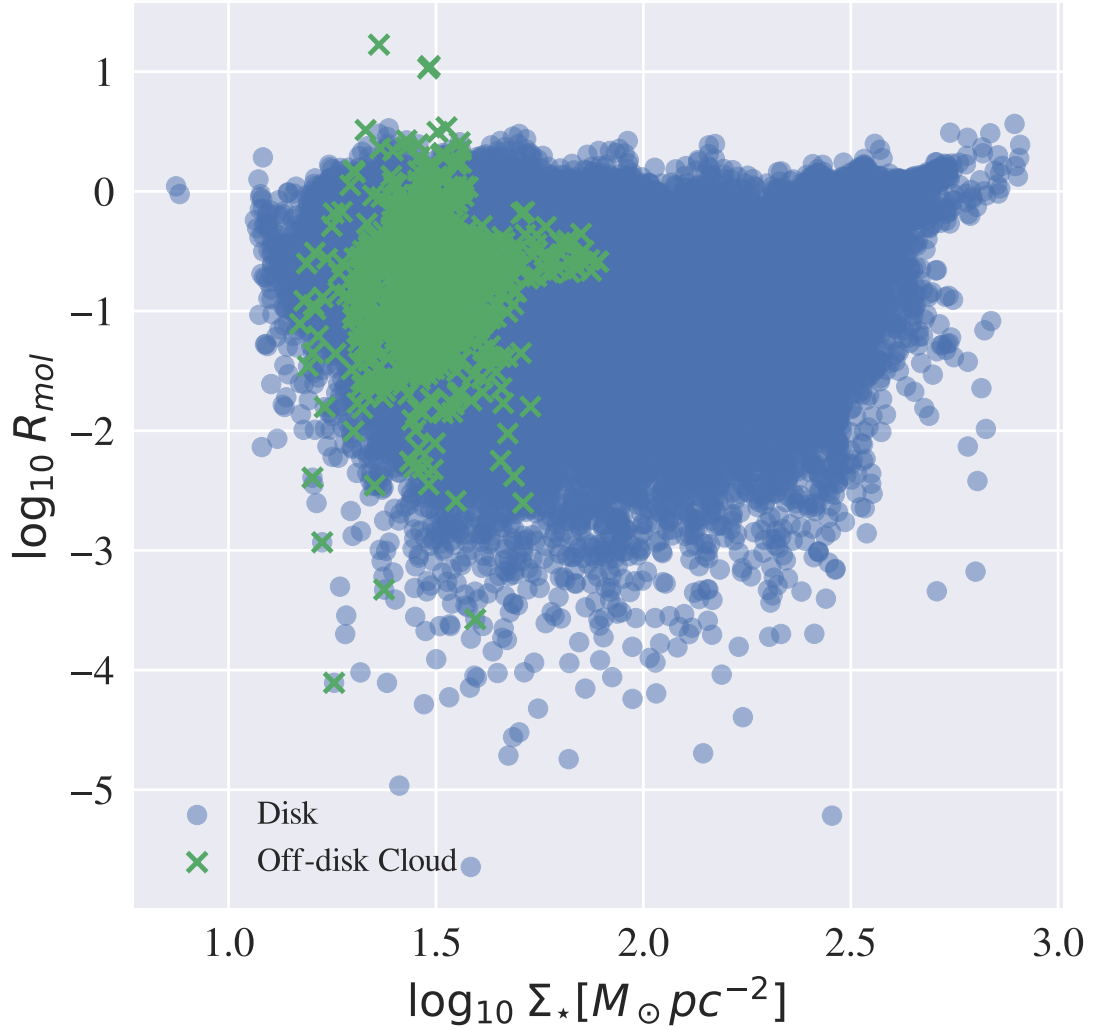


Figure 4.23: Molecular gas fraction vs. Stellar mass surface density. This figure shows the molecular gas fraction R_{mol} vs. stellar mass surface density Σ_* on a pixel-by-pixel basis. The molecular gas fraction was calculated using equation 4.22 and the stellar mass surface density was calculated using equation 4.25. The values for the disk pixels can be seen represented by blue points and the off-disk cloud pixels can be seen as green x's. This shows the off-disk cloud is dominated by gas.

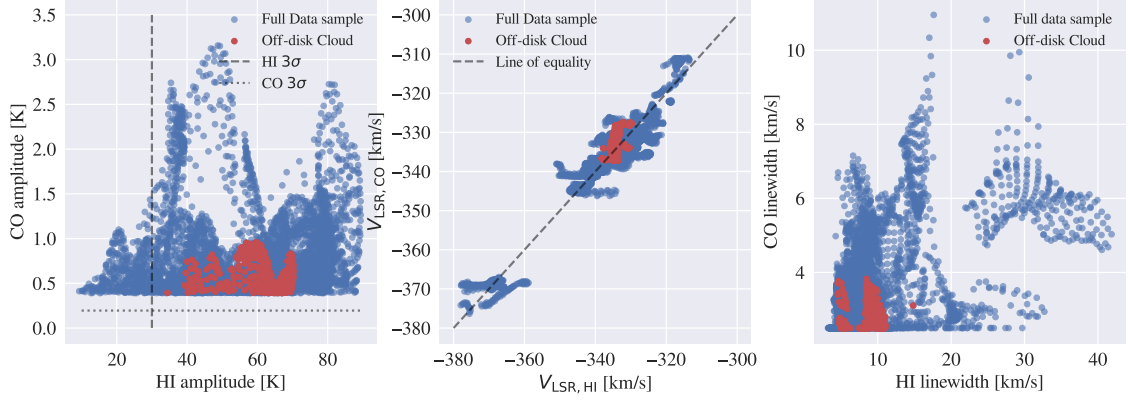


Figure 4.24: Gaussian Decomposition Amplitudes, Central velocities, and Line-widths for the CO Gaussian decomposition vs. the HI Gaussian decomposition. Prior to our analysis we convolved the HI to the CO spatial resolution and reprojected the data to the CO pixel grid. We then spatially smoothed it prior to the Gaussian decomposition of the spectra to ensure an accurate comparison. We masked the data to include only regions that have both bright CO and HI emission and compared the CO one-component decomposition to the HI component closest to the CO in velocity space. In blue we can see the pixels with bright emission in the disk and in red we have highlighted the off-disk molecular cloud.

This is interesting as P_{DE} is known to display a strong relation with the molecular gas fraction that is consistent within the disk of IC 10 (Blitz and Rosolowsky, 2006; Leroy et al., 2006; Eibensteiner et al., 2024). We expect to see a linear effect in the R_{mol} vs. P_{DE} plot for the disk which we see in the stacking plot but is not visible in the pixel plot.

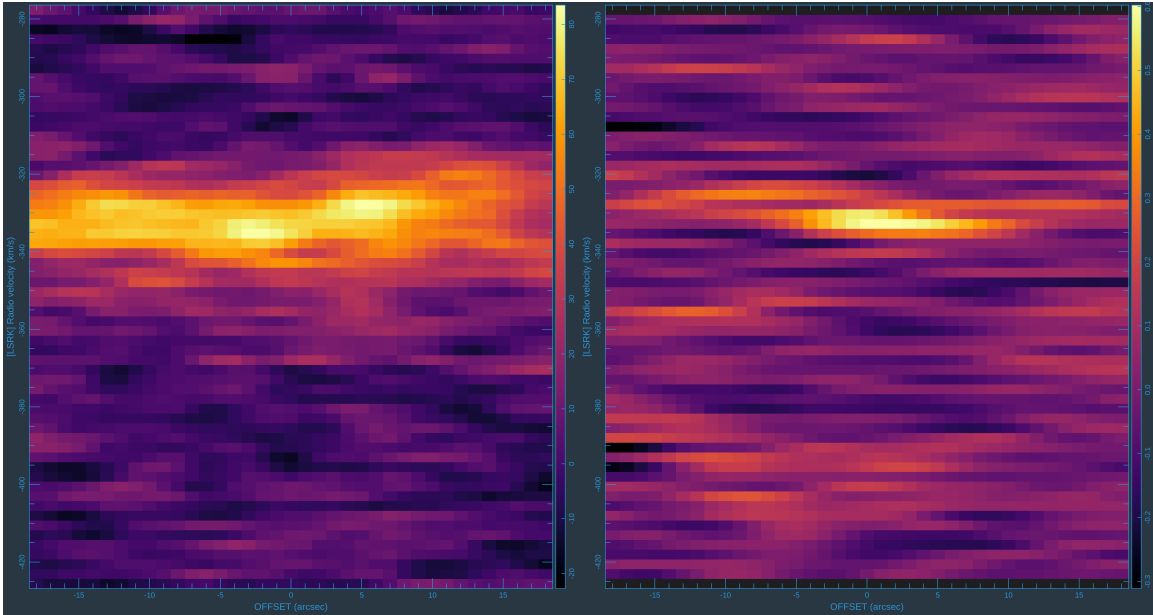


Figure 4.25: Position-Velocity diagram over the off-disk cloud along a slice following the HI emission. The left panel shows the HI atomic hydrogen position velocity diagram using the HI data with convolved and spectrally smoothed to the CO resolution of $8.5''$ and 2.5km/s . The right panel shows the CO (1-0) data over the same slice. Of note is that the off-disk cloud does not have a substantial change in velocity across the slice indicating there may not be multiple HI kinematic components in the region.

Chapter 5

Conclusions & Future Work

5.1 Conclusions

The interstellar medium is composed of neutral gas, cold molecular gas, and hot ionized gas separated into many different components. In IC 10 the ISM is complicated by the high star formation rate, low metallicity, and highly turbulent disk. Previous L-band studies on the irregular dwarf galaxy in recent years have mostly focused on the large-scale HI extensions and their potential origins. With new high-resolution HI 21-cm and L-band 1.0 - 2.0 GHz data from the VLA Local Group L-Band Survey, we focus on the disk of IC 10 and demonstrate two primary analysis techniques that we then use to study a unique, off-disk molecular cloud.

We presented a catalog of continuum point sources detected in our 1.5 GHz central frequency continuum map. This map is the highest spatial resolution data at these frequencies with a spatial resolution of $\sim 1.5''$ and a linear resolution of ~ 6 pc at the distance of IC 10. This allows us to resolve more compact sources than ever before and we find 62 total sources in the central field. We find the spectral indices for each source between the C-band 6.0 GHz image and our 1.5 GHz image and use them and the source positions to classify each source into one of three categories: HII regions, supernova remnants, and background galaxies. Using our L-to-C spectral index values we found 0 HII-regions, 19 SNR, and 43 background galaxies. Performing tests on our spectral index calculations we found that in future imaging the AW-project gridding

algorithm will be necessary to find accurate L-band spectral indices.

In our spectral line analysis, we use a spectral stacking technique to recover low column density dim CO emission under the assumption that the molecular gas has the same velocity as the HI component. In doing so we recovered 23% more emission than previously seen in the integrated intensity moment 0 map alone. We compared the CO stacks with the HI and found the CO line widths had similar values and followed the same trend, decreasing with brightness.

Performing a Gaussian decomposition on the HI emission we found the disk of IC 10 has many regions that can be represented with two HI components. These regions are generally within and around the bright HI, often towards the edge of an HI cloud. We split the HI into the “primary” and “secondary” HI components by brightness. In doing so we found an integrated intensity of $\sim 4.4 \times 10^7$ K km s⁻¹ from the primary component and $\sim 8.9 \times 10^6$ K km/s from the secondary component. We also split the HI emission into that associated with the CO by proximity in the velocity space and found an integrated intensity of 4.4×10^7 K km/s in the component associated with the CO and 4.5×10^7 K km/s from the other component. This indicates that the CO is not necessarily associated with the bright HI component.

Finally, we used the above two techniques to analyze an off-disk molecular cloud, The isolated cloud located in a region with little stellar emission. Through spectral stacking, Gaussian decomposition, and a position velocity diagram we found that this cloud was not unusual in its line widths or central velocities. However, by calculating the dynamical equilibrium pressure both in the disk and in the cloud we found that this region is unique in its high molecular gas fraction and low P_{DE} and is dominated by gas.

5.2 Future Work

Future work on IC 10 L-band data analysis and continuum imaging will be necessary in order to provide more in-depth results and to improve our data analysis methods.

Starting with the L-band continuum, we plan on improving our imaging method by applying the AW-project algorithm in the future once CASA develops its GPU gridding which should improve computation times. Next, we will do more rigorous testing on our source detection to ensure we are finding all of the compact sources in the image. It would also be useful to re-image the C-band data if possible following our L-band methods and applying self-calibration to reduce the artifacts and negative regions in the image. Further, once the sources have been categorized we would like to compare with IC 10 H α emission which traces HII-regions and will help confirm any detections we find.

As part of the Gaussian decomposition, we would like to split the HI into primary and secondary components. Currently, we have split the components by taking the brightest component and the single components as the “primary” and the remaining components as the “secondary”. Next, we would like to look at the rotation curve for IC 10 and split the HI components by proximity to the rotation curve in velocity. We would then like to determine if the CO emission is associated with one component or the other and if so, which component.

In our stacking analysis we would like to take a closer inspection of the dynamical equilibrium pressure, the gas and stellar mass density, the star formation surface density, and the HI and CO line properties across the disk. In doing so we would highlight the different regions within the disk; The HI holes, HI shells, and other molecular clouds further from the center of the disk. Currently, we use the HI moment 1 map to estimate the CO velocity. In the future, it could potentially provide better results to use the Gaussian decomposition values and the HI component that is associated with the molecular gas to estimate the CO velocity and recover more emission.

Finally, with new high-resolution wide-field NIR data tracing stellar populations in IC 10, we could narrow down the potential origins of the large-scale HI extensions visible around the disk of IC 10. Following Ashley et al. (2014) and Gerbrandt et al.

(2015), A new stellar population study of IC 10 in a field of view matching our L-band 21-cm data would enable us to look for stars in the HI extensions which may indicate if IC 10 had an interaction or accretion origin.

Bibliography

- T. Ashley, B. G. Elmegreen, M. Johnson, D. L. Nidever, C. E. Simpson, and N. R. Pokhrel. The H I Chronicles of LITTLE THINGS BCDs II: The Origin of IC 10's H I Structure. *AJ*, 148(6):130, Dec. 2014. doi: 10.1088/0004-6256/148/6/130.
- J. E. Barnes. Evolution of compact groups and the formation of elliptical galaxies. *Nature*, 338(6211):123–126, Mar. 1989. doi: 10.1038/338123a0.
- S. Bhatnagar, U. Rau, and K. Golap. Wide-field wide-band Interferometric Imaging: The WB A-Projection and Hybrid Algorithms. *ApJ*, 770(2):91, June 2013. doi: 10.1088/0004-637X/770/2/91.
- L. Blitz and E. Rosolowsky. The Role of Pressure in GMC Formation II: The H₂-Pressure Relation. *ApJ*, 650(2):933–944, Oct. 2006. doi: 10.1086/505417.
- A. D. Bolatto, J. M. Jackson, C. D. Wilson, and G. Moriarty-Schieven. Submillimeter Observations of IC 10: The Dust Properties and Neutral Carbon Content of a Low-Metallicity Starburst. *ApJ*, 532(2):909–921, Apr. 2000. doi: 10.1086/308590.
- A. D. Bolatto, A. K. Leroy, E. Rosolowsky, F. Walter, and L. Blitz. The Resolved Properties of Extragalactic Giant Molecular Clouds. *ApJ*, 686(2):948–965, Oct. 2008. doi: 10.1086/591513.
- A. D. Bolatto, M. Wolfire, and A. K. Leroy. The CO-to-H₂ Conversion Factor. *ARA&A*, 51(1):207–268, Aug. 2013. doi: 10.1146/annurev-astro-082812-140944.
- A. Brunthaler, M. J. Reid, H. Falcke, C. Henkel, and K. M. Menten. The proper motion of the Local Group galaxy IC 10. *A&A*, 462(1):101–106, Jan. 2007. doi: 10.1051/0004-6361:20066430.
- CASA Team, B. Bean, S. Bhatnagar, S. Castro, J. Donovan Meyer, B. Emonts, E. Garcia, R. Garwood, K. Golap, J. Gonzalez Villalba, P. Harris, Y. Hayashi, J. Hoskins, M. Hsieh, P. Jagannathan, W. Kawasaki, A. Keimpema, M. Kettenis, J. Lopez, J. Marvil, J. Masters, A. McNichols, D. Mehringer, R. Miel, G. Moellenbrock, F. Montesino, T. Nakazato, J. Ott, D. Petry, M. Pokorny, R. Raba, U. Rau, D. Schiebel, N. Schweighart, S. Sekhar, K. Shimada, D. Small, J.-W. Steeb, K. Sugimoto, V. Suoranta, T. Tsutsumi, I. M. van Bemmelen, M. Verkouter, A. Wells, W. Xiong, A. Szomoru, M. Griffith, B. Glendenning, and J. Kern. CASA, the Common Astronomy Software Applications for Radio Astronomy. *PASP*, 134(1041):114501, Nov. 2022. doi: 10.1088/1538-3873/ac9642.
- R. J. Cohen. The unusual kinematics of the galaxy IC 10. *MNRAS*, 187:839–845, June 1979. doi: 10.1093/mnras/187.4.839.

- A. Comrie, K.-S. Wang, S.-C. Hsu, A. Moraghan, P. Harris, Q. Pang, A. Pińska, C.-C. Chiang, R. Simmonds, T.-H. Chang, H. Jan, and M.-Y. Lin. CARTA: Cube Analysis and Rendering Tool for Astronomy. Astrophysics Source Code Library, record ascl:2103.031, Mar. 2021.
- J. J. Condon and S. M. Ransom. *Essential Radio Astronomy*. Princeton University Press, sch - school edition edition, 2016. ISBN 9780691137797. URL <http://www.jstor.org/stable/j.ctv5vdcww>.
- D. Cormier, S. C. Madden, S. Hony, A. Contursi, A. Poglitsch, F. Galliano, E. Sturm, V. Doublier, H. Feuchtgruber, M. Galametz, N. Geis, J. de Jong, K. Okumura, P. Panuzzo, and M. Sauvage. The effects of star formation on the low-metallicity ISM: NGC 4214 mapped with Herschel/PACS spectroscopy. *A&A*, 518:L57, July 2010. doi: 10.1051/0004-6361/201014699.
- T. J. Cornwell, K. Golap, and S. Bhatnagar. The Noncoplanar Baselines Effect in Radio Interferometry: The W-Projection Algorithm. *IEEE Journal of Selected Topics in Signal Processing*, 2(5):647–657, Nov. 2008. doi: 10.1109/JSTSP.2008.2005290.
- G. de Vaucouleurs and H. Ables. Integrated Magnitudes and Color Indices of IC 10. *PASP*, 77(457):272, Aug. 1965. doi: 10.1086/128215.
- B. T. Draine. *Physics of the Interstellar and Intergalactic Medium*. Princeton University Press, 2011. ISBN 9780691122144. URL <http://www.jstor.org/stable/j.ctvcv4h4zr>.
- C. Eibensteiner, J. Sun, F. Bigiel, A. K. Leroy, E. Schinnerer, E. Rosolowsky, S. Kura-pati, D. J. Pisano, W. J. G. de Blok, A. T. Barnes, M. Thorp, D. Colombo, E. W. Koch, I.-D. Chiang, E. C. Ostriker, E. J. Murphy, N. Zabel, S. Laudage, F. M. Maccagni, J. Healy, S. Sekhar, D. Utomo, J. den Brok, Y. Cao, M. Chevance, D. A. Dale, C. M. Faesi, S. C. O. Glover, H. He, S. Jeffreson, M. J. Jiménez-Donaire, R. Klessen, J. Neumann, H.-A. Pan, D. Pathak, M. Querejeta, Y.-H. Teng, A. Usero, and T. G. Williams. PHANGS-MeerKAT and MHON-GOOSE HI observations of nearby spiral galaxies: physical drivers of the molecular gas fraction, R_{mol} . *arXiv e-prints*, art. arXiv:2407.01716, July 2024. doi: 10.48550/arXiv.2407.01716.
- S. A. N. Gerbrandt, A. W. McConnachie, and M. Irwin. The red extended structure of IC 10, the nearest blue compact galaxy. *MNRAS*, 454(1):1000–1011, Nov. 2015. doi: 10.1093/mnras/stv2029.
- V. Heesen, U. Rau, M. P. Rupen, E. Brinks, and D. A. Hunter. Deep Radio Continuum Imaging of the Dwarf Irregular Galaxy IC 10: Tracing Star Formation and Magnetic Fields. *ApJ*, 739(1):L23, Sept. 2011. doi: 10.1088/2041-8205/739/1/L23.
- V. Heesen, E. Brinks, M. G. H. Krause, J. J. Harwood, U. Rau, M. P. Rupen, D. A. Hunter, K. T. Chyży, and G. Kitchener. The non-thermal superbubble in IC 10: the generation of cosmic ray electrons caught in the act. *MNRAS*, 447:L1–L5, Feb. 2015. doi: 10.1093/mnrasl/slu168.
- V. Heesen, D. A. Rafferty, A. Horneffer, R. Beck, A. Basu, J. Westcott, L. Hindson, E. Brinks, K. T. Chyży, A. M. M. Scaife, M. Brüggen, G. Heald, A. Fletcher, C. Horellou, F. S. Tabatabaei, R. Paladino, B. Nikiel-Wroczyński, M. Hoeft, and R. J. Dettmar. Exploring the making of a galactic wind in the starbursting dwarf irregular galaxy IC 10 with LOFAR. *MNRAS*, 476(2):1756–1764, May 2018. doi: 10.1093/mnras/sty325.

- P. Hodge and M. G. Lee. The H II Regions of IC 10. *PASP*, 102:26, Jan. 1990. doi: 10.1086/132603.
- J. A. Högbom. Aperture Synthesis with a Non-Regular Distribution of Interferometer Baselines. *A&AS*, 15:417, June 1974.
- D. J. Hollenbach and A. G. G. M. Tielens. Photodissociation regions in the interstellar medium of galaxies. *Reviews of Modern Physics*, 71(1):173–230, Jan. 1999. doi: 10.1103/RevModPhys.71.173.
- D. A. Hunter, D. Ficut-Vicas, T. Ashley, E. Brinks, P. Cigan, B. G. Elmegreen, V. Heesen, K. A. Herrmann, M. Johnson, S.-H. Oh, M. P. Rupen, A. Schruba, C. E. Simpson, F. Walter, D. J. Westpfahl, L. M. Young, and H.-X. Zhang. Little things. *The Astronomical Journal*, 144(5):134, oct 2012. doi: 10.1088/0004-6256/144/5/134. URL <https://dx.doi.org/10.1088/0004-6256/144/5/134>.
- H. Lee, M. L. McCall, R. L. Kingsburgh, R. Ross, and C. C. Stevenson. Uncovering Additional Clues to Galaxy Evolution. I. Dwarf Irregular Galaxies in the Field. *AJ*, 125(1):146–165, Jan. 2003. doi: 10.1086/345384.
- A. Leroy, A. Bolatto, F. Walter, and L. Blitz. Molecular Gas in the Low-Metallicity, Star-forming Dwarf IC 10. *ApJ*, 643(2):825–843, June 2006. doi: 10.1086/503024.
- A. K. Leroy, F. Walter, E. Brinks, F. Bigiel, W. J. G. de Blok, B. Madore, and M. D. Thornley. The Star Formation Efficiency in Nearby Galaxies: Measuring Where Gas Forms Stars Effectively. *AJ*, 136(6):2782–2845, Dec. 2008. doi: 10.1088/0004-6256/136/6/2782.
- A. K. Leroy, K. M. Sandstrom, D. Lang, A. Lewis, S. Salim, E. A. Behrens, J. Chastenet, I.-D. Chiang, M. J. Gallagher, S. Kessler, and D. Utomo. A $z = 0$ Multiwavelength Galaxy Synthesis. I. A WISE and GALEX Atlas of Local Galaxies. *ApJS*, 244(2):24, Oct. 2019. doi: 10.3847/1538-4365/ab3925.
- A. K. Leroy, A. Hughes, D. Liu, J. Pety, E. Rosolowsky, T. Saito, E. Schinnerer, A. Schruba, A. Usero, C. M. Faesi, C. N. Herrera, M. Chevance, A. P. S. Hygate, A. A. Kepley, E. W. Koch, M. Querejeta, K. Sliwa, D. Will, C. D. Wilson, G. S. Anand, A. Barnes, F. Belfiore, I. Bešlić, F. Bigiel, G. A. Blanc, A. D. Bolatto, M. Boquien, Y. Cao, R. Chandar, J. Chastenet, I.-D. Chiang, E. Congiu, D. A. Dale, S. Deger, J. S. den Brok, C. Eibensteiner, E. Emsellem, A. García-Rodríguez, S. C. O. Glover, K. Grasha, B. Groves, J. D. Henshaw, M. J. Jiménez Donaire, J. Kim, R. S. Klessen, K. Kreckel, J. M. D. Kruijssen, K. L. Larson, J. C. Lee, N. Mayker, R. McElroy, S. E. Meidt, A. Mok, H.-A. Pan, J. Puschnig, A. Razza, P. Sánchez-Blázquez, K. M. Sandstrom, F. Santoro, A. Sardone, F. Scheuermann, J. Sun, D. A. Thilker, J. A. Turner, L. Ubeda, D. Utomo, E. J. Watkins, and T. G. Williams. Phangs–alma data processing and pipeline. *The Astrophysical Journal Supplement Series*, 255(1):19, July 2021. ISSN 1538-4365. doi: 10.3847/1538-4365/abec80. URL <http://dx.doi.org/10.3847/1538-4365/abec80>.
- A. K. Leroy, E. Schinnerer, A. Hughes, E. Rosolowsky, J. Pety, A. Schruba, A. Usero, G. A. Blanc, M. Chevance, E. Emsellem, C. M. Faesi, C. N. Herrera, D. Liu, S. E. Meidt, M. Querejeta, T. Saito, K. M. Sandstrom, J. Sun, T. G. Williams, G. S. Anand, A. T. Barnes, E. A. Behrens, F. Belfiore, S. M. Benincasa, I. Bešlić, F. Bigiel, A. D. Bolatto, J. S. den Brok, Y. Cao, R. Chandar, J. Chastenet, I.-D. Chiang, E. Congiu, D. A. Dale, S. Deger, C. Eibensteiner, O. V. Egorov, A. García-Rodríguez, S. C. O. Glover, K. Grasha, J. D. Henshaw, I. T. Ho, A. A. Kepley, J. Kim, R. S. Klessen, K. Kreckel, E. W. Koch, J. M. D. Kruijssen, K. L. Larson,

- J. C. Lee, L. A. Lopez, J. Machado, N. Mayker, R. McElroy, E. J. Murphy, E. C. Ostriker, H.-A. Pan, I. Pessa, J. Puschig, A. Razza, P. Sánchez-Blázquez, F. Santoro, A. Sardone, F. Scheuermann, K. Sliwa, M. C. Sormani, S. K. Stuber, D. A. Thilker, J. A. Turner, D. Utomo, E. J. Watkins, and B. Whitmore. PHANGS-ALMA: Arcsecond CO(2-1) Imaging of Nearby Star-forming Galaxies. *ApJS*, 257(2):43, Dec. 2021. doi: 10.3847/1538-4365/ac17f3.
- S. Lim and M. G. Lee. The Star Cluster System in the Local Group Starburst Galaxy IC 10. *ApJ*, 804(2):123, May 2015. doi: 10.1088/0004-637X/804/2/123.
- T. A. Lozinskaya and A. V. Moiseev. A synchrotron superbubble in the IC10 galaxy: a hypernova remnant? *MNRAS*, 381(1):L26–L29, Oct. 2007. doi: 10.1111/j.1745-3933.2007.00359.x.
- S. C. Madden. Metallicity Effects on the ISM of Dwarf Galaxies - The Promise of the Herschel Space Observatory. In G. L. Pilbratt, J. Cernicharo, A. M. Heras, T. Prusti, and R. Harris, editors, *The Promise of the Herschel Space Observatory*, volume 460 of *ESA Special Publication*, page 159, July 2001.
- S. C. Madden, A. Poglitsch, N. Geis, G. J. Stacey, and C. H. Townes. [C II] 158 Micron Observations of IC 10: Evidence for Hidden Molecular Hydrogen in Irregular Galaxies. *ApJ*, 483(1):200–209, July 1997. doi: 10.1086/304247.
- S. C. Madden, F. Galliano, A. P. Jones, and M. Sauvage. ISM properties in low-metallicity environments. *A&A*, 446(3):877–896, Feb. 2006. doi: 10.1051/0004-6361:20053890.
- S. C. Madden, D. Cormier, S. Hony, V. Lebouteiller, N. Abel, M. Galametz, I. De Looze, M. Chevance, F. L. Polles, M. Y. Lee, F. Galliano, A. Lambert-Huyghe, D. Hu, and L. Ramambason. Tracing the total molecular gas in galaxies: [CII] and the CO-dark gas. *A&A*, 643:A141, Nov. 2020. doi: 10.1051/0004-6361/202038860.
- L. Magrini and D. R. Gonçalves. IC10: the history of the nearest starburst galaxy through its Planetary Nebula and HII region populations. *MNRAS*, 398(1):280–292, Sept. 2009. doi: 10.1111/j.1365-2966.2009.15124.x.
- A. Marchal, M.-A. Miville-Deschênes, F. Orioux, N. Gac, C. Soussen, M.-J. Lesot, A. R. d’Allonnes, and Q. Salomé. ROHSA: Regularized Optimization for Hyper-Spectral Analysis. Application to phase separation of 21 cm data. *A&A*, 626:A101, June 2019. doi: 10.1051/0004-6361/201935335.
- P. Massey and T. E. Armandroff. The Massive Star Content, Reddening, and Distance of the Nearby Irregular Galaxy IC 10. *AJ*, 109:2470, June 1995. doi: 10.1086/117465.
- N. Mohan and D. Rafferty. PyBDSF: Python Blob Detection and Source Finder. *Astrophysics Source Code Library*, record ascl:1502.007, Feb. 2015.
- B. Namumba, C. Carignan, T. Foster, and N. Deg. H I observations of IC 10 with the DRAO synthesis telescope. *MNRAS*, 490(3):3365–3377, Dec. 2019. doi: 10.1093/mnras/stz2737.
- E. Neistein, F. C. Van Den Bosch, and A. Dekel. Natural downsizing in hierarchical galaxy formation. *Monthly Notices of the Royal Astronomical Society*, 372(2):933–948, 09 2006. ISSN 0035-8711. doi: 10.1111/j.1365-2966.2006.10918.x. URL <https://doi.org/10.1111/j.1365-2966.2006.10918.x>.

- M. Newville, T. Stensitzki, D. B. Allen, and A. Ingargiola. LMFIT: Non-Linear Least-Square Minimization and Curve-Fitting for Python, Oct. 2015. URL <https://doi.org/10.5281/zenodo.11813>.
- D. L. Nidever, T. Ashley, C. T. Slater, J. Ott, M. Johnson, E. F. Bell, S. Stanimirović, M. Putman, S. R. Majewski, C. E. Simpson, E. Jütte, T. A. Oosterloo, and W. Butler Burton. Evidence for an Interaction in the Nearest Starbursting Dwarf Irregular Galaxy IC 10. *ApJ*, 779(2):L15, Dec. 2013. doi: 10.1088/2041-8205/779/2/L15.
- K. Ohta, M. Sasaki, and M. Saito. CO clouds in the dwarf irregular galaxy IC 10. *PASJ*, 40:653–664, Jan. 1988.
- M. S. Roberts. A study of neutral hydrogen in IC 10. *AJ*, 67:431–436, Jan. 1962. doi: 10.1086/108751.
- N. Sanna, G. Bono, P. B. Stetson, A. Pietrinferni, M. Monelli, S. Cassisi, R. Buonanno, E. Sabbi, F. Caputo, M. Castellani, C. E. Corsi, S. Degl’Innocenti, I. Drozdovsky, I. Ferraro, G. Iannicola, M. Nonino, P. G. Prada Moroni, L. Pulone, M. Romaniello, and A. R. Walker. On the Stellar Content of the Starburst Galaxy IC10. *ApJ*, 699(2):L84–L87, July 2009. doi: 10.1088/0004-637X/699/2/L84.
- N. Sanna, G. Bono, P. B. Stetson, I. Ferraro, M. Monelli, M. Nonino, P. G. Prada Moroni, R. Bresolin, R. Buonanno, F. Caputo, M. Cignoni, S. Degl’Innocenti, G. Iannicola, N. Matsunaga, A. Pietrinferni, M. Romaniello, J. Storm, and A. R. Walker. On the Radial Extent of the Dwarf Irregular Galaxy IC10. *ApJ*, 722(2):L244–L249, Oct. 2010. doi: 10.1088/2041-8205/722/2/L244.
- A. Schruba, A. K. Leroy, F. Walter, F. Bigiel, E. Brinks, W. J. G. de Blok, G. Dumas, C. Kramer, E. Rosolowsky, K. Sandstrom, K. Schuster, A. Usero, A. Weiss, and H. Wiesemeyer. A Molecular Star Formation Law in the Atomic-gas-dominated Regime in Nearby Galaxies. *AJ*, 142(2):37, Aug. 2011. doi: 10.1088/0004-6256/142/2/37.
- G. S. Shostak and E. D. Skillman. Neutral hydrogen observations of the irregular galaxy IC 10. *A&A*, 214:33–42, Apr. 1989.
- J. M. Silverman and A. V. Filippenko. On IC 10 X-1, the Most Massive Known Stellar-Mass Black Hole. *ApJ*, 678(1):L17, May 2008. doi: 10.1086/588096.
- L. S. Sparke and J. S. Gallagher, III. *Galaxies in the Universe: An Introduction*. Cambridge University Press, 2 edition, 2007.
- M. Steinmetz and J. F. Navarro. The hierarchical origin of galaxy morphologies. *New A*, 7(4):155–160, June 2002. doi: 10.1016/S1384-1076(02)00102-1.
- J. Sun, A. K. Leroy, E. C. Ostriker, A. Hughes, E. Rosolowsky, A. Schruba, E. Schinnerer, G. A. Blanc, C. Faesi, J. M. D. Kruijssen, S. Meidt, D. Utomo, F. Bigiel, A. D. Bolatto, M. Chevance, I.-D. Chiang, D. Dale, E. Emsellem, S. C. O. Glover, K. Grasha, J. Henshaw, C. N. Herrera, M. J. Jimenez-Donaire, J. C. Lee, J. Pety, M. Querejeta, T. Saito, K. Sandstrom, and A. Usero. Dynamical Equilibrium in the Molecular ISM in 28 Nearby Star-forming Galaxies. *ApJ*, 892(2):148, Apr. 2020. doi: 10.3847/1538-4357/ab781c.
- K. Tehrani, P. A. Crowther, and I. Archer. Revealing the nebular properties and Wolf-Rayet population of IC10 with Gemini/GMOS. *MNRAS*, 472(4):4618–4633, Dec. 2017. doi: 10.1093/mnras/stx2124.

- A. R. Thompson, J. M. Moran, and J. Swenson, George W. *Interferometry and Synthesis in Radio Astronomy, 3rd Edition*. Springer Cham, 2017. doi: 10.1007/978-3-319-44431-4.
- A. Toomre and J. Toomre. Galactic Bridges and Tails. *ApJ*, 178:623–666, Dec. 1972. doi: 10.1086/151823.
- V. Wakelam, E. Bron, S. Cazaux, F. Dulieu, C. Gry, P. Guillard, E. Habart, L. Hornekær, S. Morisset, G. Nyman, V. Pirronello, S. D. Price, V. Valdivia, G. Vidal, and N. Watanabe. H₂ formation on interstellar dust grains: The viewpoints of theory, experiments, models and observations. *Molecular Astrophysics*, 9:1–36, Dec. 2017. doi: 10.1016/j.molap.2017.11.001.
- J. Westcott, E. Brinks, R. J. Beswick, V. Heesen, M. K. Argo, R. D. Baldi, D. M. Fenech, I. M. McHardy, D. J. B. Smith, and D. R. A. Williams. A High-Resolution Radio Continuum Study Of The Dwarf Irregular Galaxy IC 10. *MNRAS*, 467(2): 2113–2126, May 2017. doi: 10.1093/mnras/stx188.
- E. M. Wilcots and B. W. Miller. The Kinematics and Distribution of H I in IC 10. *AJ*, 116(5):2363–2394, Nov. 1998. doi: 10.1086/300595.
- C. D. Wilson. The Metallicity Dependence of the CO-to-H₂ Conversion Factor from Observations of Local Group Galaxies. *ApJ*, 448:L97, Aug. 1995. doi: 10.1086/309615.
- C. D. Wilson and I. N. Reid. Giant Molecular Clouds and the CO-to-H₂ Conversion Factor in IC 10. *ApJ*, 366:L11, Jan. 1991. doi: 10.1086/185898.
- H. Yang and E. D. Skillman. A Nonthermal Superbubble in the Irregular Galaxy IC 10. *AJ*, 106:1448, Oct. 1993. doi: 10.1086/116738.

Appendix A: Appendix

| ID | Offset [arcsec] | RA [°] | DEC [°] | L-band Flux [μ Jy] | C-band Flux [μ Jy] | L-band α | L-to-C α | Class | L-band Class |
|----|-----------------|--------|---------|-------------------------|-------------------------|--------------------|--------------------|-------|--------------|
| 1 | 286.2 | 5.26 | 59.28 | 5104.5 \pm 114.2 | 1335.5 \pm 22.1 | -0.57 \pm -0.001 | -0.91 \pm 0.0002 | SNR | BKG |
| 3 | 265.3 | 5.24 | 59.28 | 1274.8 \pm 83.9 | 458.6 \pm 22.1 | -0.88 \pm -0.004 | -0.96 \pm 0.0008 | BKG | BKG |
| 7 | 220.1 | 5.22 | 59.28 | 102.5 \pm 17.9 | 29.5 \pm 8.1 | -3.18 \pm -0.101 | -1.12 \pm 0.0209 | BKG | BKG |
| 10 | 220.9 | 5.21 | 59.27 | 227.3 \pm 19.5 | 37.7 \pm 8.1 | -1.88 \pm -0.038 | -1.32 \pm 0.0113 | BKG | BKG |
| 12 | 206.2 | 5.21 | 59.31 | 802.7 \pm 20.3 | 168.9 \pm 5.8 | -0.42 \pm -0.01 | -1.12 \pm 0.0024 | SNR | BKG |
| 20 | 262.2 | 5.19 | 59.23 | 187.3 \pm 17.9 | 34.1 \pm 10.5 | -1.38 \pm -0.046 | -1.37 \pm 0.0151 | BKG | BKG |
| 18 | 172.4 | 5.19 | 59.31 | 265.1 \pm 15.5 | 42.9 \pm 5.2 | -1.73 \pm -0.032 | -1.31 \pm 0.0095 | BKG | BKG |
| 23 | 164.6 | 5.18 | 59.27 | 179.1 \pm 21.7 | 20.7 \pm 5.5 | -1.88 \pm -0.054 | -1.57 \pm 0.0226 | BKG | BKG |
| 25 | 138.4 | 5.18 | 59.29 | 70.2 \pm 15.4 | 24.3 \pm 6.7 | -1.43 \pm -0.12 | -0.79 \pm 0.0182 | BKG | SNR |
| 31 | 119.3 | 5.16 | 59.31 | 169.5 \pm 17.6 | 14.5 \pm 4.9 | -1.46 \pm -0.05 | -1.43 \pm 0.0177 | BKG | BKG |
| 32 | 157.5 | 5.16 | 59.32 | 319.3 \pm 21.3 | 33.5 \pm 5.9 | -1.01 \pm -0.03 | -1.5 \pm 0.012 | BKG | BKG |
| 33 | 231 | 5.16 | 59.23 | 298.9 \pm 19 | 39.5 \pm 6.8 | -1.91 \pm -0.03 | -1.44 \pm 0.0106 | BKG | BKG |
| 34 | 178.7 | 5.16 | 59.33 | 213.3 \pm 13.3 | 36 \pm 7.5 | -1.77 \pm -0.04 | -1.28 \pm 0.0114 | BKG | BKG |
| 35 | 283.5 | 5.15 | 59.22 | 310.1 \pm 19.6 | 39.9 \pm 8.1 | -1.81 \pm -0.03 | -1.29 \pm 0.0087 | BKG | BKG |
| 38 | 178.4 | 5.15 | 59.25 | 128.4 \pm 17 | 31.4 \pm 6.7 | -2.16 \pm -0.073 | -1.17 \pm 0.0177 | BKG | BKG |
| 39 | 78.8 | 5.14 | 59.29 | 286.7 \pm 36.2 | 23.6 \pm 6.7 | -1.71 \pm -0.046 | -2.16 \pm 0.0439 | BKG | BKG |
| 47 | 149.3 | 5.14 | 59.33 | 713.5 \pm 15.7 | 158.4 \pm 6.1 | -0.04 \pm -0.012 | -1.08 \pm 0.0026 | HII | BKG |
| 48 | 275 | 5.14 | 59.37 | 538.1 \pm 16.8 | 80.5 \pm 13.1 | -1.66 \pm -0.016 | -1.22 \pm 0.0043 | BKG | BKG |

| ID | Offset [arcsec] | RA [°] | DEC [°] | L-band Flux [μ Jy] | C-band Flux [μ Jy] | L-band α | L-to-C α | Class | L-band Class |
|----|-----------------|--------|---------|-------------------------|-------------------------|--------------------|--------------------|-------|--------------|
| 54 | 66 | 5.13 | 59.3 | 162.6 \pm 24.1 | 37.5 \pm 5.1 | 0.19 \pm 0.055 | -0.99 \pm 0.0111 | HII | BKG |
| 55 | 64.5 | 5.13 | 59.3 | 85.5 \pm 19.2 | 31.7 \pm 6.1 | -1.64 \pm -0.075 | -0.74 \pm 0.0106 | BKG | SNR |
| 59 | 91.5 | 5.12 | 59.31 | 67.7 \pm 13.6 | 16.1 \pm 4.3 | -2.43 \pm -0.126 | -1.33 \pm 0.0368 | BKG | BKG |
| 57 | 36.4 | 5.12 | 59.29 | 213.7 \pm 73.2 | 115.3 \pm 14.5 | -0.42 \pm -0.011 | -1.19 \pm 0.0028 | SNR | BKG |
| 61 | 34.4 | 5.12 | 59.29 | 2616.2 \pm 229.9 | 677.1 \pm 54.2 | -0.25 \pm -0.003 | -0.96 \pm 0.0005 | SNR | BKG |
| 63 | 56.3 | 5.12 | 59.31 | 68.2 \pm 17.7 | 24.9 \pm 6.7 | 0.06 \pm 0.105 | -0.7 \pm 0.0146 | HII | SNR |
| 43 | 43.3 | 5.12 | 59.28 | 180.6 \pm 34 | 66.6 \pm 12 | -0.83 \pm -0.011 | -1.77 \pm 0.0062 | BKG | BKG |
| 60 | 31.7 | 5.11 | 59.29 | 4801.5 \pm 153.1 | 2765.4 \pm 84 | 0.23 \pm 0.001 | -0.64 \pm 0.0002 | HII | SNR |
| 65 | 19 | 5.11 | 59.29 | 7390.2 \pm 100.3 | 5620.1 \pm 45.2 | 0.6 \pm 0.001 | -0.23 \pm 0.0001 | HII | SNR |
| 66 | 75.7 | 5.11 | 59.31 | 2642.7 \pm 18.4 | 175.2 \pm 4.5 | -1.67 \pm -0.003 | -1.93 \pm 0.0022 | BKG | BKG |
| 71 | 252.5 | 5.10 | 59.22 | 94.8 \pm 13.3 | 27.2 \pm 8 | -2.51 \pm -0.092 | -0.91 \pm 0.0152 | BKG | BKG |
| 42 | 35.6 | 5.10 | 59.28 | 812.6 \pm 40.8 | 366.5 \pm 9.4 | -0.53 \pm -0.009 | -0.7 \pm 0.0013 | SNR | SNR |
| 81 | 152.6 | 5.09 | 59.33 | 538.5 \pm 34.7 | 189 \pm 13.8 | -0.66 \pm -0.018 | -0.73 \pm 0.0026 | SNR | SNR |
| 83 | 177.9 | 5.09 | 59.34 | 68.7 \pm 17 | 55.2 \pm 14.8 | -0.5 \pm -0.118 | -0.6 \pm 0.0145 | SNR | SNR |
| 84 | 132.3 | 5.09 | 59.33 | 143.6 \pm 18 | 26.2 \pm 6.8 | -2.15 \pm -0.066 | -1.68 \pm 0.0318 | BKG | BKG |
| 89 | 141.1 | 5.08 | 59.33 | 206.7 \pm 17.2 | 41.7 \pm 7.6 | -0.84 \pm -0.041 | -1.22 \pm 0.0111 | BKG | BKG |
| 90 | 50.8 | 5.08 | 59.3 | 1375.2 \pm 28.9 | 555.6 \pm 6.7 | 0 \pm -0.006 | -0.61 \pm 0.0008 | HII | SNR |
| 94 | 48.8 | 5.08 | 59.29 | 829.4 \pm 41.1 | 473.4 \pm 37.1 | -0.35 \pm -0.007 | -0.78 \pm 0.0011 | SNR | SNR |

| ID | Offset [arcsec] | RA [°] | DEC [°] | L-band Flux [μ Jy] | C-band Flux [μ Jy] | L-band α | L-to-C α | Class | L-band Class |
|-----|-----------------|--------|---------|-------------------------|-------------------------|--------------------|--------------------|-------|--------------|
| 93 | 46.5 | 5.08 | 59.29 | 320 \pm 46 | 208.2 \pm 23.4 | -0.45 \pm -0.012 | -0.96 \pm 0.0023 | SNR | BKG |
| 96 | 161.8 | 5.08 | 59.33 | 109 \pm 20.9 | 51.7 \pm 11.8 | -1.21 \pm -0.099 | -0.64 \pm 0.0124 | BKG | SNR |
| 98 | 137.2 | 5.07 | 59.26 | 382.1 \pm 18.1 | 49.1 \pm 4.4 | -1.35 \pm -0.022 | -1.48 \pm 0.0084 | BKG | BKG |
| 103 | 110.7 | 5.07 | 59.27 | 96.8 \pm 16.9 | 34.6 \pm 4.5 | -1.02 \pm -0.082 | -0.74 \pm 0.0118 | BKG | SNR |
| 105 | 120.8 | 5.07 | 59.32 | 201.3 \pm 18.6 | 36.2 \pm 8.9 | -1.26 \pm -0.044 | -1.29 \pm 0.0129 | BKG | BKG |
| 107 | 110.9 | 5.06 | 59.31 | 6072.1 \pm 58.9 | 1195.9 \pm 24.4 | -0.65 \pm -0.002 | -1.17 \pm 0.0004 | SNR | BKG |
| 109 | 260.3 | 5.06 | 59.36 | 274.2 \pm 18.2 | 59.7 \pm 19.5 | -1.59 \pm -0.04 | -1.12 \pm 0.0092 | BKG | BKG |
| 110 | 104.3 | 5.06 | 59.27 | 1143.6 \pm 48.3 | 188.7 \pm 12.7 | -1.02 \pm -0.01 | -1.28 \pm 0.0031 | BKG | BKG |
| 111 | 182.9 | 5.06 | 59.34 | 1382.4 \pm 105.5 | 221.6 \pm 16.4 | -0.52 \pm -0.01 | -0.68 \pm 0.0013 | SNR | SNR |
| 112 | 98.1 | 5.06 | 59.31 | 170.3 \pm 22.8 | 18.3 \pm 5.8 | -2.69 \pm -0.06 | -2.33 \pm 0.069 | BKG | BKG |
| 115 | 154.7 | 5.05 | 59.26 | 67.5 \pm 17.6 | 15.6 \pm 5 | -1.9 \pm -0.136 | -1.28 \pm 0.0386 | BKG | BKG |
| 119 | 152.5 | 5.04 | 59.32 | 1336.9 \pm 52.1 | 1150.3 \pm 107.6 | -0.4 \pm -0.006 | -0.76 \pm 0.0008 | SNR | SNR |
| 122 | 201.7 | 5.04 | 59.24 | 47.4 \pm 11.9 | 28.9 \pm 8.9 | -1.48 \pm -0.151 | -0.74 \pm 0.0214 | BKG | SNR |
| 129 | 165.4 | 5.03 | 59.26 | 2261.6 \pm 26.2 | 349.1 \pm 6.1 | -0.59 \pm -0.003 | -1.31 \pm 0.001 | SNR | BKG |
| 130 | 191.5 | 5.03 | 59.33 | 463.6 \pm 18.7 | 290.2 \pm 10.7 | 0.01 \pm 0.017 | -0.3 \pm 0.0015 | HII | SNR |
| 131 | 137.9 | 5.03 | 59.31 | 163.3 \pm 17 | 27.2 \pm 8.4 | -1.03 \pm -0.054 | -1.87 \pm 0.0356 | BKG | BKG |
| 133 | 132.4 | 5.03 | 59.29 | 93.3 \pm 20.2 | 53 \pm 5 | -0.22 \pm -0.038 | -0.99 \pm 0.0078 | SNR | BKG |
| 135 | 237.9 | 5.03 | 59.35 | 112.2 \pm 14.7 | 47.4 \pm 14.8 | -1.04 \pm -0.07 | -0.94 \pm 0.013 | BKG | BKG |

| ID | Offset [arcsec] | RA [°] | DEC [°] | L-band Flux [μ Jy] | C-band Flux [μ Jy] | L-band α | L-to-C α | Class | L-band Class |
|-----|-----------------|--------|---------|-------------------------|-------------------------|--------------------|--------------------|-------|--------------|
| 137 | 157.1 | 5.02 | 59.28 | 170.1 \pm 16.3 | 40.7 \pm 8.4 | -1.75 \pm -0.05 | -1.06 \pm 0.0106 | BKG | BKG |
| 138 | 156.3 | 5.02 | 59.28 | 190.2 \pm 16.7 | 29.5 \pm 6.3 | -0.72 \pm -0.043 | -1.36 \pm 0.0144 | SNR | BKG |
| 139 | 159 | 5.02 | 59.28 | 247 \pm 19.5 | 82.7 \pm 6.2 | -0.74 \pm -0.035 | -0.78 \pm 0.0053 | SNR | SNR |
| 141 | 211.5 | 5.01 | 59.33 | 209.4 \pm 17.7 | 33.9 \pm 11 | -1.41 \pm -0.042 | -1.79 \pm 0.0243 | BKG | BKG |
| 144 | 185.1 | 5.00 | 59.28 | 167.6 \pm 19.6 | 61.8 \pm 8.2 | -1.08 \pm -0.05 | -0.76 \pm 0.0074 | BKG | SNR |
| 147 | 205.8 | 5.00 | 59.31 | 226.9 \pm 27.4 | 85.7 \pm 9.7 | -0.86 \pm -0.041 | -0.75 \pm 0.006 | BKG | SNR |
| 148 | 247.7 | 5.00 | 59.25 | 339.9 \pm 21.5 | 65.5 \pm 18.2 | -1.83 \pm -0.025 | -1.26 \pm 0.007 | BKG | BKG |
| 151 | 256.8 | 4.96 | 59.28 | 660.6 \pm 19.6 | 95.5 \pm 16.6 | -1.62 \pm -0.013 | -1.31 \pm 0.0038 | BKG | BKG |

Table A.1: IC 10 full continuum source catalog including all 62 compact continuum sources, L-band and C-band flux densities and both the L-band in-band spectral index as well as the L-band to C-band spectral index. Offset is the source offset from the field center in arcseconds, L-band α is the L-band in-band spectral index value calculated from the CASA .alpha image, L-to-C α is the 2 point spectral index calculated between the L-band 1.5 GHz data and the C-band 6.0 GHz data.